IMPRESSION CREEP AND HIGH CYCLE FATIGUE BEHAVIOUR OF ULTRASONICALLY PROCESSED INSITU Al6061-Al_3Ti/Al_3Zr COMPOSITES

Ph.D. THESIS

by

RAHUL GUPTA

DEPARTMENT OF METALLURGICAL & MATERIALS ENGINEERING
INDIAN INSTITUTE OF TECHNOLOGY ROORKEE
ROORKEE- 247667, INDIA
OCTOBER, 2018

IMPRESSION CREEP AND HIGH CYCLE FATIGUE BEHAVIOUR OF ULTRASONICALLY PROCESSED INSITU Al6061-Al_3Ti/Al_3Zr COMPOSITES

A THESIS

Submitted in partial fulfilment of the requirements for the award of the degree

of

DOCTOR OF PHILOSOPHY

in

METALLURGICAL & MATERIALS ENGINEERING

by

RAHUL GUPTA

DEPARTMENT OF METALLURGICAL & MATERIALS ENGINEERING
INDIAN INSTITUTE OF TECHNOLOGY ROORKEE
ROORKEE- 247667, INDIA
OCTOBER, 2018

INDIAN INSTITUTE OF TECHNOLOGY ROORKEE
ROORKEE

CANDIDATE'S DECLARATION

I hereby certify that the work which is being presented in this thesis entitled **"IMPRESSION CREEP AND HIGH CYCLE FATIGUE BEHAVIOUR OF ULTRASONICALLY PROCESSED INSITU Al6061-Al_3Ti/Al_3Zr COMPOSITES"** in partial fulfilment of the requirements for the award of the Degree of Doctor of Philosophy and submitted in the Department of Metallurgical and Materials Engineering of the Indian Institute of Technology Roorkee, Roorkee is an authentic record of my own work carried out during a period from July, 2013 to October, 2018 under the supervision of Dr. B.S.S. Daniel, Professor, Department of Metallurgical and Materials Engineering, Indian Institute of Technology Roorkee, Roorkee.

The matter presented in this thesis has not been submitted by me for the award of any other degree of this or any other Institution.

(RAHUL GUPTA)

This is to certify that the above statement made by the candidate is correct to the best of my knowledge.

(B.S.S. Daniel)
Supervisor

The Ph.D. Viva-Voce Examination of Mr. Rahul Gupta, Research Scholar, has been held on April 18, 2019.

Chairperson, SRC **Signature of External Examiner**

This is to certify that student has made all the correction in the thesis.

(B.S.S. Daniel)
Supervisor **Head of the Department**

Dated: April 18, 2019

ABSTRACT

Engineering sectors demand materials with stringent combination of properties unattainable by conventional alloys. Particulate reinforced aluminium matrix composites (AMCs) are attractive materials for aerospace, marine and automobile applications. Components such as cylinder blocks, pistons, brake, drums/rotors, cylinder liners, connecting rods, gears etc. are made by AMCs due to their high specific strength and elastic modulus, good high temperature properties and damping capabilities, high wear resistance, good electrical and thermal properties.

In the present work, AMCs are processed by in-situ salt reaction in aluminium melt. It is well known that in-situ process allows finer precipitates and better interfaces to be obtained. By additionally incorporating ultrasonication, better distribution of precipitates is achieved which have a bearing on the mechanical properties of the composite. This improvement is verified by comparing with the mechanical properties of the base aluminium alloy.

To develop AMCs for engine components, creep studies are very important as the components are subjected to high temperature. In recent decades, impression creep method has been used as an alternative of conventional creep test by several researchers to analyze creep property of many materials such as metal matrix composites, superalloys, intermetallics and steel at high as well as low temperature. Unlike conventional creep test, in this test cylindrical indenter with flat end is used to provide constant strain rate under constant stress leading to steady state penetration.

High cycle fatigue resistance is often required for automotive components such as power trains, brake discs or piston, where excellent stiffness or damping properties are required. Therefore, it is of great interest to investigate damage behaviour of AMCs under cyclic loading conditions besides mechanical and physical properties of these materials. AMCs reinforced with particulate are expected to show superior high cycle fatigue property

as compared to the unreinforced matrix alloys. Fatigue life depend on particle size and volume fraction. When the particle size is decreased and the volume fraction is increased, fatigue life is improved due to combination of direct and indirect strengthening. Uniform distribution of the particles in the matrix also increase high cycle fatigue life of the AMCs.

There is very less work reported on the fabrication of in-situ Al_3Ti and Al_3Zr reinforced AMCs by using ultrasonication assisted casting method. Their creep behaviour and fatigue behaviour investigations have not been done so far to the best of our knowledge. It is well established that aluminides can withstand at high temperature and therefore their addition to the base Al alloy can improves its high temperature property. Also, their uniform distribution in the base Al alloy can improve its high cycle fatigue. Ultrasonication has potential to not only disperse reinforced particles uniformly throughout the Al matrix but also eliminate casting defects such as porosity in the AMCs which will lead to superior mechanical properties.

The organization of the thesis is as follows:

Chapter 1 contains a brief introduction to in-situ AMCs, their fabrication techniques, effect of ultrasonication on the microstructure and the mechanical properties of the composite and their creep and high cycle fatigue behaviour.

Chapter 2 gives comprehensive literature review on AMCs and their in-situ fabrication routes, ultrasonic processing, creep behaviour and high cycle fatigue behaviour of AMCs. It also defines the objectives of the present work based on the literature review.

Chapter 3 deals with the details of experimental procedure and equipments used for the characterization of the composites and investigation of their creep and high cycle fatigue behaviour. The procedures of specimen preparation for microstructural evolution (scanning electron microscopy, optical microscopy and transmission electron microscopy), mechanical testing (hardness and tensile test), creep test and high cycle fatigue test are explained.

Chapter 4 deals with processing of Al-Al_3Ti and Al-Al_3Zr composites with different amounts of Al_3Ti and Al_3Zr particles by in-situ reaction of aluminium alloy with potassium hexafluorotitanate (K_2TiF_6) and hexafluorozirconate (K_2ZrF_6), respectively. Ultrasonication of the aluminium melt during salt reaction was carried out to refine the cast microstructure and achieve better dispersion of in-situ formed particles. The in-situ composites were characterized by X-ray diffraction (XRD), scanning electron microscopy (SEM) and transmission electron microscopy (TEM). The particles generated in the melt promoted heterogeneous nucleation, which was responsible for grain refinement of the cast microstructure. The well dispersed in-situ formed particles significantly improved the mechanical properties including ductility, yield strength (YS), ultimate tensile strength (UTS) and hardness. The dominant strengthening mechanism in the composite was the thermal mismatch strengthening followed by Hall-Petch strengthening. It was observed that the mechanical properties of the in-situ Al_3Zr reinforced composite was better than the in-situ Al_3Ti reinforced composite. This was explained as due to the average size of Al_3Zr particles was 1.8 ± 0.8 μm which was around 50% smaller than the in-situ Al_3Ti particles whose average size was 3.4 ± 1.2 μm.

Creep analysis was carried out under stresses between 113 and 170 MPa and temperatures ranging from 543 to 603 K. The results obtained from creep analysis revealed that the composites had higher activation energy and stress exponent compared to the base aluminium alloy. The improved creep behaviour is attributed to the presence of homogeneously distributed particles in the aluminium matrix. The obtained stress exponent and activation energy values suggest that the main creep mechanism in the base Al alloy and the developed composites was lattice diffusion-controlled dislocation climb. However, activation energy values of in-situ Al_3Zr reinforced composite was higher than that of in-situ Al_3Ti reinforced composite which suggested that Al_3Zr reinforced composite was more creep resistant than Al_3Ti reinforced composite.

The high cycle fatigue behaviour of the developed composites was investigated for stress ratio R = 0.1. The results obtained from high cycle fatigue analysis revealed that both the composites had higher fatigue life as compared to the base Al alloy due to uniform dispersion of reinforced particles, refinement of the matrix and clear interface between the particles and the matrix. It was observed from the comparison of high cycle fatigue between the two developed composites that the Al_3Zr reinforced Al composites had higher fatigue life as compared to Al_3Ti reinforced composites under comparable stress amplitude. This improvement was mainly due to presence of fine in-situ Al_3Zr particles.

Chapter 5 summarizes the main conclusions on processing, creep and high cycle fatigue behaviour two intermetallic reinforced aluminium matrix composites, Al-Al_3Ti and Al-Al_3Zr. Additionally, scope for future work is included.

ACKNOWLEDGEMENT

It is my sublime duty to express my deepest sense of gratitude and veneration to my respected supervisor Prof. B.S.S. Daniel, Department of Metallurgical and Materials Engineering, Indian Institute of Technology, Roorkee for his sincere exhortation, indelible inspiration, constant encouragement, meticulous guidance, sustained interest, immense patience and supporting attitude throughout the investigation of the present research problem and preparation of this thesis.

I express my deepest sense of reverence and indebtedness to the esteemed members of my SRC committee Dr. G.P. Chaudhari (SRC Chairman), Associate Professor, Department of Metallurgical and Materials Engineering, Indian Institute of Technology, Roorkee, Dr. S.K. Nath (internal expert), Professor, Department of Metallurgical and Materials Engineering, Indian Institute of Technology, Roorkee, Dr. A.K. Sharma (external expert), Professor, Department of Mechanical and Industrial Engineering, Indian Institute of Technology, Roorkee, and my DRC chairman, Dr. Ujjawal Prakash, Professor, Department of Metallurgical and Materials Engineering, Indian Institute of Technology, Roorkee for their valuable suggestions and eternal encouragement in all my research endeavours.

I am also thankful to the Head Department of Metallurgical and Materials Engineering for providing me with a nice working environment and fellowship. I thank all the faculty members of the Department of Metallurgical and Material Engineering and non – teaching staff, Mr. R.K. Sharma, Mr. Rajendra Sharma, Mr. Naresh Sharma and Mr. Sukhmal Giri for generously providing me the guidance and various research related resources on time.

My friends and colleagues Dr. Devasri Fuloria, Dr. Reenu, Dr. A. Raja, Mr. Rahul Kumar, Dr. Sumit Ghosh, Dr. Raj Kumar, Mr. Guru Prakash, Dr. Vijesh, Dr. Gaurav Gautam and Dr. Nikhil Kumar definitely deserve a special word of thanks for always being there to support and encourage me.

I would like to thank my Seniors Dr. Neeraj Srivastava, Dr. Himanshu Panjiar, Dr. Sandan Sharma, Dr. P. Nageswararao, Dr. Sunkulp Goel and my juniors Ms. Nikki Barla , Mr. Raviraj Verma, Mr. Himanshu Kala, Mr. Nitish Raja and Mr. Nitin for their support and co-operation in lab.

Last but not the least, I am extremely grateful to my mother Mrs. Swadesh Gupta and my father Mr. N.C. Gupta, my sisters Ms. Nalini Gupta, Mrs Bharti Tiwaskar and Ms. Labhni Maheshwari for their unfailing love and support throughout the journey of my research work.

RAHUL GUPTA

TABLE OF CONTENTS

LIST OF FIGURES

LIST OF TABLES

LIST OF ABBREVIATIONS AND SYMBOLS

MMC	Metal Matrix composite
AMCs	Aluminium matrix composites
PRMMC	Particulate reinforced metal matrix composite
PRAMCS	Particulate reinforced aluminium matrix composites
UST	Ultrasonic stirring
SHS	Self-propagating high-temperature synthesis
RSP	Rapid solidification processing
RHP	Reactive hot pressing
RSI	Reactive spontaneous infiltration
RSC	Reactive squeeze casting
XD	Exothermic dispersion
VLS	Vapour-liquid-solid reaction technique
IHT	Isothermal heat treatment
DMR	Direct melt reaction
DIMOX	Directed melt oxidation
DMI	Directed melt infiltration
T	Temperature
T_m	Melting temperature
HCF	High cycle fatigue
LCF	Low cycle fatigue
GPa	Giga Pascal
MPa	Mega Pascal
Pa	Pascal
TEM	Transmission Electron Microscopy
HRTEM	High resolution Transmission Electron Microscopy
SEM	Scanning Electron Microscope
XRF	X-Ray fluorescence
EBSD	Electron Back Scattered Diffraction
EDS/EDAX	Energy dispersive X-ray spectroscopy
XRD	X-Ray Diffraction
BHN	Brinell hardness number
CTE	Coefficient of thermal expansion
Hz	Hertz

k	Kilo
K	Kelvin
˚C	Degree Celsius
cm	Centimeter
m	Meter
mm	Millimeter
μm	Micro meter
nm	Nano meter
ml	Millilitre
UTS	Ultimate tensile strength
YS	Yield strength
Atm	Atmospheric pressure
J	Joules
g	gram
W	Watt
t	Time
s	Second
Kg	Kilogram
N	Newton
SAED	Selected Area Electron Diffraction
F	Force
V	Volume
I	Intensity
$\mathring{A}$	Angstrom
θ	Angle
DNA	Deoxyribonucleic acids
HAZ	Heat affected Zone
A	Area
L	Length
h	Height
FCP	Fatigue crack propagation
FCI	Fatigue crack initiation
FCC	Face centered cubic
V	Volt

e	Electron
d	Inter-planer distance
JCPDS	Joint Committee on Powder Diffraction Standards
ASTM	American Society for Testing and Materials
LVDT	Linear variable displacement transducer
PID	Proportional–integral–derivative
mol	Mole
a.u	Arbitrary unit
GND	Geometrically necessary dislocations
IFFT	Inverse Fast Fourier Transform
PSBs	Persistent slip bands
P(fr)	Probability of particle fracture
$\bar{d}$	Average size of particle
f (σ)	Stress parameter
d_N	Normalization constant
σ_{flow}^{matrix}	Matrix flow stress
σ_{min}^{matrix}	Matrix stress corresponding to the minimum stress require for particle fracture
σ_1	Constant
m	Weibull inhomogeneity factor
Al	Aluminium
Mg	Magnesium
Ti	Titanium
Li	Lithium
Zr	Zirconium

CHAPTER 1
INTRODUCTION

Metal matrix composites (MMCs) is a type of material which derives the best characteristics of combining two or more materials which are chemically and physically distinct from each other. MMCs combine the strength and modulus of reinforcements such as ceramics, oxides, borides etc, and toughness and ductility of metallic matrices such as Al, Mg etc. Thus, MMCs possess superior properties as compared to the unreinforced metals. The reinforcements may be synthesized either ex-situ or in-situ [1–3]. The interface between matrix and reinforcement have a large say in determining the properties of MMCs. For making MMCs, lighter alloys such as Al, Mg and Ti are preferred as matrix materials which provide significant improvement in fuel efficiency for the automobiles and thrust-to-weight ratio for the aerospace applications. The reinforcements are either discontinuous or continuous or a combination of both such as whiskers, chopped fibers, particulates or platelets. The discontinuous reinforced composites are more cost effective as compared to continuous reinforced composites because processing techniques which are used to fabricate unreinforced materials such as liquid metallurgy, powder metallurgy, etc may also use to fabricate discontinuous reinforced composites. They provide more isotropic properties than continuously reinforced composites due to more random orientation of reinforcement and lower aspect ratio. The strength, temperature, density and cost requirements for the intended applications generally govern the choice of matrix materials [4].

Aluminium alloys are mostly used as matrix for MMCs. Al alloys have high corrosion resistance, good damping capability, high thermal conductivity, low density, strength can be provided by precipitation and high electrical conductivity. Aluminium matrix composites (AMCs) are wide studied since the 1970s and are currently utilized in sports equipment, electronic equipment, armours and automobile industries. They provide an outsized form of mechanical properties reckoning on the chemical composition of the Al-matrix. AMCs are

supposed to substitute metal alloys, ferrous alloys, metallic element alloys in many applications. AMCs provide economically viable solutions for wide range of applications due to the size, shape and distribution of reinforcement and near net shape forming [5,6].

To fabricate AMCs, several processing techniques are used such as spray deposition, various casting technologies such as stir casting, compocasting, squeeze casting and rheocasting, powder metallurgy, mechanical alloying and perform infiltration which require the addition of the particulate reinforcement to the matrix materials, which either in molten or powder form.

In all traditional fabrication processing, wetting between reinforcements and molten metal is often poor. Improved wetting leads to better bonding between matrix and reinforcements. By alloying addition such as Mg and Li and through reinforcement coating these problems can be sorted out. During the processing of MMCs, some problems are encountered such as interfacial reaction between the reinforcement and the matrix, the reinforcement distribution and control of volume fraction which degrade properties of MMCs. Ample studies have been done on processing of Al alloys composites by casting routes and its associated techniques [7–10]. The main drawback of this technology is to ensure adequate wetting of reinforced particles by the liquid metal and sustain a homogeneous dispersion of the particles.

Conventional fabrication techniques of MMCs have some inherent problems which are overcome by considering in-situ processing techniques to fabricate MMCs. In in-situ fabrication process, reinforcement phase is formed by chemical reaction with in the metal matrix which is thermodynamically stable and has clean interface which shows strong bond between the phase and the matrix [11]. In-situ composites can contain different types of reinforcement such as organic compounds, metals, ceramics and intermetallics. By controlling microstructure new avenues in structural, magnetic, optical, electrical, thermal and chemical applications can be explored.

Different processes are used to fabricate in-situ composites, some of these are reactive gas infiltration, directed melt oxidation (DIMOX), XD, high temperature self-propagating synthesis (SHS), directed melt infiltration (DMI) [11,12].

However, in-situ processing of AMCs has two main severe issues such as clustering of in-situ formed particles and high porosity. Mechanical stirring is not effective to disperse small particles which are less than a few microns in diameter. Agglomeration of the particles and presence of high porosity severely degrade the mechanical properties of the AMCs, such as tensile strength and fatigue resistance [13][14]. These problems can be overcome by ultrasonication of the molten metal.

Ultrasonic treatment of molten aluminium and its alloys is a well-established technology. It is a promising and effective physical method to refine grain size of matrix, increase homogeneity and reduce segregation. Various mechanisms for grain refinement using ultrasonic vibrations have been proposed. These mechanisms are related to cavitation phenomena induced by high intensity ultrasonic waves. This causes instantaneous temperature and pressure variations in the molten metal. These temperature and pressure variations encourage heterogeneous nucleation and dendrite fragmentation, through acoustic streaming by improving solute diffusion in the molten metal [15]. The main possible effects of ultrasonic vibrations on the characteristics of as cast materials are [16]:

1. High intensity ultrasonic vibration was optimising the microstructure of the composites
2. Large clusters of reinforced particles could be fragmented into the smaller ones effectively in the ultrasonic field.
3. Promotion of columnar to equiaxed transition
4. Alteration in the size and distribution of the reinforced particles
5. Promotion of uniformity in the distribution of the reinforced particles; and

6. Porosity in the composites could be decreased significantly due to the ultrasonic degassing.

Ultrasonic assisted casting process, which involve high intensity ultrasonication, is a novel method to fabricate in-situ AMCs [17–22]. This process is very effective to degas and homogenise the melt [18], de-agglomerate and uniformly disperse the reinforcement particles [19–22].

To develop MMCs for engine components as they have application in automobile industries, their behaviour at high temperature needs to be studied as the components are subjected to high temperature. For example, engine pistons are operated at upto 300 ˚C [23] whereas, thermal stresses acting on the piston is around 100 MPa [24]. Therefore, creep resistance is important for MMCs to be used as engine components. Conventional tensile and compression creep tests are generally used for creep analysis of MMCs [25,26]. Impression creep test is a compressive creep test which has been developed by modifying indentation creep test where flat bottom cylindrical indenter replaces the ball, conical or pyramidal indenter. Under an applied stress, a cylindrical indenter with flat end is indented into the specimen. The depth of indentation of the indenter is recorded and plotted with time to obtain the impression creep curve. In recent decades, many researchers have utilised this elegant test to analysis creep property of many materials such as metal matrix composites, metals, intermetallics and steel at high as well as low temperature [27,28].

For structural applications, fatigue resistance is one of the important design criteria. High cycle fatigue resistance is often required for automotive components such as power trains, brake discs or piston, where excellent stiffness or damping properties are required [29,30]. Therefore, it is of great interest to investigate damage behaviour of MMCs under cyclic loading conditions besides mechanical and physical properties of these materials [30].

For many applications, inadequate fatigue resistance is observed in monolithic Al alloys which can be improved, under certain conditions, by adding high stiffness particulate reinforcement to Al alloys [31,32].

MMCs reinforced with either particulate or whisker show superior high cycle fatigue property as compared to the unreinforced matrix alloys. Fatigue life depend on particle size and volume fraction. When particle size is decreased and volume fraction is increased, fatigue life is increased due to combination of direct and indirect strengthening [33]. Uniform distribution the particles in the matrix also increase high cycle fatigue life of the MMCs [34,35].

Particle reinforced MMCs generally show longer fatigue life than those of unreinforced matrix alloys because cyclic load is mostly carried by high strength and high modulus reinforcement due to which, for a given stress, composite experience a lower strain than the unreinforced matrix alloy [36]. Therefore, it is of great interest to investigate high cycle fatigue (HCF, $\geq 10^5$ cycles) behaviour of particulate reinforced AMCs.

For high temperature applications, Aluminides, as a reinforcement for AMCs, are potential candidate materials. In particular, aluminide intermetallics of transition metals such as Al_3Ti and Al_3Zr are receiving considerable attention because they have low density, high Young's modulus, excellent oxidation and corrosion resistance and high temperature strength. For tetragonal structured Al_3Ti [37], Young's modulus is 217 GPa, density is 3.3 g/cm^3 and melting point is 1350 ˚C [38] whereas for tetragonal structured Al_3Zr [39], Young's modulus is 205 GPa, density is 4.11 g/cm^3 and melting point is 1580 ˚C [40–42]. They have some adverse properties such as brittleness. Therefore, during in-situ casting, reaction should be optimized so that fine and even distribution of these intermetallics could be obtained in the matrix which may improve mechanical properties of the composite. Large size particles of these intermetallics may degrade mechanical properties [43].

In this research, ultrasonic assisted casting method is used to fabricate two different Al matrix composites reinforced with Al_3Ti and Al_3Zr by adding varying amount of K_2TiF_6 and K_2ZrF_6 inorganic salt (5, 10 and 15 wt. %), respectively. At 750 ˚C temperature, these salts are added into the melt to develop composites with different weight percent (2.7, 5.4 and 8.1 wt. %) of Al_3Ti and (3.0, 6.1 and 9.1 wt. %) of Al_3Zr. Microstructural and mechanical properties of these composites are studied. Various strengthening mechanism i.e. coefficient of thermal expansion (CTE) mismatch between the particle and the matrix and Hall-Petch strengthening are analysed. To investigate their high temperature property, impression creep test is carried out under stresses between 113 and 170 MPa and temperatures ranging from 543 to 603 K. High cycle fatigue behaviour of these composites, under constant stress amplitude, are also investigated by maintaining frequency of the test as 50 Hz and stress ratio (R) is 0.1 for all the processed conditions. After fatigue test, fractured surface of the samples is also examined under SEM.

CHAPTER 2
LITERATURE REVIEW

Ultrasonic assisted casting method to fabricate intermetallic (Al_3Ti or Al_3Zr) reinforced Al alloy composite is a recent research area. The brittleness of these intermetallic compounds is compensated by dispersing them in a ductile metal matrix. By using this approach, superior characteristics of intermetallics such as stability at high temperature, high resistance to corrosion, and high hardness can be used without any disadvantages of their intrinsic brittleness. Thus, the beneficial properties of these intermetallics compound can be used in a structural material because the whole material is not brittle due to the ductility of metal matrix [44–46]. In recent works, the detailed study of the processing conditions of Al/Al_3Zr and Al/Al_3Ti has been done to evaluate the mechanical properties and microstructure of these materials [47–49].

2.1 Preparation of AMCs:

AMCs can be produced by two methods namely ex-situ and in-situ processes. In ex-situ process second phase to be reinforced is already available and is added to solid or liquid state matrix. While in in-situ process second phase to be reinforced is generated by chemical reaction between suitable inorganic salts and matrix material [50,51]. AMCs prepared by in-situ process show better properties as compared to materials synthesized by ex-situ process [52].

2.1.1. Ex-situ processes:

2.2.1.1 Liquid ingot casting:

In this process, the second phase reinforcement particles are mixed in the melt by mechanical stirring. Vortex formation helps in uniform distribution of reinforcement articles. Melt is poured into the mould and allowed to solidify. SiC reinforced Al alloy composite has been fabricated by this technique. AA6061 alloy was brought to melt condition in a graphite crucible kept in an electric resistance furnace. The melt was superheated to 750°C

and SiC powder was added while stirring mechanically. After 30 minutes of mixing melt was poured into the preheated mould [50,51,53].

2.2.1.2 Powder metallurgy:

Mechanical mixture of matrix and reinforcement powders are compacted and sintered in this technique. AMC with Al_2O_3 particles (mean particle size 50 nm) reinforced in aluminium (mean particle size 28 μm) have been prepared by this technique. The aluminium and alumina are mixed in the ethanol and dried at 150 °C followed by cold isotropic pressing and sintering in vacuum at 620 ˚C [54].

2.2.2 In-situ processes:

2.2.2.1 Self propagating high-temperature synthesis (SHS):

In this process, reactant powders are preheated in an electric oven followed by ignition. During ignition the powders react exothermically to give final product. By this process AMCs reinforced with fine fibrous titanium carbide (TiC) and multi reinforcements (TiC+TiB_2) have been fabricated [55][56].

2.2.2.2 Rapid solidification processing (RSP):

In RSP process, the molten material is rapidly solidified after reinforcement of particles in the matrix at high temperature. This process is combination of traditional ingot metallurgy with rapid solidification [57]. This process results in refined microstructure with minimum particle segregation, fine particle size and homogeneous distribution of particles. The composites prepared by this method show improvement in the physical and mechanical properties [58]. Al-TiC composites with different compositions and uniform distribution of TiC particles have been produced by this process. These composites exhibit improved mechanical properties [57,59,60].

2.2.2.3 Reactive hot pressing (RHP):

The process was used to prepare TiB_2 reinforced aluminium/aluminium alloy composites. In this process second phase reinforcement particles are generated in the matrix by exothermic reaction of reactant powders. Powders of aluminium, titanium and boron are

blended to prepare the compacts. These compacts are heated at high temperature in vacuum for few minutes. During this period titanium reacts with boron to form TiB_2, then compacts are cooled to a specific temperature and hot-pressed. The in-situ reaction generates submicron size TiB_2 particles in the matrix. Hybrid composites with Al_2O_3 and TiB_2 reinforcement in the aluminium matrix have also been produced by this technique [61–63].

2.2.2.4 Reactive spontaneous infiltration (RSI):

In the RSI process, the molten matrix material is infiltrated through porous preform. The reaction between matrix melt and preform generates second phase ceramic reinforcement particles which are in thermodynamic equilibrium with matrix phase [64]. Micron size Al_2O_3 particles have been generated in the aluminium matrix by infiltrating aluminium melt into preform of SiO_2 or Mg and SiO_2 mixture [65,66].

2.2.2.5 Reactive squeeze casting (RSC):

In this process molten matrix material is poured on preform of the inorganic powder kept in pre-heated die followed by squeezing. The reinforcement particles are generated by the reaction of molten matrix materials with preform inorganic salt powder. This process has also been used to prepare hybrid composites with Al_2O_3 and Al_3Ti reinforcement. The schematic diagram of experimental setup is shown in Figure 2.1 [67,68].

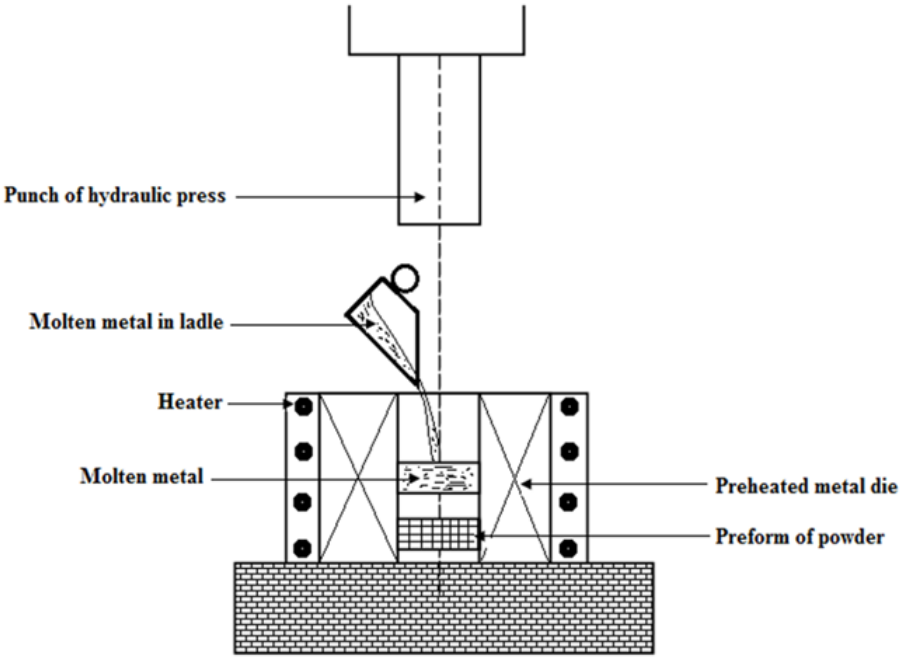

Figure 2. 1 Schematic diagram of experimental set-up for composite fabrication by RSC process [67]

2.2.2.6 Exothermic dispersion (XD):

In this process, the chemical elements (namely, R1 and R2) in required amount are heated at high temperature in the presence of matrix material (M). These chemical elements react exothermically and form submicron size ceramic particles (R1R2) in the matrix. A schematic diagram of the fabrication process of composite materials is shown in Figure 2.2. TiB_2 reinforced AMC have been fabricated by this process. TiB_2 particles are generated by the chemical reaction between Ti and B powders at high temperature in the presence of aluminium powder under argon atmosphere. AMCs with other reinforcements have also been produced by this technique [69–71].

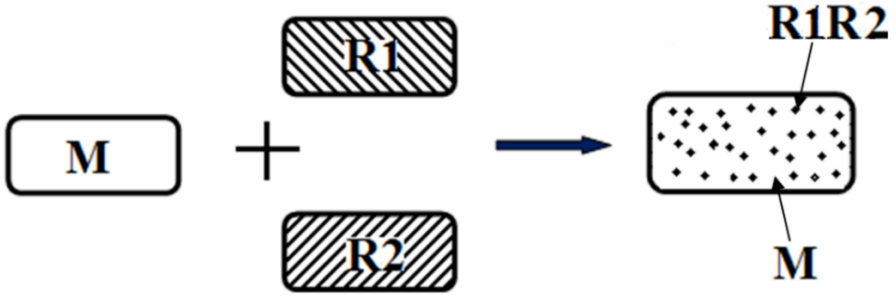

Figure 2. 2 Schematic diagram of the composite fabrication by XD process.

2.2.2.7 Vapour-liquid-solid (VLS) reaction technique:

In this process, the matrix alloy consisting of reinforcement forming element is brought to melt condition and a suitable gas is injected into the melt. This gas reacts with reinforcement forming element and the reinforcement is generated within the matrix alloy [72]. This procedure has been used to prepare TiC particulates reinforced aluminium matrix composites [73][74].

2.2.2.8 Mechanical alloying:

In mechanical alloying technique the composite materials are fabricated by the repeated cold welding, fracturing, and re-welding of reactant powders in a high-energy ball mill [75]. Al-Zr nanocomposites with Al_3Zr reinforcement have been fabricated by this process which exhibit better mechanical properties [76].

2.2.2.9 Isothermal heat treatment (IHT):

In this process, the composite materials are exposed to high temperature which create new second phase particles. These particles act as reinforcement and improved mechanical properties are achieved. Hot rolled rods of Al/TiC have been used to create new reinforcement. These rods were exposed to 600 °C temperature for different time periods. This resulted in the formation of Al_3Ti and Al_4C_3 phases by the chemical reaction between aluminium and TiC, resulting in improved mechanical properties [77].

2.2.2.10 Direct melt reaction (DMR):

In this process, the matrix material is heated above the melting point and inorganic salts (flux) are introduced. These salts are thoroughly mixed in the molten matrix by continuous stirring. These salts react with the molten material to form reinforcement particles and continuous stirring helps in uniform distribution of reinforcement particles. The molten composite is poured into the mould to solidify. A schematic diagram of the apparatus used to fabricate composite material by this technique is shown in Figure 2.3 [78–80].

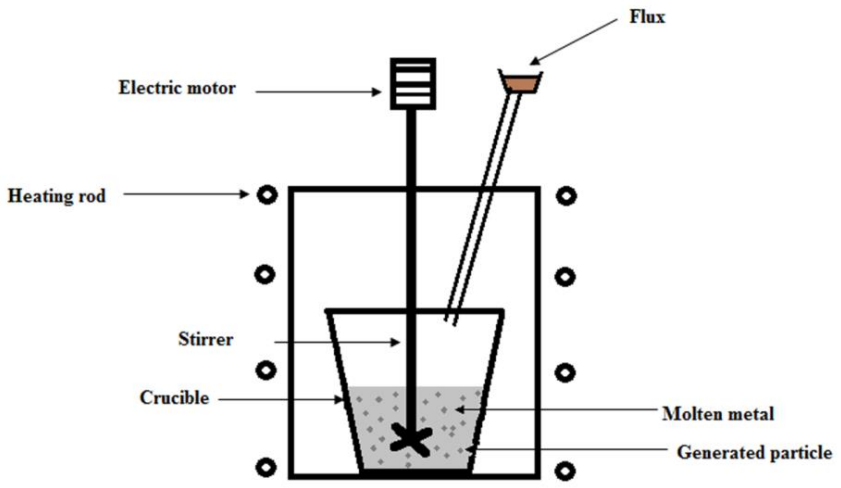

Figure 2.3 Schematic diagram of apparatus used in DMR technique.

2.2.3 Applications of AMCs:

AMCs are being used in different sectors but have gained special attention in components related to automobile, space, aerospace, marine etc. Table 2.1 provides an overview of the property requirements for automotive components. Table 2.2 lists important mechanical properties of AMCs along with manufacturers, and Table 2.3 provides information regarding applications of AMCs in automobile industry with their properties and benefits. Detailed information on AMCs with different reinforcement has been provided [81].

AMCs are also used in several components related to space and aerospace applications. Gr/Al composites are used in high-gain antenna boom for Hubble Space Telescope and B/Al composites in mid-fuselage section of space shuttle orbiter. SiC_p/Al and Telescope and B/Al composites in mid-fuselage section of space shuttle orbiter. SiC_p/Al and SiC_w/Al are used to make bushings, electronic packages, housings, thermal planes and attachment fittings and joints for structural components (truss structures) etc. [82]. Fan exit guide vanes of gas turbine engines, rotating blade sleeves of helicopters, flight control hydraulic manifolds etc are made of AMCs [5]. The spars, tumbuckles, propellers and portholes are also made by AMCs for marine applications [83]

Table 2. 1 Properties requirements for automotive components [81].

System	Component	Justification
Engine	Bearings	Reduced friction, Weight
	Piston Crown	Wear, fatigue, high temperature, creep
	Connecting Rod	Weight, specific stiffness
	Rocker Arm	Wear, stiffness, weight
	Cylinder Block (liner)	Weight, low friction, seizure and wear resistance
	Valve	Wear, fatigue, high temperature, creep
	Piston Ring Groove	Weight reduction, wear resistance
	Wrist Pin	Creep, wear, specific stiffness
Suspension	Struts	Stiffness, damping
Driveline	Wheels	Weight
	Shift Forks	Weight, wear
	Gears	Weight, wear
	Drive Shaft	Fatigue, specific stiffness
Housings	Differential Bearing Pumps	Weight, wear
	Gearbox Bearing	Weight, wear
Brakes	Disk Rotors Calipers	Weight, wear

Table 2. 2 Mechanical properties of AMCs with different matrices and reinforcement [81].

Manufacturer	Matrix	Reinforcement*	Modulus† (GPa)	UTS (MPa)
Martin Marietta and Amax	Al base Al 2219	None TiC, 15 vol.%	74 69-117	221 400
Lanxide	Al base	None SiC, 45-55 vol.% Al_2O_3, 50-70 vol.%	69 152-179 193-262	124-172 400-448 200-276
Dural	Al base Al 2014 Al 6061 Al A356	None Al_2O_3, 10-20 vol.% Al_2O_3, 10-20 vol.% SiC, 10-20 vol.%	72 83-103 83-103 83-97	186-262 414-483 241-345 276-345
Comalco	Al base Al 6061	None Al_2O_3, 20 vol.%	69 85	310 330
Honda	Al base ADC12	None Al_2O_3(f), 10 vol.% Carbon(f), 10 vol.% Carbon(f), 5 vol.%	69 80 70 80	193 250 200 230

Table 2. 3 Automotive demonstrator components of aluminium-matrix composites [81].

Reinforcement	Component	Property	Benefits	Manufacturer
SiC(P)	Piston	Wear resistance, high strength	Reduced weight	Dural, Martin Marietta, Lanxide
Al_2O_3(f)*	Piston Ring Groove	Wear resistance	Higher running temperature	Toyota
Al_2O_3(f)*	Piston Crown (combustion bowl)	Fatigue resistance, creep	Opportunity to use Al, reduced reciprocating mass	T&N, JPL, Mahle and others
SiC(P)	Brake Rotor, Caliper, Liner	Wear resistance	Reduced weight	Dural, Lanxide
Fiberfrax	Piston	Wear resistance, high strength	Reduced weight	Zollner
SiC(P)	Drive Shaft	Specific stiffness	Reduction of parts and weight	GKN, Dural
SiC(w)	Connecting Rod	Specific stiffness and strength; thermal expansion	Reduced reciprocating mass	Nissan
Al_2O_3(f)†	Connecting Rod	Specific stiffness and strength; thermal expansion	Reduced reciprocating mass	DuPont, Chrysler
Al_2O_3 - SiO_2 - C	Cylinder Liner	Wear resistance, expansion	Increased life, reduced size	Honda
Gr(P)	Cylinder Liner, Pistons, Bearings	Gall resistance, reduced wear and friction	Increased power output	Assoc. Eng., CSIR, IISc.‡
TiC(P)	Piston, Connecting Rod	Wear, fatigue	Reduced weight and wear	Martin Marietta
Al_2O_3	Valve Spring, Retainer Cam, Lifter Body	Wear strength	Reduced weight, increased life	Lanxide

* Short fibers.† Long fibers.‡ CSIR; IISc.

2.3 Intermetallic Phases in Aluminium Alloys:

Recently, aluminides, Al_3X (Ti, V, Zr, Nb, Hf, Ta) have gained lot of attention due to their high melting point, low density, good thermal conductivity and good oxidation resistance which make them a potential candidate for high temperature applications. However, at low temperature, their brittleness limits their applications [39,84–87].

According to the Al-Zr and Al-Ti phase diagram as shown in Figure 2.4 and 2.5, respectively, Al_3Zr, and Al_3Ti intermetallics are present in the liquid Al at a temperature of 750 ˚C, respectively. On solidification, both acquire same tetragonal crystal structure, $D0_{23}$ in Al_3Zr and $D0_{22}$ in Al_3Ti, with the space group of I4/mmm [39]. However, as it was discussed earlier that there are some problems associated with Al_3Ti and Al_3Zr which limit

their practical use as structural materials. The poor ductility of aluminides is mainly because of their low crystal symmetry of the tetragonal structure ($D0_{22}$ or $D0_{23}$) [39,84–87] which do not have sufficient number of slip systems to accommodate dislocation motions due to deformation. Tetragonal $D0_{23}$ or $D0_{22}$ structure is closely related to the cubic $L1_2$ structure whose space group is Pm3m and has five independent slip systems [84]. Deformability of the material can be improved by structural isotropy because, for dislocation motions, the variants of active slip systems are increased by isotropy. Thus, it is of great interest to stabilize $L1_2$ structure for practical purposes. According to the recent studies, the presence of third elements such as Cu, Mn, Ag, Cr, Pd, Co, Fe, Zn and Ni stabilize the $L1_2$ structure [86]. The ductility of $L1_2$ cubic structured Al_3Zr and Al_3Ti is improved because $L1_2$ structure has more slip systems. However, neither the influences of atom-species/quantities nor the origin of this effect are fully understood yet. However, high brittleness of the tetragonal structured intermetallics can be beneficial when they are dispersed uniformly in the ductile phase because the presence of hard particles in the soft matrix give strength to the matrix and, consequently, mechanical properties are improved [88][89].

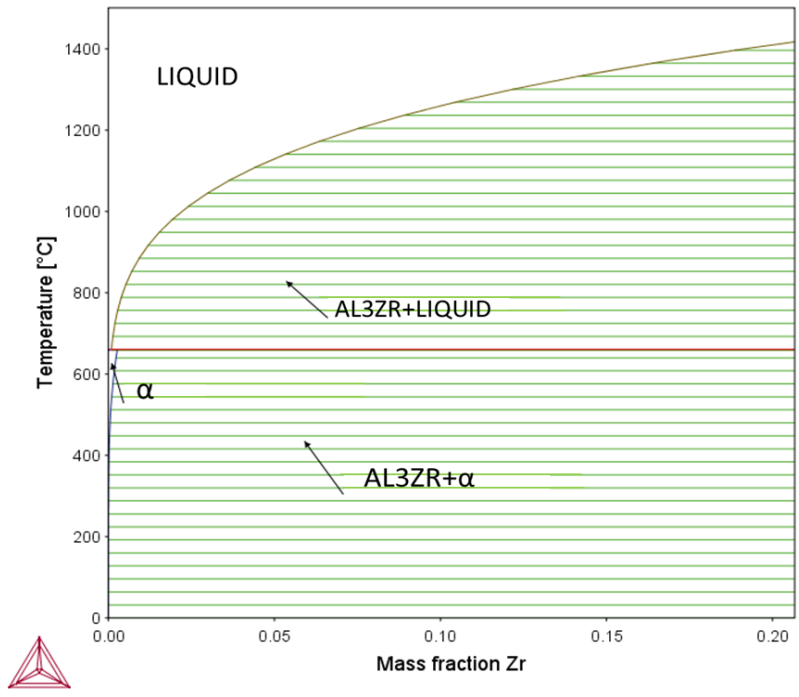

Figure 2. 4 Phase diagram between Al and Zr

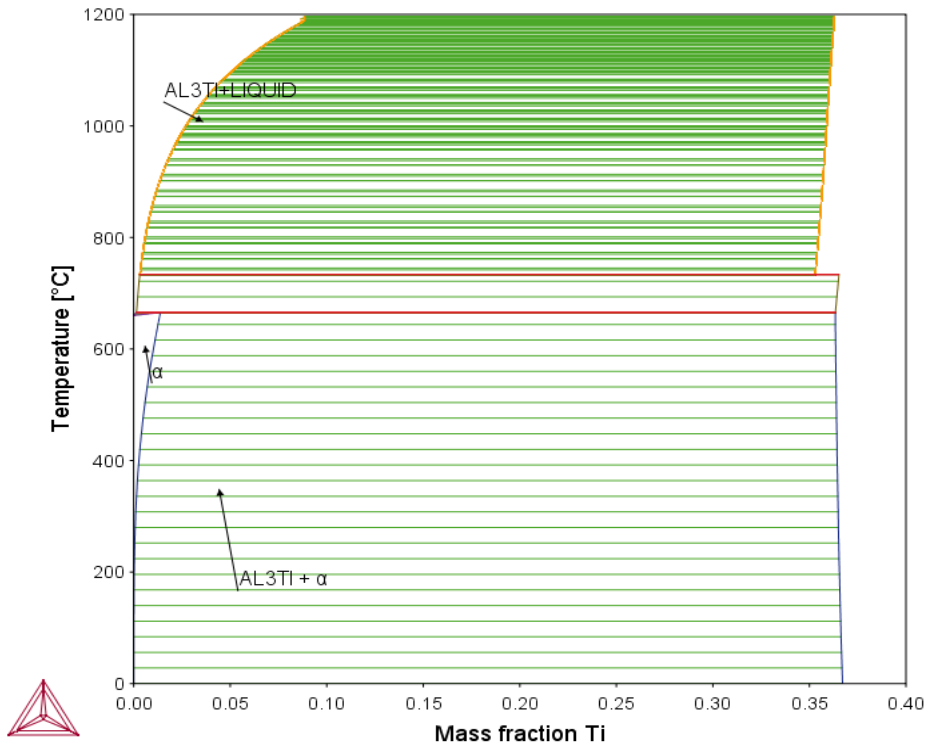

Figure 2. 5 Phase diagram between Al and Ti

2.4 Effects of ultrasonication in molten metals:

When high intensity ultrasound propagates through liquid melts, some phenomena like acoustic streaming and cavitation arise in the molten metal, which causes the change in the morphology of the solidifying phases. Some known metallurgical effects are observed during the treatment of molten metal under the application of power ultrasound. These effects are as follows [90,91]:

i. Solidification under ultrasonic field

   a) Reduction in grain size

   b) Non-dendritic solidification

ii. Refining of melts

   a) Ultrasonic degassing of melts

   b) Fine filtration in the ultrasonic field (USFIRALS process)

iii. Dispersion of other substances into the melts

iv. Acceleration of rate processes

v. Other metallurgical and related effects

When ultrasonic waves are transmitted through a medium, its atomic structure is alternately stretched and compressed [92]. If the negative pressure during the stretching phase or rarefaction phase is strong enough to overcome interatomic binding forces, it can tear apart the medium resulting in tiny cavities (micro bubbles). The cavities so formed can grow under tensile stresses in the succeeding cycles. Eventually they collapse with the release of large magnitude of energy as depicted in Figure 2.6. This phenomenon produces hot spots [93]. These local transient hot spots have very high temperatures (>5000 K) and large pressure (>1000 atm) which could significantly increase the wettability between the particles and the molten metal and break up the clustering of particles [22,94,95]. In addition, the powerful acoustic streaming produced by UST can promote the uniformly dispersion of reinforced particles into the molten metal [96–99].

The important factors controlling the intensity of cavitation are: [100–102]

Ultrasonic frequency: If frequency is low, larger and violently collapsing bubbles are formed which is responsible for de-agglomeration of the particles whereas, smaller cavitation bubbles with shorter life cycle are formed which are useful for chemical reactions and cleaning.

Ultrasonic power: The amount of cavitation per unit of time and volume is determined by the power level. Increase in power increases the number of cavitation events. Nucleation rate of crystallization is increased and crystals are dispersed due to cavitation bubbles which are formed when cavitation occurred in a melt.

Two mechanisms have been proposed for grain refinement of alloys using UST. These mechanisms are dendrite fragmentation and enhanced nucleation due to cavitation [92][103–106].

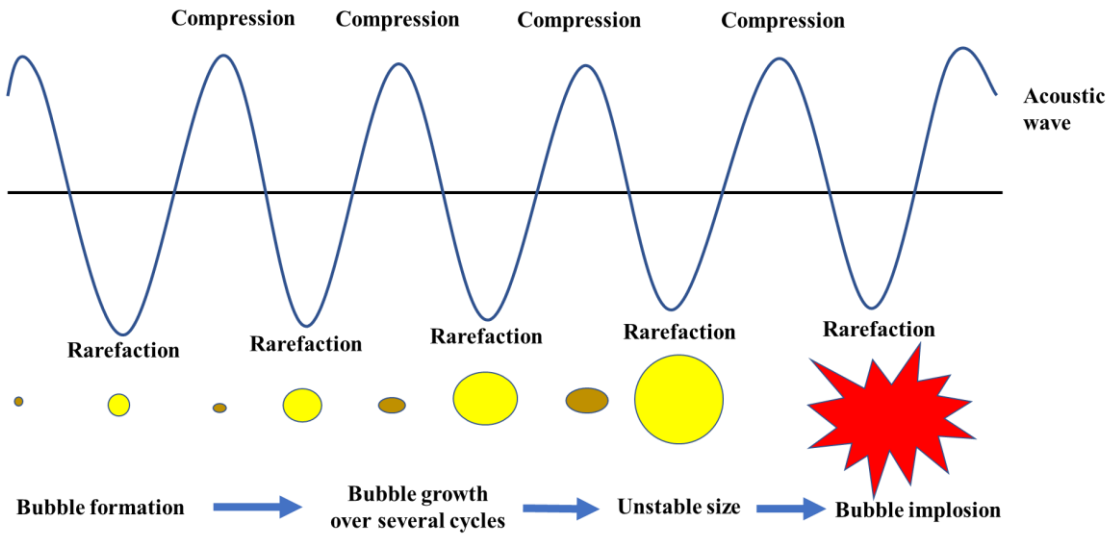

Figure 2. 6 Cavitation phenomena in the melt [118]

2.4.1. Cavitation enhanced nucleation:

Nucleation is affected by UST in several ways. Liquidus temperature of an alloy is influenced by pressure [90]. Some regions in the molten alloy may be superheated while other regions may be undercooled when ultrasonic energy is applied to a melt near its liquidus temperature. When this superheating and undercooling of the melt take place at high frequency, as a result increased number of solid nuclei are formed at each location [107]. Ultrasonic vibration may also affect the grain refiners added to the melt since foreign particles, which act as a nucleation site, are most effective under a certain undercooling. Nucleation may occur when ultrasound vibration is applied in the melt at a temperature higher than the liquidus due to the increase in the pressure [18,108].

Possible mechanisms of crystal nucleation due to cavitation are [109]:

1. From the surface of the expanding cavity, the liquid evaporates to cause cooling of the surface.
2. An increase in the melting point is produced from positive pressure pulse associated with cavity collapse.
3. Cooling is caused by negative pressure associated with cavity collapse.

Interpretation of enhanced nucleation due to cavitation in terms of two different mechanisms are discussed below [107,110]:

2.4.1.1 Pressure pulse melting point (T_m) mechanism:

Cavitation bubbles produced in liquid metal start to collapse, inducing the pressure pulse waves, resulting in an increase of solid-liquid equilibrium temperature. Increase in pressure is responsible for undercooling of the liquid phase due to which melting point is increased according to the Clausius-Clapeyron equation (2.1) [93,111].

$$\frac{dT_m}{dP} = \frac{T_m(V_L - V_S)}{\Delta H} \qquad 2.1$$

where, ΔH is the latent heat of freezing in $J.g^{-1}$, P is atmospheric pressure ~10^5 Pa, T_m is freezing point in K, V_S, and V_L are the specific volumes of solid and liquid phases in $cm^3.g^{-1}$, respectively. Nucleation rate increases due to an increase in T_m, which is equivalent to increasing the undercooling.

2.4.1.2. Cavitation enhanced inclusion wetting:

In this case, the pressure pulse fills the cavities and cracks on the surfaces of the substrates such as the mould, or impurities by molten metal. Therefore, enhanced nucleation results from these defects that can act as effective nucleation sites [90].

2.4.1.3. Cavitation induced endothermic vaporization theory:

This mechanism involves undercooling of the molten metal at the surface of bubble. During cavitation, cavitation bubble size is increased due to expansion of gas inside the bubbles and the temperature of the bubble is decreased, which will cause undercooling at the bubble surface and, as a result, form nuclei on the bubble's surface. When these bubbles collapse, a significant number of nuclei are produced in the melt and this promotes the heterogeneous nucleation in the melt [109].

2.4.2. Cavitation assisted dendrite fragmentation:

During ultrasonic vibration, dendrites are fragmented due to shock and convection waves created in the solidifying melt, which causes melting at a dendrite root, where the

solutes are segregated. Due to increase in local temperature, melting at a dendrite root takes place. Solute concentration is reduced and local temperature is increased when solutes diffuse away from the dendrite roots. Stirring can promote dendrite fragmentation by promoting diffusion of solutes and varying local temperature in the liquid. Furthermore, the local pressure fluctuations given by equations (2.2) and (2.3) lead to fluctuations in the melting temperature which results in the melting of the dendrite roots.

$$p_{max} = p_0 + \sqrt{2\rho cI} \quad 2.2$$

$$p_{min} = p_0 - \sqrt{2\rho cI} \quad 2.3$$

These fluctuations help in the melting of the dendrite roots due to which small grain sized homogeneous microstructure is obtained. However, if the applied ultrasonic field is strong enough to produce cavitation, then a major origin of grain refinement is the fragmentation of crystals to produce new nuclei [92,103–106]. Abramov studied the destruction/fragmentation of growing crystals due to cavitation induced by ultrasound [91]. Equation (2.4) shows the pressure (Pd) required for the fragmentation of crystals [111].

$$P_d = \frac{1}{4}\left(\frac{r}{l}\right)^2 \sigma_{mp} \approx \gamma\sigma_{mp} \quad 2.4$$

Where σ_{mp} is strength of the material near the melting point, and *l* and *r* are the length and radius of the crystal, respectively. Table 2.4 shows that the ultrasonic intensity required for the crystal dispersion scales with the γ parameter. Both the alloy strength and the crystal morphology influence the dispersion of growing crystals. Table 2.4 also reveals how the crystal morphology is related to the size of the mushy zone [91,111].

Table 2. 4 Crystal geometry and ultrasound intensity necessary for crystal dispersion [111]

Crystal growth velocity (μm. s^{-1})	**Crystal length (mm)**	**Crystal radius (mm)**	$\gamma \times 10^{-2}$	**Ultrasound intensity ($W.cm^{-2}$)**
5	0.2	0.05	6.25	30
16	0.4	0.06	2.25	20
25	0.6	0.08	1.78	15
50	1.0	0.12	1.44	10
100	1.6	0.20	1.55	10

It was also reported that UST helps the degassing of the melt and decrease the porosity of the cast-structure [112–117]. Mechanism of ultrasonic degassing is described as follows.

2.4.3. Ultrasonic degassing of melts:

The interaction of high intensity ultrasound with liquid reduces the amount of liquid contained gas, leading to degassing. This effect can be used for degassing metal melts.

Ultrasonic degassing of melts is an environmentally clean and comparatively cheap technique. In this technique, Hydrogen is removed from the molten aluminium with the help of UST. The mechanism of ultrasonic degassing is interdependent on the phenomenon of ultrasonic cavitation in the molten metal. When the ultrasonic horn is applied into the melt, ultrasonic waves produce tensile and compressive stress in the alternate cycle, which forms large number of tiny cavities in the melt at higher ultrasonic vibration. The surface area of pulsating bubbles in rarefaction phase is several times greater than compression phase. At this time, the hydrogen gas diffuses from the surrounding melt in to the bubbles. The amount of hydrogen gas which enters into the bubble in the rarefaction phase is larger than the amount of hydrogen gas leaving the bubble in the compression phase, as shown in Figure

2.7. This is called rectified mass diffusion effect [118,119]. According to this effect, significant amount of hydrogen gas enters into the bubble resulting in increased bubble size. Large bubbles float on the surface of the molten metal due to hydrodynamic buoyancy force and escape from the surface [118].

An experiment was carried out for finding out the rates of removal of hydrogen from Al-Si-Mg alloy by using different processes like, chlorine salts processing, UST, vacuum degassing, combined UST and vacuum degassing and it was observed that combined UST and vacuum degassing gives promising results (as shown in Figure 2.8 and Table 2.5) [109,120].

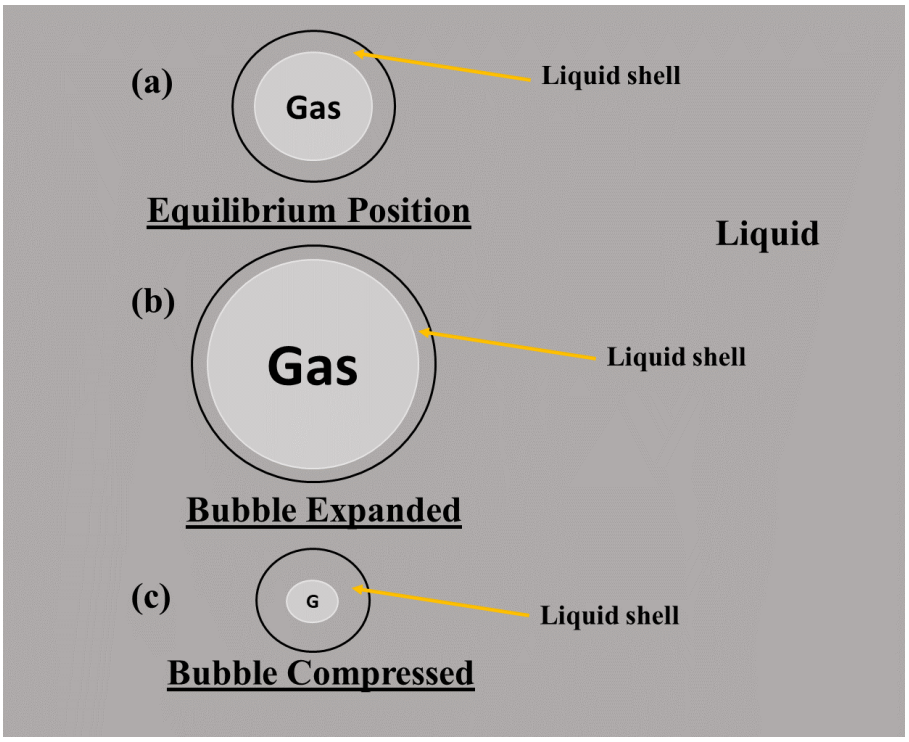

Figure 2. 7 Schematic of rectified diffusion [120]

Table 2. 5 Comparison of efficiencies of degassing techniques used in industry for Al-Si-Mg alloy [109,120]

Degassing techniques	**H_2 (cm^3 per 100 g)**	**Density (10^3 $Kg.m^{-3}$)**	**Porosity number**
Ultrasonic degassing	0.17	2.706	1-2
Vacuum degassing	0.20	2.681	1-2
Argon purging	0.26	2.667	2-3
C_2Cl_6	0.30	2.665	2-3
Universal flux	0.26	2.663	3-4
Initial melt	0.35	2.660	4

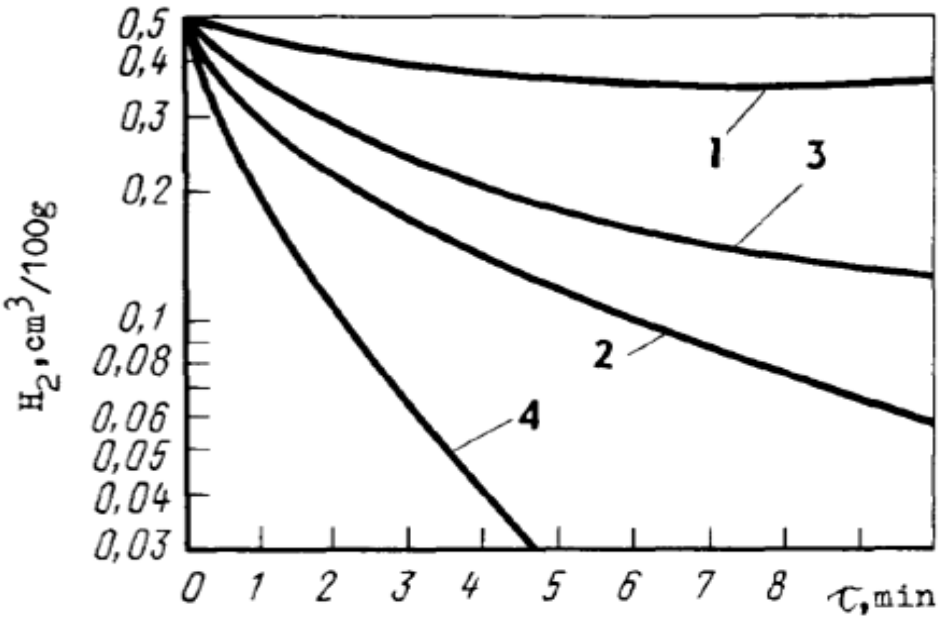

Figure 2. 8 Rates of removal of hydrogen from Al-Si-Mg alloy (1) chlorine salts processing, (2) UST, (3) vacuum degassing, (4) combined UST and vacuum degassing [109,120].

2.4.4 Acoustic Streaming:

Acoustic streaming is a macroscopic movement of fluid induced by acoustic wave [121]. As the acoustic wave travels in the liquid medium, it may be absorbed (attenuation phenomenon). The momentum absorbed from the acoustic field manifests itself as a flow of the liquid in the direction of the sound field, termed as acoustic streaming [122,123]. The schematic diagram of acoustic streaming is shown in Figure 2.9.

When ultrasound propagates through a liquid, absorption of energy from the acoustic beam results in an energy density gradient becoming established in the direction of propagation. A gradient in energy corresponds to a force, and liquid flow can occur due to the energy gradient in the liquid. The relationship can be expressed by the following equation [124]:

$$\vec{\nabla} p = \frac{F}{V} = \frac{2I\alpha}{C} \qquad 2.5$$

Where $\vec{\nabla} p$ is the gradient in pressure, $\frac{F}{V}$ represents the force per unit volume, I is the intensity, α the absorption, and c the speed of sound in the liquid. It is clear that if both intensity and attenuation can vary spatially throughout a sound beam in a liquid, then so will the streaming forces and flows. An increase in either parameter will increase the acoustic streaming.

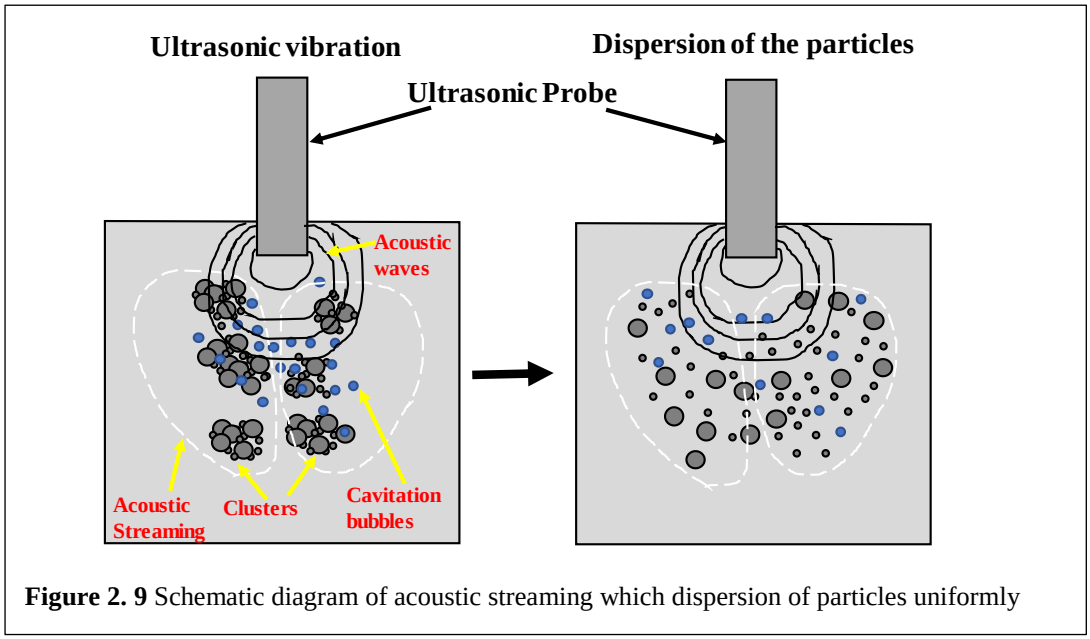

Figure 2. 9 Schematic diagram of acoustic streaming which dispersion of particles uniformly

In addition, there is a second type of acoustic streaming, i.e. acoustic streaming occurring near small obstacles placed within a sound field, or vibrating membrane or bounding walls [125]. It arises from the frictional forces between a boundary and a medium carrying vibrations with a frequency of ω. This time-independent circulation occurs only in

a small region within liquid, leading to form an acoustic microstreaming boundary layer. The thickness of the layer can be estimated by:

$$L = \sqrt{2\eta/\rho\omega} \quad 2.6$$

where η and ρ are the shear viscosity and density of liquid, respectively [123,125]. Due to the restricted scale of the circulation, it is commonly termed as microstreaming.

Acoustic streaming in a liquid can generate the liquid flow, which can accelerate the mass and thermal transfers in the liquid, making the liquid more homogeneous. Furthermore, microstreaming can bring about some important effects resulting from the shear forces generated in the liquid. Thereby, it can be used to disrupt particle clusters in the Al melt for fabricating particulate reinforced Al composites [126–128], disrupt DNA and disaggregate bacteria, etc. [129,130].

2.4.5 Chemical effects of ultrasound:

Many researchers have proposed that the chemical effects of ultrasound do not derive from a direct interaction of the ultrasonic field with chemical species on a molecular level [131–134]. In the research, it is mentioned that the acoustic wavelengths in liquids irradiated with ultrasound are roughly in the range of 0.1-100 mm, which is not on the scale of molecular dimensions. Further, it is also indicated that ultrasound is able to cause high-energy chemistry through the process of acoustic cavitation in a liquid [133].

2.5 Creep behaviour:

2.5.1 Fundamental about creep:

2.5.1.1 The creep curve:

When high temperature and stress are applied on a material, creep occurs and material is permanently deformed. Creep is of engineering significance at a $T > 0.5\ T_m$ [135], where T_m is absolute melting temperature in the Kelvin scale. Temperature and stress govern the creep rate because when temperature and stress are increased, creep rate is also increased as shown in Figure 2.10 (a) and (b), respectively.

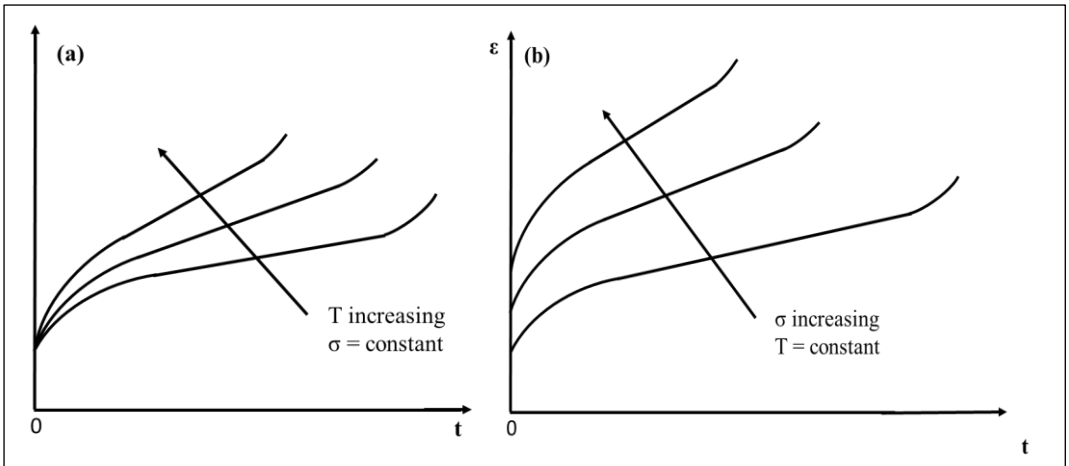

Figure 2. 10 Effects of (a) temperature and (b) stress on a typical creep curve [144]

A typical creep curve, as shown in Figure 2.11, is obtained from a uniaxial creep test which shows creep strain as a function of time. It is observed from the figure that the creep response of the material can be characterised by three different regions. i.e. primary, secondary and tertiary creep regions, and the instantaneous deformation which is either elastic or elastic-plastic.

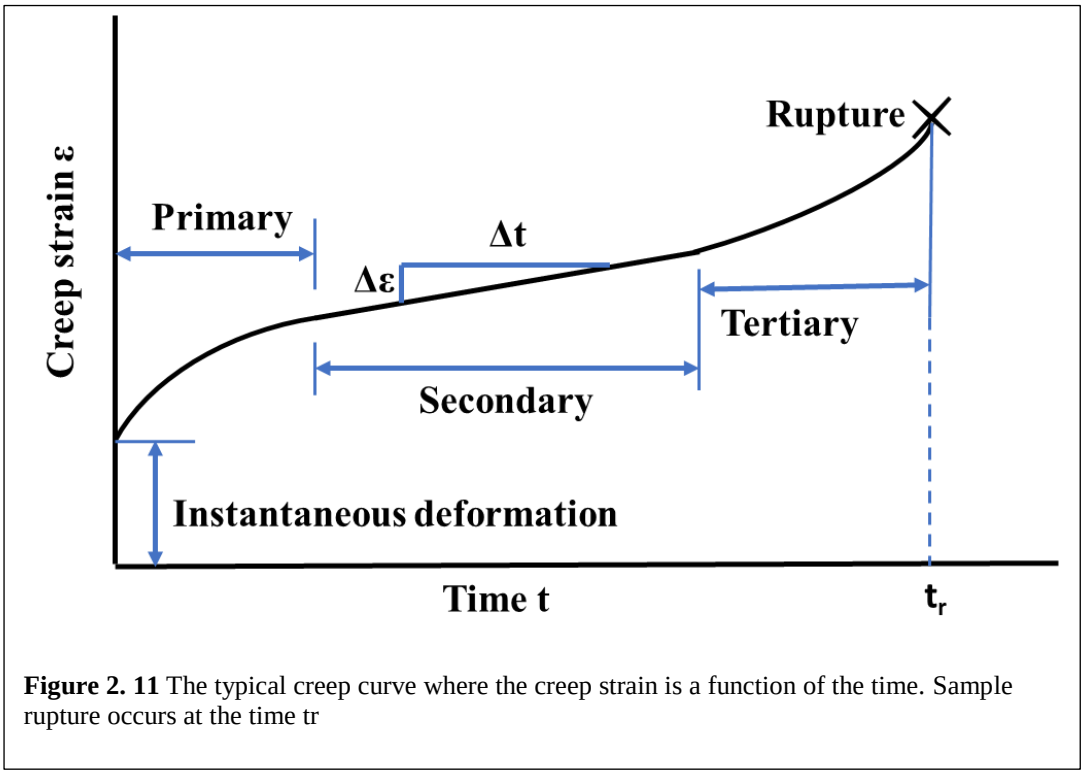

Figure 2. 11 The typical creep curve where the creep strain is a function of the time. Sample rupture occurs at the time tr

In primary creep which is also known as transient creep, it is observed that creep rate is decreased steadily. During limited plastic deformation, dislocations are generated in the

material and their density is increased over time which results in dislocation hardening of the material and hence creep rate is decreased [136].

In secondary creep which is also known as minimum creep or steady state creep, it is observed that creep rate is constant. In this region of creep, dislocations start annihilating by cancelling out each other. Due to annihilation effect, material become soft which not only lowers the dislocation density but also lower the internal energy of the material. Creep rate is constant because new dislocations are formed and old dislocations are annihilated which keeps the dislocation density constant and a dynamic mechanical equilibrium is maintained in the material. When temperature is increased, thermal fluctuation occurs in the material due to which creep deformation takes place. This is the difference between high temperature and sustained low temperature deformation [136].

In tertiary creep, creep rate is further increased due to rupture of material. This increase in creep rate can be attributed to the presence of voids in the grain boundaries which weaken the material and increased annihilations of old dislocations over formations of new ones. The final rupture of the material takes place due to the formation, growth and accumulation of the voids which form crack in the grain boundaries and, consequently weaken the microstructure. Ageing process of the material which makes the microstructure weak and reduction in cross section area due to necking lead to the final rupture of the material [136].

The engineering components should be designed in such a way that they should spend most of their lives in the primary and secondary stages and do not enter into the tertiary stage of creep. The life of the component is determined by the secondary creep rate and therefore, it is considered as a design criterion for the components which are subjected to creep [137,138].

2.5.2 Temperature dependent creep deformation mechanisms:

For temperature above 0.3 T_m, for metals, the deformation of the material is enhanced because the energy associated with atomic vibration increases [139,140]. This can cause time dependent deformation, i.e. creep to occur. Various mechanisms govern creep deformation at different temperatures domains. At a temperature below 0.35 T_m, when stress is applied to the material, dislocation slip processes take place which is rate controlling. In this mechanism, dislocations, which are generated due to plastic deformation, are resisted by some obstacles such as solute precipitates or other dislocations [140]. At temperatures in the range between 0.35 T_m and 0.4 T_m, the energy level of screw dislocations is increased which allow them to move away from the obstacles as a consequence of the cross-slip mechanism. When temperature is increased up to 0.6 T_m, diffusion is active in metallic crystals. Under an applied stress field, when dislocation motion is encountered by an obstacle, e.g. a solute precipitate, the atoms of the dislocation in the proximity of the obstacle diffuse away from it. In this condition, dislocation can climb over the obstacle, by the process called creep recovery [140–143]. At temperatures above 0.8 T_m, creep occurs by diffusion within crystals nevertheless this temperature range falls outside normal structural engineering applications [140].

Diffusion and dislocation climb generate time-dependent unrecoverable deformation, i.e. creep deformation, which represents one of the main effects of temperature increase on the mechanical behaviour of materials [139–141,144].

2.5.3 Impression creep test:

The need for creep testing has become important over the last few decades to understand high temperature failure of materials [145,146]. These needs have been driven by the aerospace and power generation industries. Another aspect is the need for carrying out creep testing where only small amounts of material are available for assessment [145,147–149]. This includes non-destructive evaluation of in-service components,

especially when the removal of material could significantly impair the structural integrity of the component [150], the characterization of the HAZ of welds [151], the development of new alloys [149] and, in the nuclear industry, problems related to the handling of active materials [146]. In these situations, it may not be possible to use conventional full-size specimens. Therefore, innovative techniques have been developed [139,145–148,152] which requires very small volume of material for creep testing analysis and impression creep is one of those innovative testing techniques. An illustration of the impression creep test can be seen in Figure 2.12.

Use of the impression creep test method was first reported in 1977, by Chu and Li [27], for testing of a molecular crystal which exhibited creep behaviour at room temperature, and, then, it was used for testing of several materials, such as the HAZ of P91 welds [148], 316 stainless steel, 0.5Cr-Mo-V steel [147], magnesium alloys [153] or solid fuel for the nuclear industry [154]. Impression creep testing was also used under stepped load or stepped temperature conditions, in order to investigate the creep response of the material, at different stresses or temperatures, using a single specimen in each case [155].

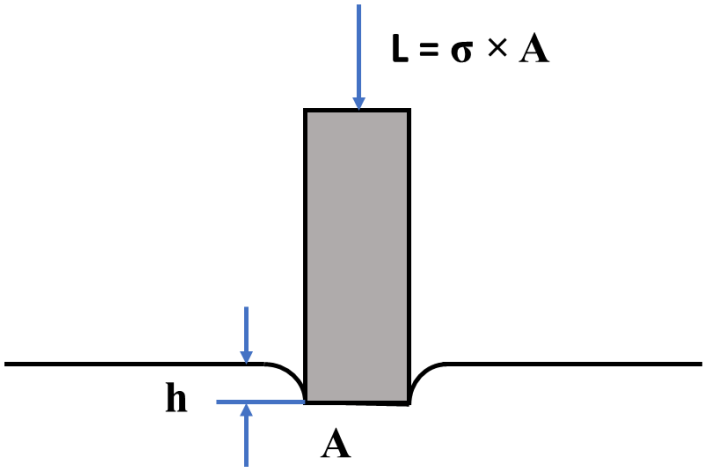

Figure 2. 12 Schematic diagram of impression creep test which shows that load "L" is applied on the punch whose area is "A" which creates an impression of depth "h" in the material.

The impression creep deformation curve is related to the primary and secondary creep properties of the tested material in the vicinity of the contact region between the

specimen and the indenter. Due to the compressive stress field which is produced in the specimen during the test, the material does not exhibit creep damage, and therefore, tertiary creep behaviour cannot be investigated by using this technique [153,155]. However, Rashno et al. [153] reported that magnesium alloy MRI153 exhibited an increase of the displacement rate curve when impression creep tested at 217 ^{o}C and they related this behaviour to carbide coarsening or precipitate dissolution.

It is generally considered that the contact is between the indenter and the specimen must be relatively large compared to metallurgical features, in order to obtain bulk creep properties of the material investigated and to avoid size effects which can affect the experimental results when less than 6-10 grains are covered by the effective section of the specimen, i.e. the contact area with the indenter [147,156].

2.5.3.1 Comparison with conventional creep test:

Impression creep tests have been compared with conventional creep tests since the origin of impression creep testing. From the comparison, it was found that the results showed agreement in both the activation energy and stress exponent [27,157]. Subsequently, many comparisons have been reported in the literature [158]. The effect of cavity depth, slip and stick on the impression velocity by using finite elemental method have been studied [159]. Conclusions drawn from this work are (1) the power law exponent assumed in the calculation is the same as the stress exponent between punching stress and impression velocity. (2) After a transient stage, the velocity of the punch is constant which decrease with the cavity depth and increase with the power exponent. (3) Under the punch, slip or stick conditions between the material and the punch govern the maximum stress which is proportional to the applied load. (4) The steady state impression velocity is the smallest for all stick conditions and is the largest for all slip conditions for the same applied load.

Comparison between impression creep and conventional creep of single crystal of lead has been reported in literature by Chiang and Li [160]. They observed that both the stress and temperature dependences are comparable to those of constant stress tensile creep.

As suggested by Chu and Li [27], Sastry [28] compared tensile and impression creep of Mg by dividing punching stress by 3 to compare with the tensile stress and by dividing the impression velocity by the diameter of the punch to compare with the tensile strain rate. Both the tests were performed at 478 K. The same comparison was made for Cd at 373, 403 and 433 K. The stress exponent was 5.2 to 5.7 for Cd in the temperature range of 348 to 433 K for tensile creep whereas, for impression creep, it was 5.7 in the temperature range of 368 to 453 K. For Zn, the stress exponent was 4.0 to 4.5 for tensile creep whereas, for impression creep, it was 4.5 to 4.6 at 373 K. The stress exponent calculated by using impression creep for a near eutectic Sn-Pb alloy and for superplastic Zn-22 wt. % Al alloy agreed with those from conventional creep tests reported in the literature.

More recently, impression creep of Ni based single crystal superalloys was compared with uniaxial tensile creep by computer simulation [161]. The stress exponents obtained for uniaxial tensile creep were 5.13, 5.10 and 5.12 whereas, for impression creep, stress exponents were 4.96, 5.13 and 5.10. Finite element method was used to calculate these results. Uniaxial creep and impression creep are two different tests. Therefore, only the activation energy and the stress exponent can be compared.

2.5.3.2 Impression velocity under diffusion creep:

Diffusional creep of a semi-infinite medium under cylindrical punch was analysed by Chu and Li [27]. They found that the impression velocity is inversely proportional to the punch radius and proportional to the lattice diffusivity and punching stress at low punching stresses. However, it is inversely proportional to the square of the punch radius for interfacial diffusion between the material and the punch. Impression velocity is proportional to the punch radius and dependent on the punching stress for dislocation creep.

The impression velocity of a thin film was analysed by lattice diffusion using a straight punch by Yang and Li [162]. They found that the impression creep velocity is inversely proportional to the square of the punch width and is directly proportional to the film thickness. However, the impression velocity, without the substrate, is independent of the punch width and inversely proportional to the film thickness. They also analysed impression creep of a thin film by lattice diffusion using a cylindrical punch [163]. They found that the impression velocity is proportional to the punching stress at low punching stresses whereas the impression velocity, for the same punch radius and the same punching stress, increases without the substrate and decreases for a rigid substrate.

2.5.3.3. Impression velocity under dislocation creep:

The impression velocity was analysed by Chu and Li [27] using finite element method in which the strain rate obeys a power law of the von-Mises stress. They found that the impression velocity obeys the same power law with the punching stress and is proportional to the punch radius. For comparison with uniaxial creep test, the effective gauge length is 0.84 of the punch diameter and the effective stress is 0.3 of the punching stress.

Finite element method was also used by Hyde et al. [164] to simulate the impression creep. They found that the equivalent uniaxial strain rate was the impression velocity divided by 0.755 of the punch diameter and the equivalent uniaxial stress was 0.296 times the punching stress which agree with the findings of Chu and Li [27]. Later, these findings were also confirmed by Hyde et al. [165] conducting impression creep experiments on 316 stainless steel at 600 ˚C.

2.5.3.4 Limitations of impression creep test:

A limitation of this technique is represented by the range of materials that can be tested, because, in order to avoid excessive deformations of the indenter, its creep resistance needs to be two to three orders of magnitude higher than that of the specimen. Therefore, steels for high temperature applications can be tested [147], while materials with higher

creep strengths, such as nickel-based superalloys, cannot be tested [145]. Also, the displacement of the indenter during the test is of the order of ~0.1 mm, hence accurate measurement systems need to be used because experimental noise, for example due to temperature fluctuations during the test, is likely to affect the test results [145,155].

2.6 Fatigue behaviour:

Typically, material for structural applications are designed in such a way so that maximum stresses do not exceed the tensile yield strength of the material during their lifetime so that only elastic strains are developed. However, local stresses are also generated due to microstructural discontinuities such as pores and inclusions in the structure including design flaws and surface imperfections. Thus, total stresses acting on the material are more than the yield stress of the material which results in formation and propagation of cracks after some repeated loading leading to final rupture. This progressive failure is referred to as fatigue.

In the early 1800's, engineers observed fatigue as a problem of crack developed in railroad sections and some bridges where stresses were well under the yield strength. Thus, engineers concluded that the materials were "tired" and used the word "fatigue" [166]. Today, failures to fatigue account for ninety percent of the total failures reported in the published literature. This is one of the most common type of failure experienced while in service as reported by Dieter and Reed-Hill [135,167].

There are three events in the fatigue failure which are nucleation of a crack, propagation of the crack and the final failure, as shown in Figure 2.13. Fatigue crack growth, which is perpendicular to the applied tensile load, occurs cycle by cycle. It is governed by crack tip stress intensity [168]. Fatigue crack propagation (FCP) can be separated into three stages: Crack growth in stage I occurred by crack propagation due to shear decohesion of a single slip system and is limited to within a single grain. Transition of the crack growth from stage I to stage II takes place at higher stress intensities due to which two slip systems are

activated and multiple grains are present within the crack tip plastic zone. In this stage, crack growth is normal to the loading direction and fatigue striations are formed on the fracture surface. In stage III, material has completely failed due to overload fracture. Fracture toughness or ultimate tensile strength of the material limit the overload fracture. It occurs when the cross-sectional area is decreased to a point where it cannot hold the maximum applied stress during the applied tensile load cycle any longer.

When the yield strength of the material is lower than the maximum cyclic stresses, rapid crack initiation takes place due to gross plasticity within the material and the crack propagation rate governs the number of cycles to failure [169]. This is termed as low cycle fatigue, whereas high cycle fatigue is somewhat different. In high cycle fatigue, yield strength of the material is higher than the maximum applied stress. During high cycle fatigue, fatigue crack initiation (FCI) takes place due to inhomogeneous localised plasticity which may occurs at defect sites such as grain boundaries, secondary phases, surface asperities or inclusions [169]. Slip face less resistance in surface grains or around surface features than in the interior. Therefore, surface of a component or specimen are responsible for initiation of the fatigue crack, but fatigue crack is nucleated internally when, due to internal defects, there are sufficiently high local stress concentrations. Fatigue crack can also initiate in polycrystalline, and high purity single phase, single crystal with very smooth surfaces. Therefore, stress concentrations at persistent slip bands on the surface of the material are the main cause for fatigue crack nucleation [168].

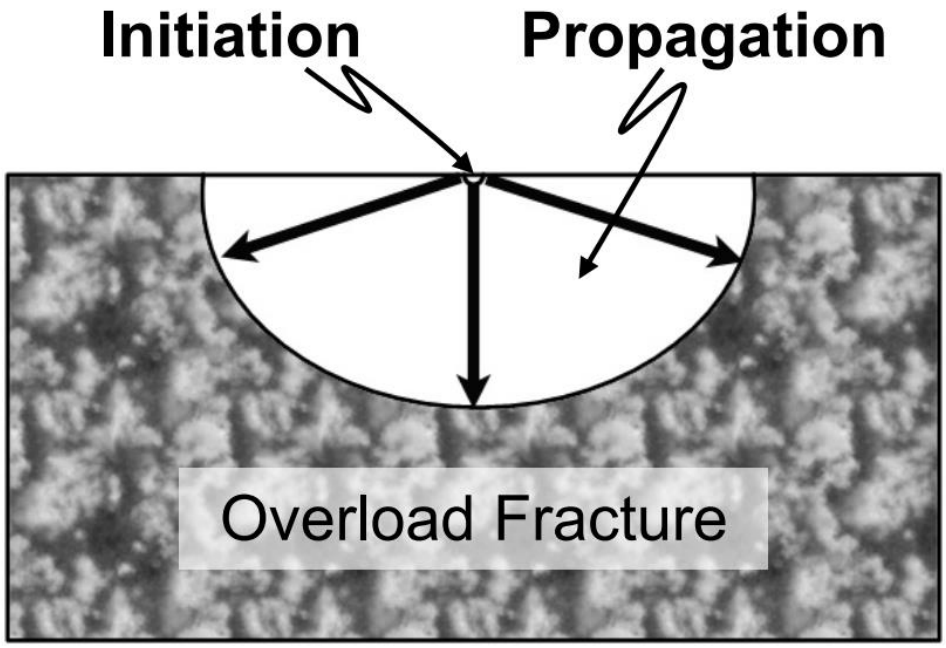

Figure 2. 13 Schematic illustration of stages in fatigue failure

Kim and Laird [170,171] also examined stage I crack to investigate the fatigue crack nucleation process. In stage I cracking, crack due to plastic blunting process is advanced from grain boundary surface to the internal boundary as it is extended up to 180 μm into the specimen surface. Transition from stage I to stage II occurred when multiple slip systems are activated due to sufficiently high stress intensity or when the crack reached triple point junctions. Impurity segregation along grain boundaries are not considered by Kim and Laird to describe the grain boundary crack initiation process but during high cycle fatigue, weakening of grain boundaries will likely affect the rate of fatigue crack nucleation and propagation. Components, which are designed against fatigue failure, are tested in a laboratory environment where service stresses are simulated because stress cycles applied on the material in a laboratory is different from an in-service stress cycles as shown in Figure 2.14. During fatigue, either strain or load control cyclic loading is applied to the test specimen. In high cycle fatigue, load control testing is utilised because strain is limited to elastic values due to low stress levels whereas, in low cycle fatigue, tests are performed under strain control because stress state of the material is changed by microplasticity [169].

During fatigue testing, cyclic loading is simulated by using wave functions which is square, trapezoidal, sinusoidal or triangular. To describe constant amplitude stress-controlled waveform fatigue testing, terminologies are used which are shown schematically in Figure 2.14 and also shown below as Equations (2.7) through (2.12) [135]

N_f = number of cycles to failure

σ_{max} = maximum stress applied during cyclic loading 2.7

σ_{min} = minimum stress applied during cyclic loading 2.8

σ_a = stress amplitude for the fatigue test

$$= \frac{\Delta\sigma}{2} = \frac{\sigma_{max} - \sigma_{min}}{2} \quad 2.9$$

σ_{mean} = average stress applied during cyclic loading

$$= \frac{\sigma_{max} + \sigma_{min}}{2} \quad 2.10$$

$\Delta\sigma$ = stress range

$$= \sigma_{max} - \sigma_{min} \quad 2.11$$

$R = \frac{\sigma_{min}}{\sigma_{max}}$ = fatigue stress ratio 2.12

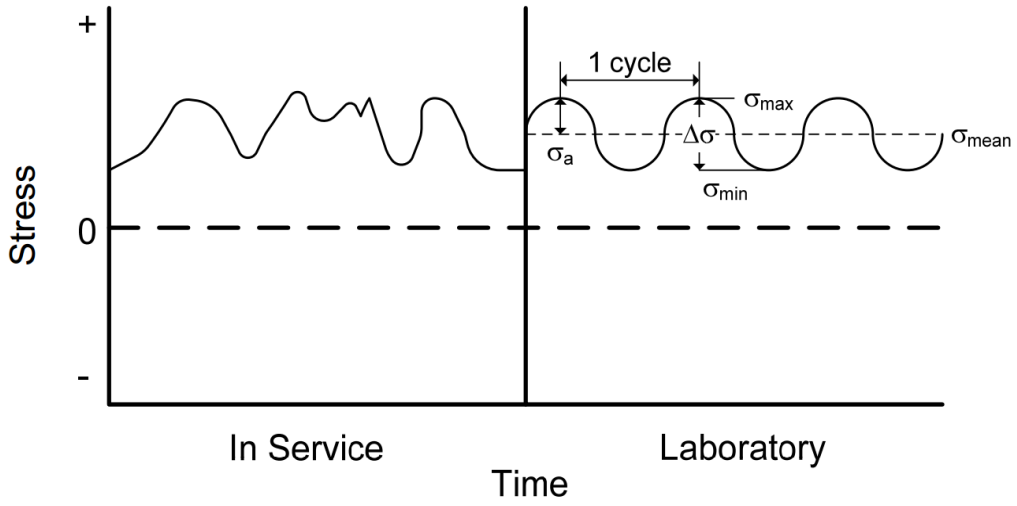

Figure 2. 14 Schematic illustration of stress cycle in in-service and laboratory, and also shows terminologies which are used to characterize fatigue behaviour of materials [169]

Fatigue lives are affected by these loading variables and should be reported along with fatigue results. Many stress loading parameters govern the fatigue lives of specimen including, testing environment, stress amplitude, stress ratio, frequency and mean stress. At a given stress ratio (R), increase in the stress amplitude will increase σ_{max}, $\Delta\sigma$ and σ_{mean} and result in lower fatigue lives. Fatigue results are significantly affected by different mean stresses due to different R values as shown in Figure 2.15 [135,172–175].

Fatigue testing is often performed at a variable mean stress, controlled stress amplitude and fixed stress ratio, but empirical equation exist for relating mean stress effects on fatigue lives [169]. Fatigue behaviour of a metal can also be affected by frequency of loading, particularly if it is greater than 200 Hz for metals [169].

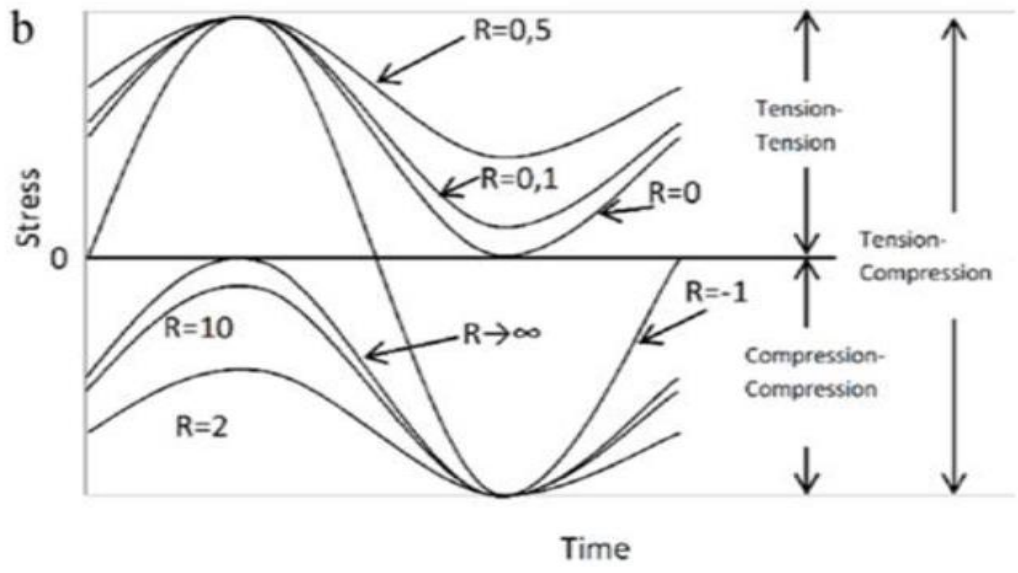

Figure 2. 15 Schematic illustration of different R ratios on spectrum [175]

The number of cycles up to the final failure of the specimen is recorded and the stress amplitude is varied during fatigue testing. A stress-life (S-N) curve is plotted by using this data, as shown in Figure 2.16. S-N curves are different for different alloy systems and materials, and used to design components against fatigue failure. The number of cycles to failure is increased as the stress amplitude is decreased. Endurance or fatigue limit is usually observed at stress levels around 40 % of the tensile strength for steel and other ferrous alloys [169]. The specimen has infinite life at stress amplitude which is below the fatigue limit. Al and other FCC materials show fatigue behaviour which is different from steel and other ferrous alloys because, at low stress amplitude, they do not reach fatigue limit [169]. In such cases, fatigue limit is considered at stress level that give high number of cycles (typically 10^7 cycles) and this limit is used for designing the components [176].

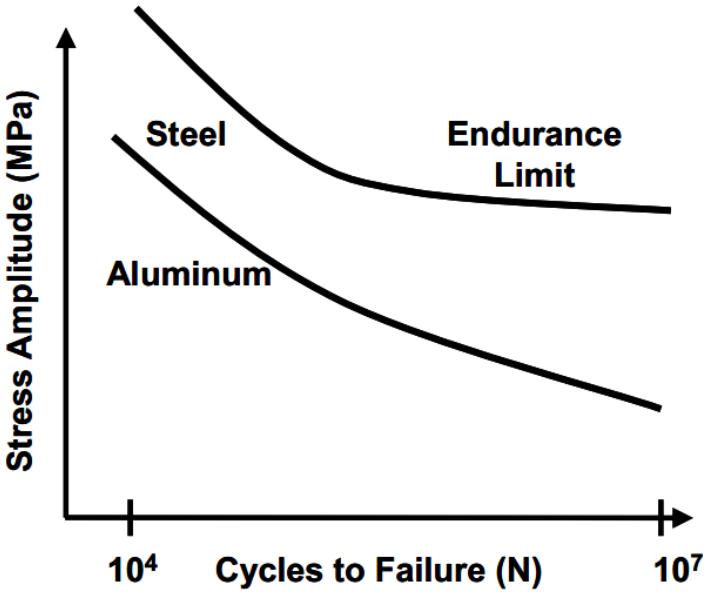

Figure 2. 16 Schematic illustration of a stress-life (S-N) curve [169]

The fatigue behaviour of specimens is not only affected by intrinsic features such as surface finish, microstructure, welds and texture but also by external variables such as exposure to corrosion environment and temperature. Salty environments such as marine environments and environments near ocean severely damage automotive components due to presence of chloride ions. Therefore, it is necessary to consider the dynamic or static effects of corrosion-fatigue. Automotive components also experience elevated temperatures due to braking friction, exhaust gases and transfer of heat from the engine which also affect fatigue behaviour of the material.

2.7 Research gaps and Problem formulations:

Particulate reinforced aluminium matrix composites (PRAMCs) are one of the important engineering materials in the present era. PRAMCs are increasingly preferred and used in many applications in aerospace, automotive and marine industries. Therefore, time-to-time modification on PRAMCs has been made by changing the composition, processing method and reinforced particles size for achieving better mechanical properties. However, the demand for continuous improvement in performance of PRAMCs, through its

improvement of mechanical behaviour, in automobile and aerospace application is ever increasing.

An exhaustive review of the literature on in-situ aluminide reinforced AMCs with effect of UST, and their impression creep and fatigue behaviour have been carried out, and based on the identified research gaps, the problem formulation was made in the present work. The important findings from the literature are summarized below:

Fabrication of in-situ aluminide reinforced AMCs by using ultrasonic assisted casting method is still a novel area of research. Creep and fatigue behaviour investigations have not been done so far to the best of our knowledge on ultrasonically processed in-situ composites. Aluminides as reinforcement particles are harder than the matrix phase and can withstand high temperatures. Homogeneously dispersed intermetallic particles in the aluminium matrix improves high temperature property. Also, their uniform distribution in the base Al alloy can improve its high cycle fatigue as it has been reported in the literature that the presence of small sized reinforced particles in the matrix improves high cycle fatigue.

UST has potential to not only refine the grain structure and disperse reinforced particle uniformly throughout the Al matrix but also eliminate casting defects such as porosity in the AMCs, which will show superior mechanical properties.

Thus, the objectives of the present work are:

1. To fabricate in-situ Al-Al_3Ti and Al-Al_3Zr composites using ultrasonic assisted casting method.
2. To investigate and compare the creep behaviour of Al-Al_3Ti and Al-Al_3Zr composites.
3. To investigate and compare the high cycle fatigue behaviour of Al-Al_3Ti and Al-Al_3Zr composites.

CHAPTER 3
EXPERIMENTAL PROCEDURE AND INSTRUMENTS

This chapter deals with the details of experimental procedure carried out in line with the scope of the work. The procedures of specimen preparation for microstructural characterization (scanning electron microscopy, optical microscopy and transmission electron microscopy) and mechanical testing (hardness and tensile test) are explained.

3.1 Materials:

Commercially available Al6061 alloy was procured from Hindalco, India. Its chemical analysis was done by XRF (Rigaku supermini 200), as shown in Figure 3.1, and presented in Table 3.1. Its melting range is 580 °C - 660 ºC. Potassium hexafluorotitanate (K_2TiF_6) and potassium hexafluorozirconate (K_2ZrF_6) inorganic salt were procured from Madras Fluorine Private Ltd, Chennai, India.

Table 3. 1 Chemical composition of Al6061 alloy

Elements	Mn	Zn	Fe	Cr	Si	Mg	Ti	Cu	Al
Wt. %	0.33	0.003	0.18	0.006	0.70	0.88	0.02	0.29	97.591

3.2 Experimental procedure:

For fabricating different wt. % of Al_3Ti and Al_3Zr reinforced Al composite, the experimental setup used is as shown in Figure 3.2. An ultrasonic system (Model VCX 1500, Sonics and Materials, USA) which was used to generate ultrasonic vibration in the melt is shown in Figure 3.3. It had an air-cooled converter which was made from piezoelectric lead zirconate titanate crystals and was able to produce frequency of 20 kHz. The intensity of this unit could be adjusted from 0 to 5.4 kW/cm^2. In each experiment, about 250 grams of the Al6061 ingot was taken inside a graphite crucible and heated up to 750 °C in an electrical resistance furnace. After holding the melt at 750 ºC for 30 minutes, varying amount of K_2TiF_6 and K_2ZrF_6 (5, 10 and 15 wt. %) was added into the melt to develop composites with

different weight percent (2.7, 5.4 and 8.1 wt. %) of Al_3Ti particles and (3.0, 6.1 and 9.1 wt. %) of Al_3Zr particles as shown in Table 3.2 and Table 3.3, respectively. After addition, the melt was stirred manually for 2 min by using a graphite rod for proper mixing of the powders into the molten metal. After proper mixing of the salt, ultrasonication was carried out at 750 ^oC for 5 min. This is achieved by inserting the niobium probe of 19 mm in diameter and 42 cm in length, coated with zirconia baked at 200 ^oC and preheated to the processing temperature. The amplitude and frequency of ultrasonic stirring was 24 µm and 20 kHz respectively.

After ultrasonication, the melt was poured and allowed to solidify in a mild steel mould of dimension 40 × 40 × 120 mm^3 which was coated with high temperature coating (Zirconia) to avoid any contamination from the mould. The mould was preheated to 400 ^oC to ease the flow and reduce thermal damage to the casting. The solidification conditions were maintained the same for all experiments so that differences in the mechanical properties and microstructure are due to the processing conditions.

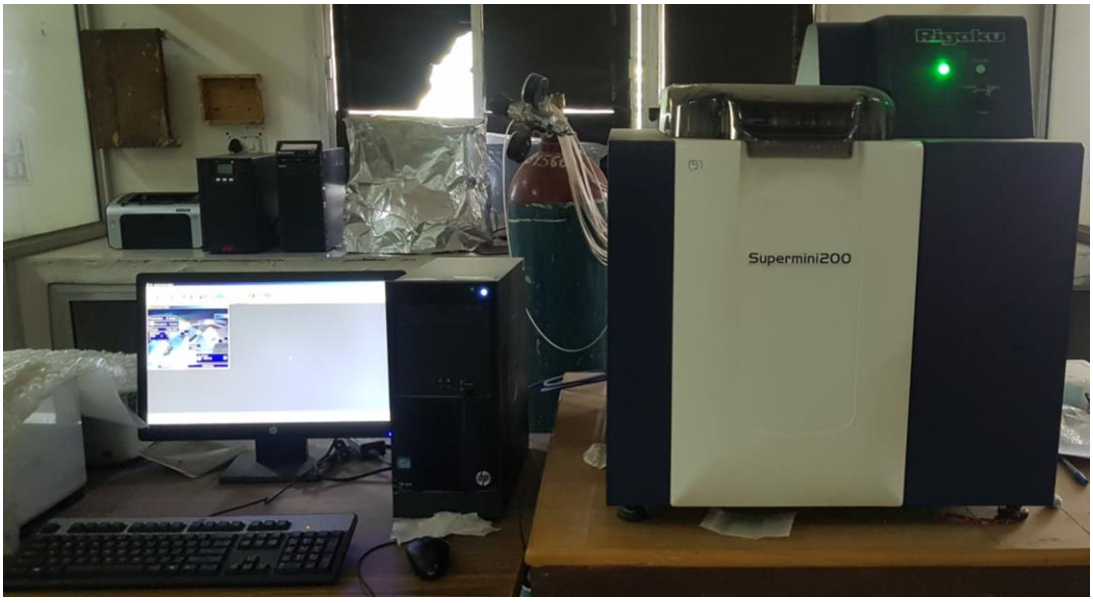

Figure 3. 1 XRF (Rigaku supermini 200) is used for chemical analysis

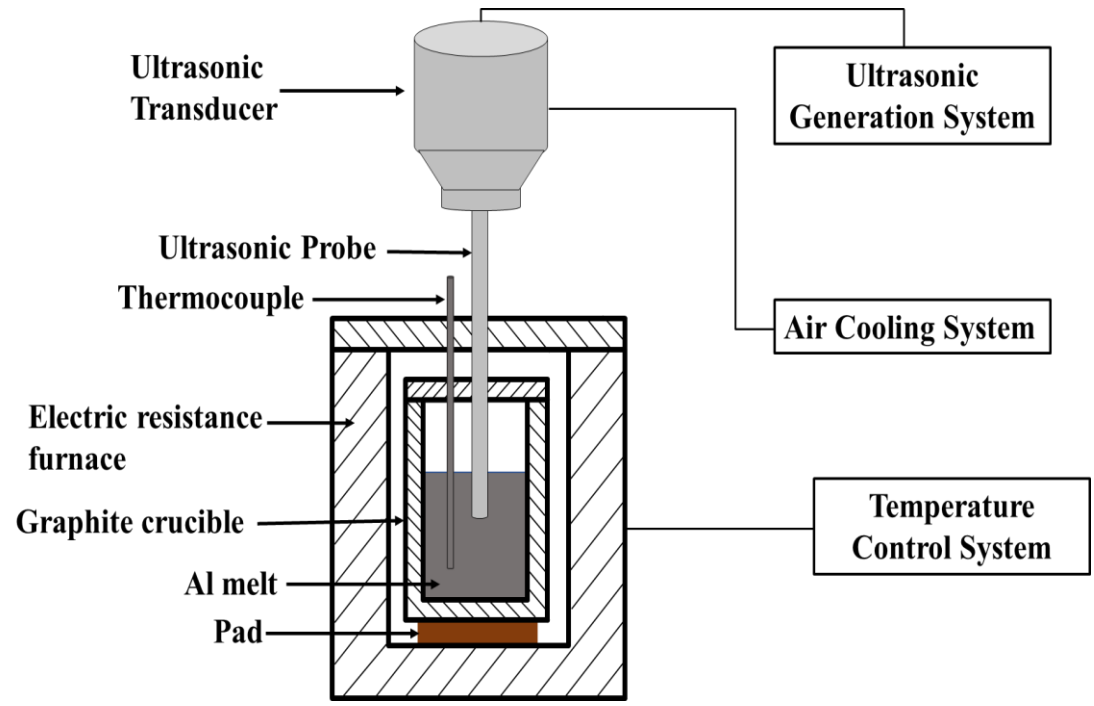

Figure 3. 2 Schematic diagram of ultrasonic assisted casting

Figure 3. 3 Set up for ultrasonic stirring

Table 3. 2 Al_3Ti intermetallic content in each sample with sample labelling

Sample Label	K_2TiF_6 addition (wt. %)	Al_3Ti content (wt. %)
Base Al alloy	0	0
C1U	5	2.7
C2U	10	5.4
C3U	15	8.1

Table 3. 3 Al_3Zr Intermetallic content in each sample with sample labelling

Sample Label	K_2ZrF_6 addition (wt. %)	Al_3Zr content (wt. %)
Base Al alloy	0	0
C*1U	5	3.0
C*2U	10	6.1
C*3U	15	9.1

3.4 Microstructural characterization:

3.4.1 Optical metallography:

Samples were cut, for metallographic analysis, from the cast ingot. Specimen preparation involved grinding in belt grinder using emery paper of 100 grit size followed by manual polishing using 320, 800, 1200, 1500 and 2000 grit size emery papers. Then, cloth polishing was performed on velvet cloth using a mixture of magnesium oxide powder and water. These polished specimens were cleaned in ultrasonic cleaner using acetone. All specimens were etched using Keller reagent. The chemical composition of the Keller reagent is 2 ml HF, 3 ml HCl, 20 ml HNO_3, and 175 ml water.

For microstructural examination, a Zeiss scanning electron microscope (SEM) in secondary electron imaging mode and an optical microscope (Leica DMI 5000 M) were used. To determine the average grain size of the Al matrix, ImageJ software and mean linear intercept method were used.

3.4.1.1 TEM sample preparation:

For TEM specimen preparation, a low speed diamond saw (BUEHLER IsoMet) was used for cutting thin slice (1-2 mm) as shown in Figure 3.4. This thin slice was further thinned down to about 100 µm using paper polishing with 1500 grit size emery paper. For further thinning, dimple grinder (FISCHIONE Model 200) as shown in Figure 3.5 was used to thin down the slice to about 25 µm. At last, dimple grinded slice was placed in ion beam miller (GATAN PIPS II model 695) as shown in Figure 3.6 with dual modulation at 5keV with 6˚ angle of beam to get ion beam polished thin foil for TEM examination.

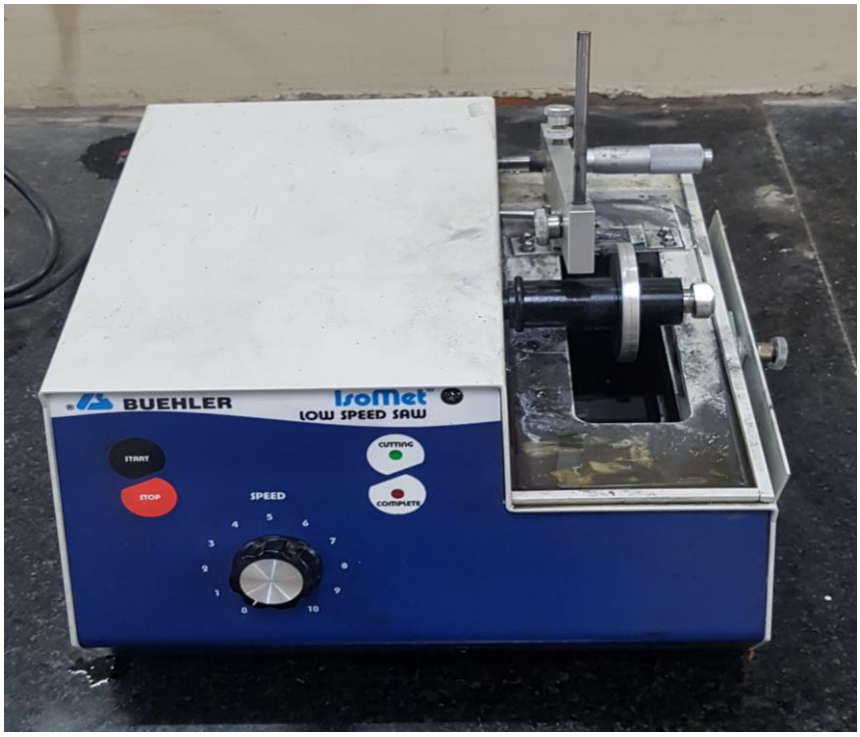

Figure 3. 4 Low speed precision diamond saw cutter

Figure 3. 5 Dimple grinder for creating dimple at the centre of the thin slice

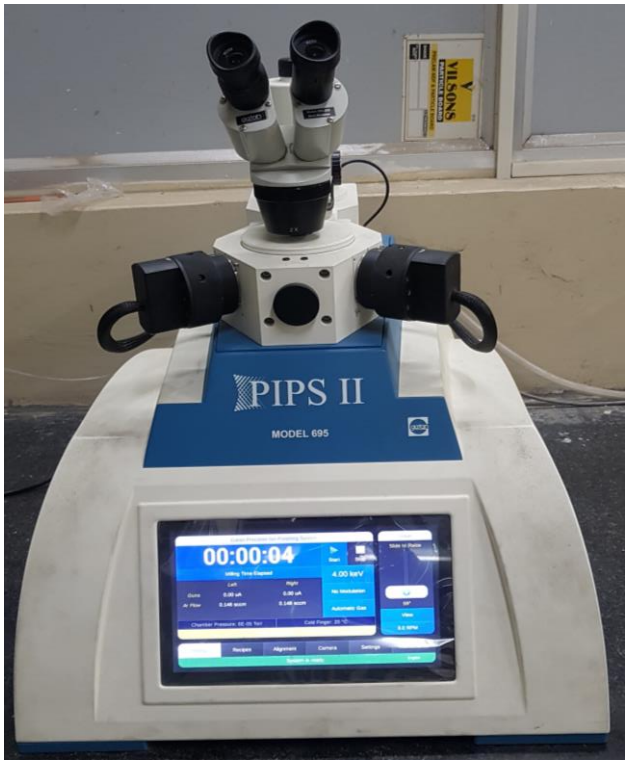

Figure 3. 6 Ion beam miller for ion beam polishing of the thin slice

3.4.2 Instruments used in microstructural characterization:

3.4.2.1 Optical microscope:

A Leica DMI 5000M microscope which was used for optical microscopy is shown in Figure 3.7. Microstructures were captured digitally at different magnifications (5x, 10x, 20x, 50x, and 100x) at various locations in the specimens. In general, this instrument has light source, objective lens, condenser and ocular or eyepiece. A recording device can replace the eyepieces. In research, optical microscopy is used for the inspection, analysis, and recording of microstructure of materials.

3.4.2.2 Scanning electron microscope:

The image of ZEISS EVO 18 scanning electron microscope (SEM) is shown in Figure 3.8. The SEM with energy dispersive X-ray spectroscopy (EDS) and electron backscattered diffraction (EBSD) The SEM acquired the microstructural characteristics and elemental analysis of the aluminium alloys and composites specimens. The fracture surface analysis was performed for identifying the type of fracture that occurs during tensile tests. An EDS spectrometer was used for detecting different elements present in the composites.

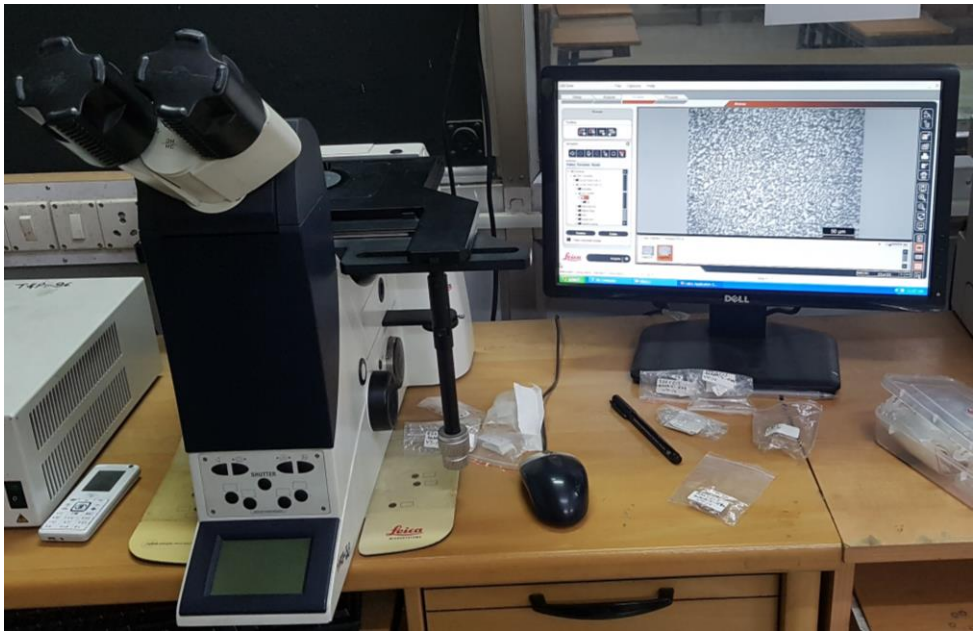

Figure 3. 7 Leica (DMI 5000M) optical microscope was used for optical microscopy

Figure 3. 8 ZEISS EVO 18 Special Edition scanning electron microscope used for characterization of in-situ aluminide reinforced aluminium alloy composites.

3.4.2.3 Transmission electron microscope:

The electron microscopy of the specimens was also performed using a transmission electron microscope (TEM) (JEOL JEM-3200FS) as shown in Figure 3.9. The TEM was operated at accelerating voltage of 300 kV. The TEM provides information about the size, morphological, compositional, and crystallographic characteristics. In the present study, TEM study was used for the analysis of interface between the reinforced particles and the matrix, and dislocations and their interactions in the matrix phase.

3.4.2.4 X-ray diffraction (XRD):

XRD is an analytical method which is used for phase identification, phase quantification, and for determining the lattice parameter, crystallite size, and dislocation density of the materials. In the present work, XRD (Rigaku SmartLab, Japan) equipment, as shown in Figure 3.10, was used for identification of different phases present in the composites. X-ray diffraction patterns were obtained by using Cu K_α radiation whose wavelength is 1.54 Å with 2θ ranging from 10º to 120º. For all the diffraction peaks and

corresponding values of 2θ, the inter-planer spacing, d, was calculated using the Bragg's law. For identifying the various phases, JCPDS X-ray diffraction database was used.

3.5 Mechanical testing:

Different mechanical testing procedures used for aluminium alloys and aluminium alloy composites are discussed in the following sections.

3.5.1 Hardness tester:

Hardness tests were performed on Brinell hardness tester (Heckert HPO-250), as shown in Figure 3.11, employing 15 kg load and dwell time 10 s. The ball diameter is 2.5 mm. An average of at least five hardness readings was taken and reported along with standard deviation.

Figure 3. 9 Transmission electron microscope used for characterization of in-situ composites

3.5.2 Tensile testing machine:

Tensile testing machine (H25 K-S Tinius Olsen) with constant cross head speed of 0.1 mm/min was used to perform tensile test at room temperature, as shown in Figure 3.12. The gauge length and diameter of tensile specimen was kept according to the ASTM E8M standard which was 20 mm and 4 mm, respectively. According to ASTM B557, tensile test was carried out with a strain rate of 10^{-3}/s. The average value of three tensile tests is reported along with standard deviation. The tensile strength and ductility of the composites were evaluated from the stress-strain data.

Figure 3. 10 XRD (Rigaku SmartLab) is used for phase identification of the composites

Figure 3. 11 Brinell hardness testing machine (Heckert HPO-250) used for the measuring the hardness of the composites.

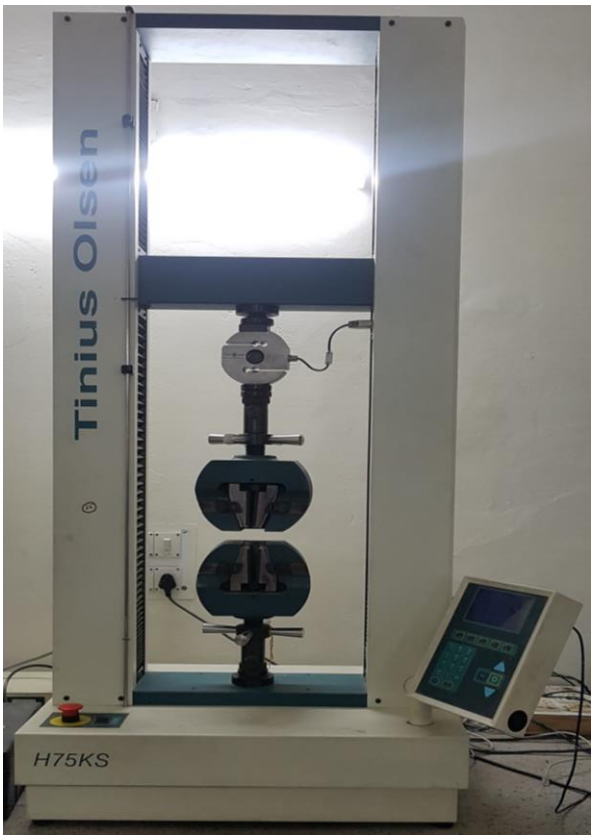

Figure 3. 12 H25 K-S Tinius Olsen tensile testing machine used for the tensile testing of the composites.

3.5.2 Impression creep machine:

Impression creep tests were carried out on an indentation creep machine (Spranktronics, India) which consist of a linear variable displacement transducer (LVDT), vacuum chamber, a lever arm and a data acquisition system as shown in Figure 3.13. Vacuum chamber contains PID controlled furnace, sample holder, indenter holder and indenter made up of tungsten carbide, as shown in Figure 3.14. To carry out the experiment, samples of size 15 mm × 15 mm × 6 mm were cut from each casting by using a diamond cutter. At specific temperature and load, a tungsten carbide indenter of 1.5 mm in dia. was made to indent the surface of sample and the creep rate was obtained from the curve plotted between depth of indentation and time.

Creep is of engineering significance at a temperature, $T > 0.5\ T_m$ [25], where T_m is absolute melting temperature in Kelvin scale. For Al alloy, T_m is 933 K and therefore $0.5\ T_m$ is ~ 467 K. So, the test temperature for creep analysis should be higher than 467 K [26]. Therefore, the impression creep tests were carried out on base Al alloy and the composites at three different temperatures (543 K, 573 K and 603 K) and three different stresses (113 MPa, 141 MPa and 170 MPa) for 10,000 s under a vacuum of 10^{-7} Pa.

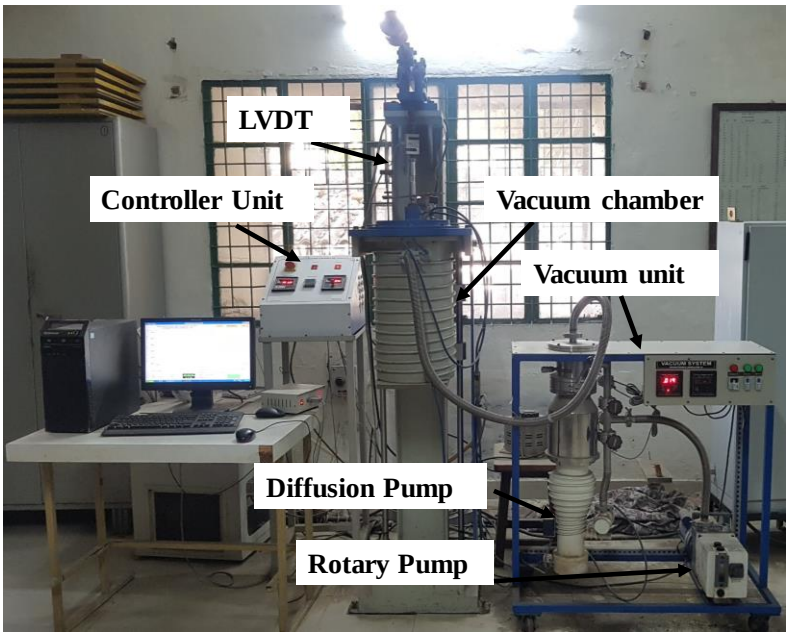

Figure 3. 13 Impression creep machine set up

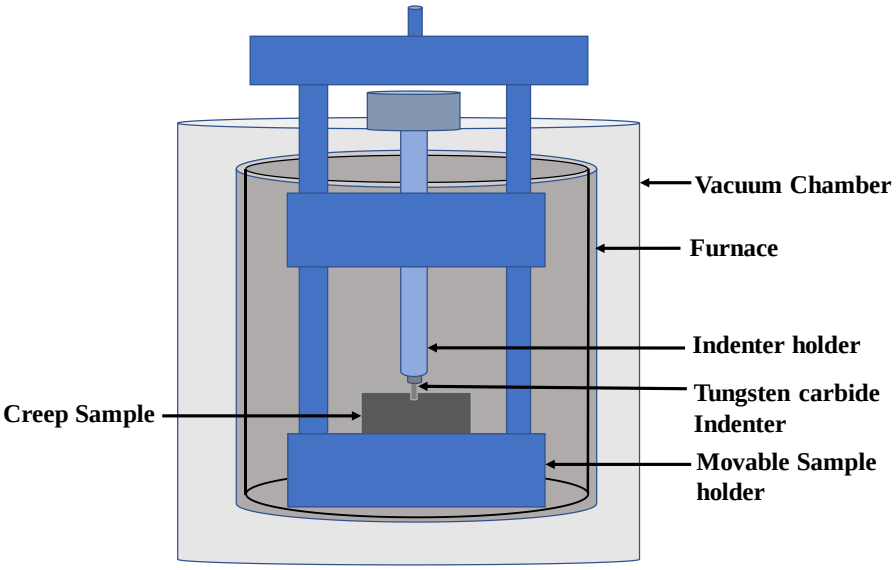

Figure 3. 14 Schematic diagram of setup inside vacuum chamber

3.5.3 Fatigue testing machine:

The fatigue resistance of the base Al alloy and the composites are investigated by performing fatigue test on servo hydraulic axial fatigue testing machine (INSTRON 8802) with load cell of 50 kN at a stress-controlled mode as shown in Figure 3.15. The samples were prepared according to the ASTM E466-07 standard as shown in Figure 3.16. The fatigue tests were performed under constant stress amplitude on axially loaded specimens. For all the processed conditions, the stress ratio (R) value was taken to be 0.1 and the test frequency was maintained at 50 Hz. Scanning electron microscope (Carl Zeiss, EVO 18) in secondary electron imaging mode was used to analyse fracture surface of the fatigue samples.

Figure 3. 15 Instron 8802 machine used for high cycle fatigue and 50 kN load cell

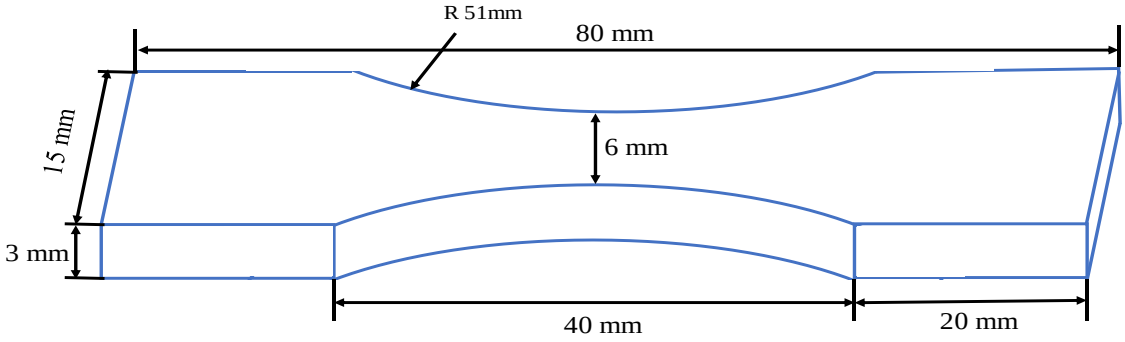

Figure 3. 16 Schematic diagram of a specimen for high cycle fatigue

CHAPTER 4
RESULTS AND DISCUSSIONS

4.1 Processing of in-situ Al-Al_3Ti and Al-Al_3Zr composites:

Liquid Metallurgy approach to processing of aluminium matrix composites (AMC) is economical and favours large scale production based on established technology. Reinforcements like carbides, nitrides, oxides and borides are common to AMCs [177,178,187–195,179–186]. In in-situ processing, the reinforcement particle is formed within the matrix phase as a result of favourable chemical reaction. Consequently, the second phase is thermodynamically stable and uniformly dispersed throughout the matrix with a clean interface [196–199]. As a result, in-situ formed composites demonstrate improved mechanical properties [11].

Several investigations have reported on ceramic reinforced AMCs [200–204]. The making of these composites has some limitations due to the significant difference in the coefficient of thermal expansions (CTE) between the matrix and reinforcement phase. On the contrary, intermetallic compounds are an appropriate choice for reinforcement due to their low density and high modulus. Aluminides, such as Al_3Fe, Al_3Ni, Al_3Zr and Al_3Ti have attracted attention due to their excellent mechanical properties, high specific strength, and high specific modulus, good oxidation and corrosion resistance [62,205,206]. Among these aluminides, tetragonally structured Al_3Ti [37] and Al_3Zr [39] have attracted lot of attention due to their low density (3.4 and 4.11 g/cm^3, respectively), good thermal stability due their high melting point (1350 and 1580 ˚C, respectively) and high Young's modulus (217 and 205 GPa, respectively) [38,40–42]. Moreover, these particles act as heterogeneous nuclei which lead to the grain refinement of α-Al phase [207]. Orowan strengthening, load transfer and grain size strengthening are the major strengthening mechanisms in aluminide reinforced composites [89,208,209].

The presence of porosity is detrimental to the casting. The major cause for porosity in aluminium castings is the presence of dissolved hydrogen in molten metal (0.3 – 0.5 cm^3 per 100 g), which is more than the industry standard of about 0.1 cm^3 per 100 g [210]. For degassing, purifying and refinement of metallic melts, ultrasonication is a viable option, as it is both environment-friendly and economical [109,112,117,211]. In ultrasonic processing, high intensity acoustic wave interacts with molten metal producing nonlinear effects which include acoustic streaming, acoustic radiation pressure, cavitation and emulsification [91]. These effects contribute to the better distribution of the second phase, elimination of columnar dendritic structure and refinement of equiaxed grains [109]. The mechanism behind grain refinement is related to the formation of micro "hot spots" which sustain only for a few nanoseconds in the molten metal during ultrasonic vibration. These hot spots attain a temperature of the order of 5000^oC with heating and cooling rates close to 10^{10} K s^{-1}, and localized pressure approaching 1000 atm [21].

In this work, in-situ Al_3Ti and Al_3Zr particles are formed by reacting K_2TiF_6 and K_2ZrF_6 inorganic salt, respectively with molten Al at 750 ˚C. For uniform dispersion of the particles, high intensity ultrasonic vibrations are applied to the melt. It is well established that the mechanical properties of the composite are significantly improved when there is a uniform dispersion of in-situ formed particles and less percentage of porosity. Therefore, an effort is made to use low cost salt-metal reaction route to fabricate Al_3Ti and Al_3Zr reinforced Al composite.

4.1.1 Properties:

When Al melt, maintained at 750 ˚C, reacted with K_2TiF_6 and K_2ZrF_6 salt, exothermic reaction took place between Al and salt [212].

$$3K_2TiF_6 + 13Al \rightarrow 3Al_3Ti + K_3AlF_6 + 3KAlF_4 \quad (4.1)$$

$$3K_2ZrF_6 + 13Al \rightarrow 3Al_3Zr + 2K_3AlF_6 + 2AlF_3 \quad (4.2)$$

Gibbs free energy for the formation of Al_3Ti at 750 ^oC (1023 K) is -122.8 kJ/mol [213,214]. For the formation of Al_3Zr at 750 ˚C (1023 K), Gibbs free energy is -31 kJ/mol [215] which confirms that reaction between inorganic salts and aluminium takes place spontaneously.

4.1.1.1 Microstructure:

XRD analysis of Al composite with varying amount of K_2TiF_6 and K_2ZrF_6 salt addition into the melt was conducted to determine phases present in the developed composites as shown in Figure 4.1 and 4.2, respecively. It confirms the formation of in-situ Al_3Ti and Al_3Zr particles as corresponding peak is clearly observed as shown in Figure 4.1 and 4.2, respectively. Moreover, as the amount of salt increased, relative intensity of Al_3Ti and Al_3Zr particle also increased. Intermetallics phases other than Al_3Ti and Al_3Zr, and elemental Ti and Zr were not observed which suggested that reaction between molten Al and salts was completed within the time duration.

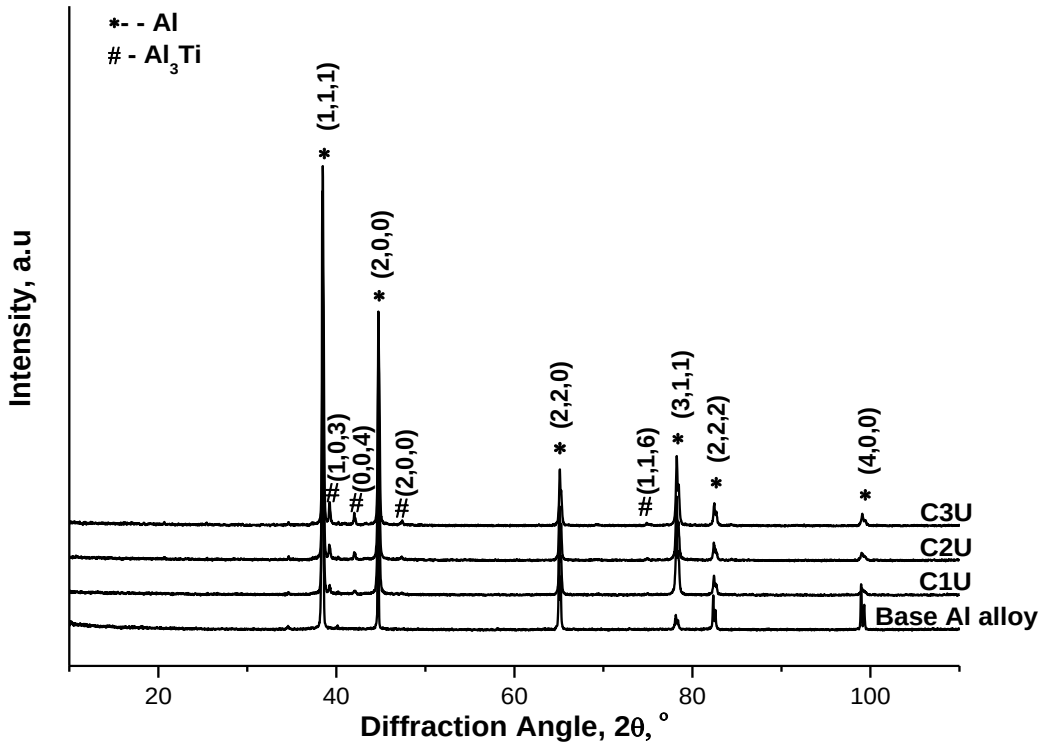

Figure 4. 1 XRD patterns of the base Al alloy and Al_3Ti reinforced Al alloy composites

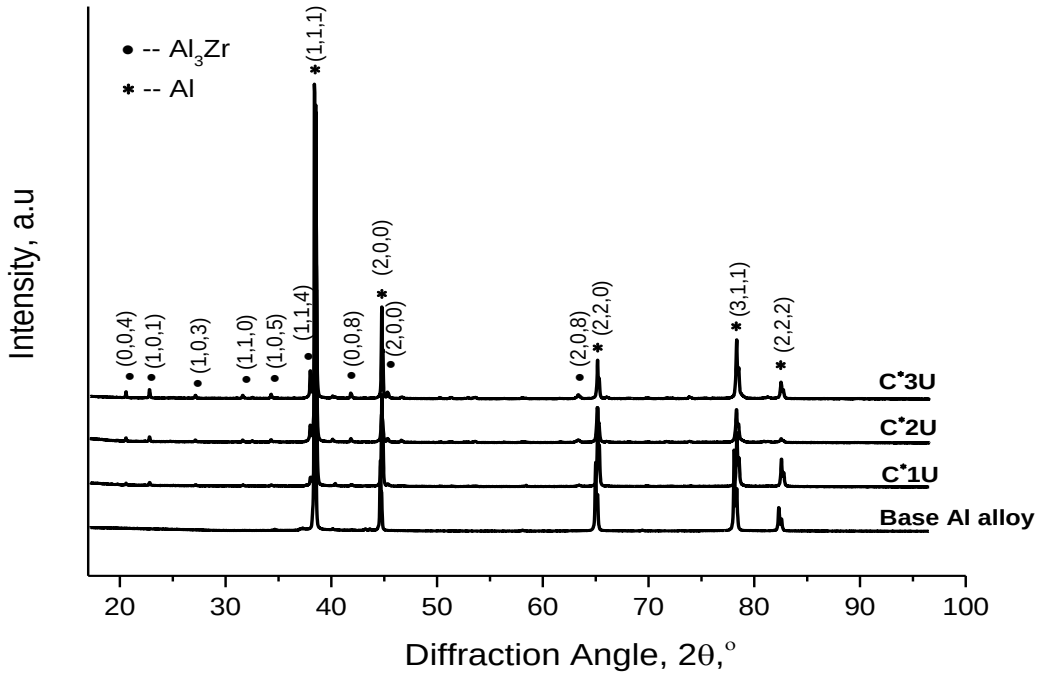

Figure 4. 2 XRD patterns of the base Al alloy and Al_3Zr reinforced Al alloy composites

Optical micrograph of base Al alloy, Al_3Ti reinforced composite, as shown in Figure 4.3, and Al_3Zr reinforced composite, as shown in Figure 4.4, reveals the uniform dispersion of reinforced particles throughout the matrix. The dark spots appeared in the microstructure is Al_3Ti particles (Figure 4.3) and Al_3Zr particles (Figure 4.4) which is confirmed by EDAX analysis as shown in Figure 4.5 and Figure 4.6, respectively. With higher amounts of salts addition, more intermetallic particles form which tend to agglomerate during casting to minimize the overall interfacial energy [128]. The uniform distribution is achieved when high intensity ultrasonic vibrations is applied into the Al melt. During ultrasonic treatment, nonlinear effects such as cavitation and acoustic steaming are produced when ultrasonic field is injected into the molten metal. According to the cavitation phenomena, during rarefaction phase of the acoustic waves, tensile stress is generated which result in the formation of small cavities throughout the molten metal. These cavities grow in size due to inertia, a stage comes when the size of the bubbles become unstable and collapse under compressive stress which is generated during the compression phase. The sound pressure (P) in the travelling wave can be calculated according to

$$P_k = \sqrt{\frac{2P\ c\ \rho_L}{S}} \quad 4.3$$

where ρ_L is the melt density in (g cm^{-3}), P (kW) is the output power of the ultrasonic generator, c is the speed of sound in the melt (m s^{-1}) and S (cm^2) is the probe-face area [216–218]. In our experiment, ρ_L = 2.37 g cm^{-3}, c = 1.3×10^3 m s^{-1} [27], P = 1.5 kW and S = 2.8 cm^2, thereby, P_k = 5.7 MPa, which is much higher than the threshold value of 1 MPa [217] for generating acoustic cavitation. Under the effect of high-pressure pulse, the particle clusters are broken and dispersed throughout the matrix. The dispersion is facilitated by acoustic streaming, which is a form of turbulence developed near obstacles when there is a loss in wave energy. To produce these effects, fully developed cavitation must occur into the molten metal which depends upon the intensity (I) of the ultrasonic vibration. The intensity of ultrasonic vibration is defined by

$$\mathrm{I} = \frac{1}{2}\rho_L c(2\pi f A)^2 \quad 4.4$$

where ρ_L is the melt density (g cm^{-3}), f is the frequency (Hz), A is the amplitude (μm) and c is the speed of sound in the melt (m s^{-1}) [109,128]. High-intensity ultrasonic vibration requires I ≥ 100 W cm^{-2}. Moreover, the fully developed cavitation occurs in the molten aluminium alloys when I ≥ 80 W cm^{-2} [109,128]. In our experiment, A = 24 μm, ρ = 2.37 g cm^{-3}, c = 1.3×10^3 m s^{-1}, and f = 20 × 10^3 Hz, thereby I = 1400 W cm^{-2}, which is far greater than the threshold value. The effect of cavitation produced by the ultrasonic vibration in the melt is confirmed by the well dispersed Al_3Ti and Al_3Zr particles shown in the microstructure of the ultrasonically treated melts.

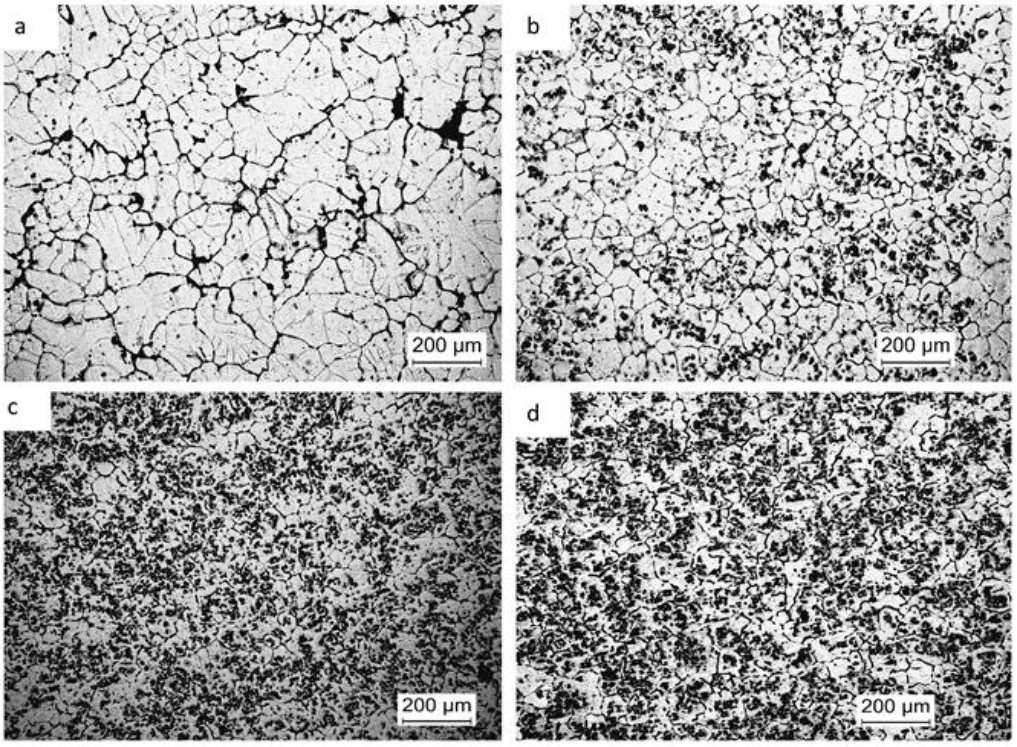

Figure 4. 3 Optical micrographs show microstructure of (a) base Al alloy; (b) C1U; (c) C2U and (d) C3U showing uniform distribution of the Al_3Ti particles throughout the matrix

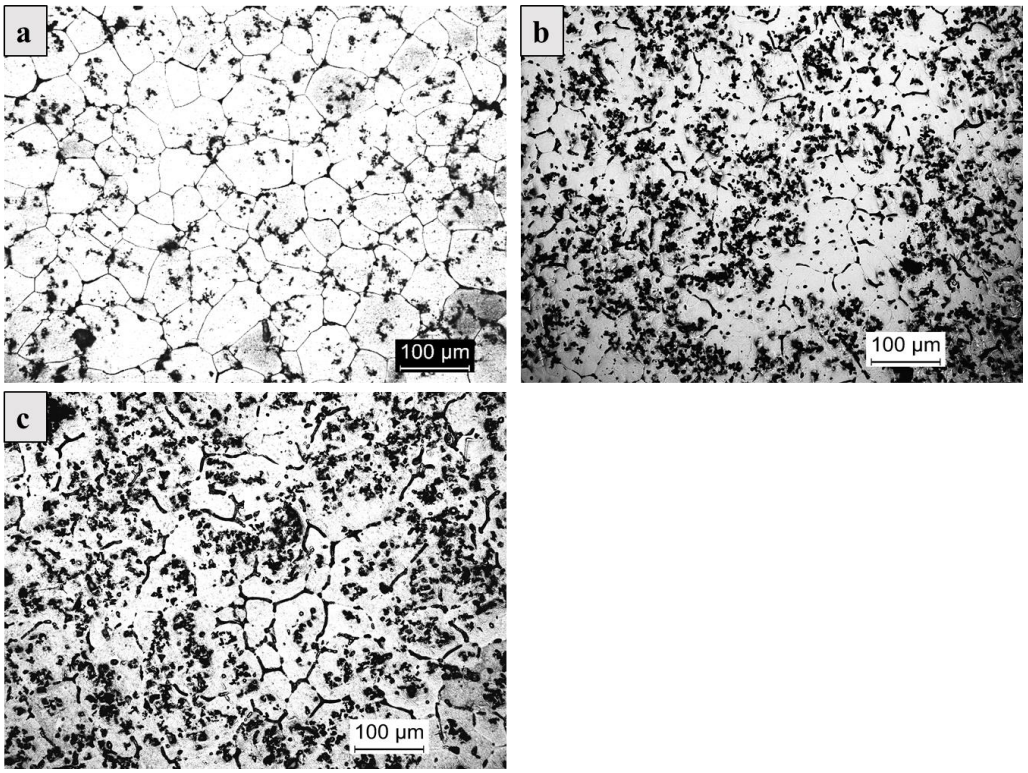

Figure 4. 4 Optical micrographs show microstructure of (a) C*1U; (b) C*2U and (c) C*3U showing uniform distribution of the Al_3Zr particles throughout the matrix

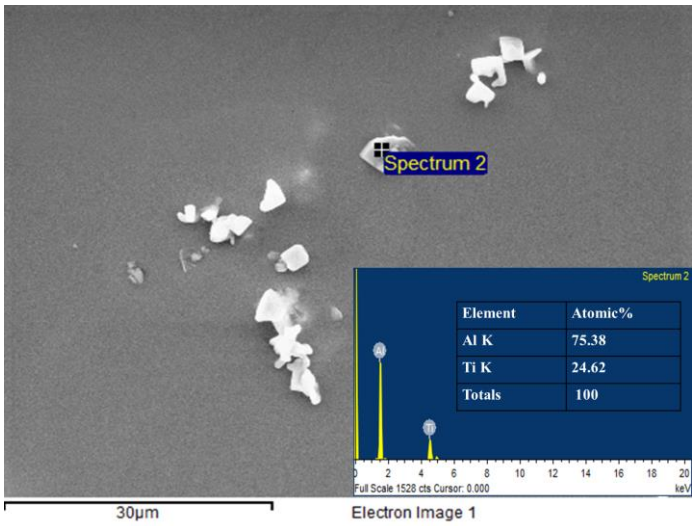

Figure 4. 5 SEM micrograph shows in-situ formed Al_3Ti particles in the matrix. Inset in shows the energy spectra corresponding to the Al_3Ti particles and atomic percentage of its elements

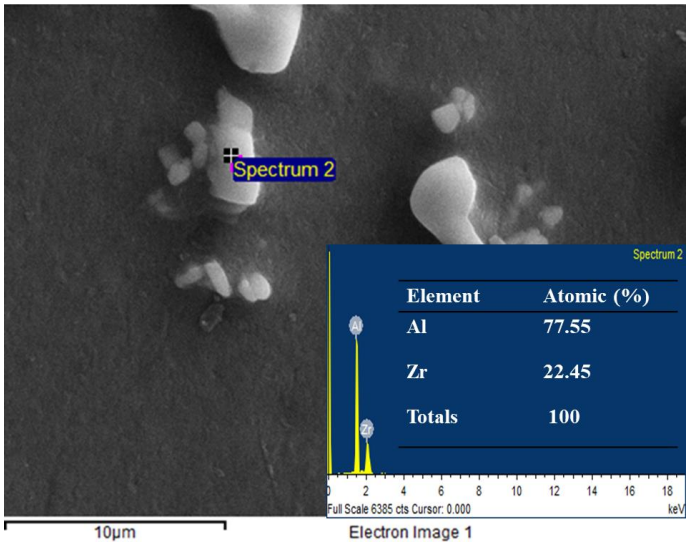

Figure 4. 6 SEM micrograph shows in-situ formed Al_3Zr particles in the matrix. Inset in shows the energy spectra corresponding to the Al_3Zr particles and atomic percentage of its elements

The average grain size of the composites is shown in Figure 4.7. It is observed from the figure that the grain size of composites decreases with increase of the particles, suggesting that in-situ formed particles can act as an effective grain refining agent during solidification. The interfacial energy between the solid matrix and the nucleating substrate plays an important role in microstructure refinement. If the solid and the substrate are coherent or partially coherent, the interfacial energy will be low. The following equation can be used to evaluate the lattice misfit, δ, between the substrate and the matrix:

$$\delta = \left|\frac{a_{matrix} - a_{substrate}}{a_{matrix}}\right| \quad 4.5$$

where $\alpha_{substrate}$ and α_{matrix} are the lattice constants of the substrate and the matrix, respectively. As a rule, the interface between the matrix and the substrate is coherent when $\delta \leq 0.05$ and partially coherent when $0.05 < \delta < 0.25$ [219].

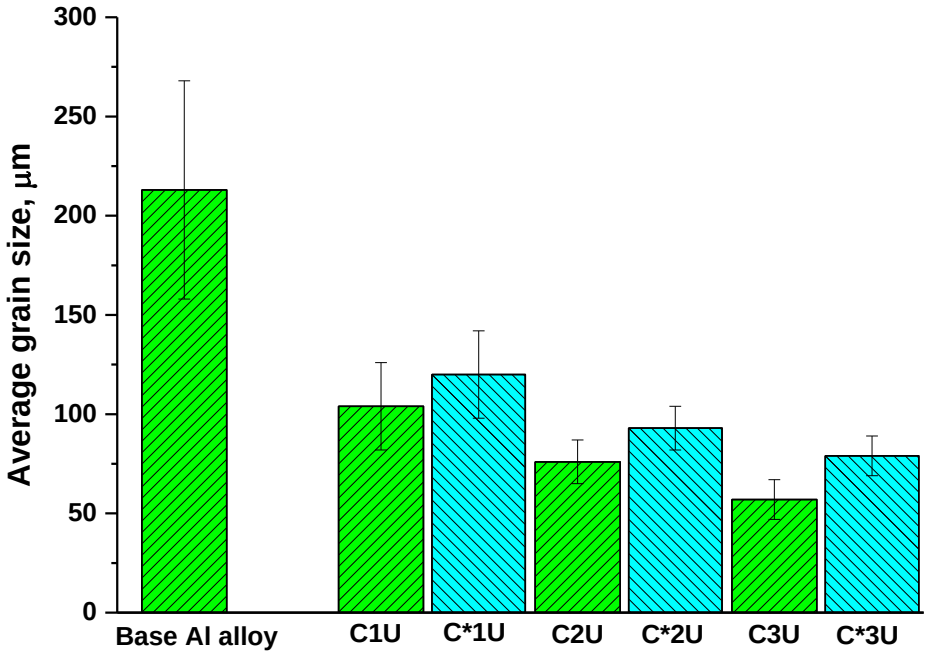

Figure 4. 7 Variation in grain size of base Al alloy and the composites.

The crystal structure of Al_3Ti ($D0_{22}$) is tetragonal with $a = b = 0.385$ nm and $c = 0.861$ nm [220]. The crystal structure of Al_3Zr ($D0_{23}$) is also tetragonal with $a = b = 0.4009$ nm and $c = 0.864$ nm [221]. On the other hand, α-Al crystal has a fcc structure with $a = b = c = 0.404$ nm [222]. So, the lattice misfit values between in-situ formed Al_3Ti and α-Al in both *a* and *c/2* directions are 0.049 and 0.065, respectively whereas the lattice misfit values between in-situ formed Al_3Zr and α-Al in both *a* and *c/2* directions are 0.069 and 0.008, respectively. On the basis of this calculation, it can be concluded that in-situ formed Al_3Ti and Al_3Zr particles have a good lattice match with α-Al and can act as an effective heterogeneous nucleating site for primary Al during solidification. The size distribution of the Al_3Ti and Al_3Zr reinforced particles in the composites was characterized by Image J software as shown in Figure 4.8 and Figure 4.9, respectively. It was observed that about 75%

of Al_3Ti particles are between 2 µm and 4 µm in size whereas, around 70 % of Al_3Zr particles have size less than 2 µm. The average size of Al_3Ti and Al_3Zr particles is about 3.4 ± 1.2 µm and 1.8 ± 0.8 µm, respectively.

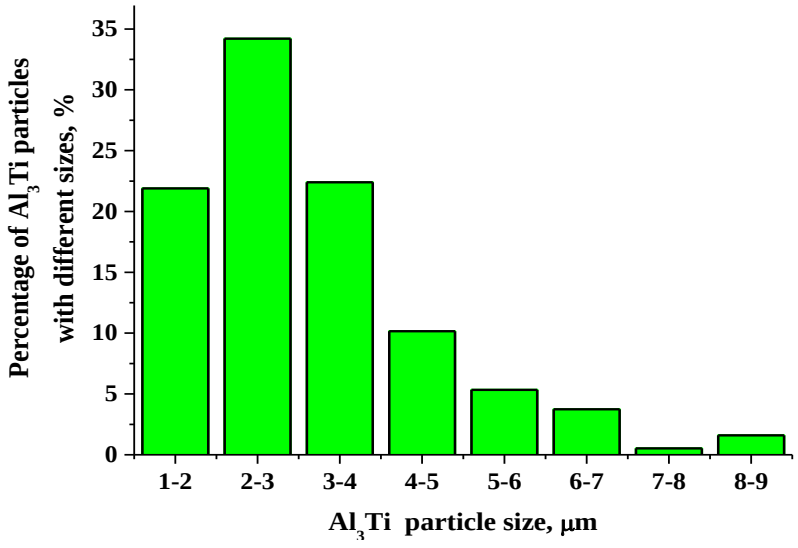

Figure 4. 8 Size distribution of in-situ Al_3Ti particles in the composite.

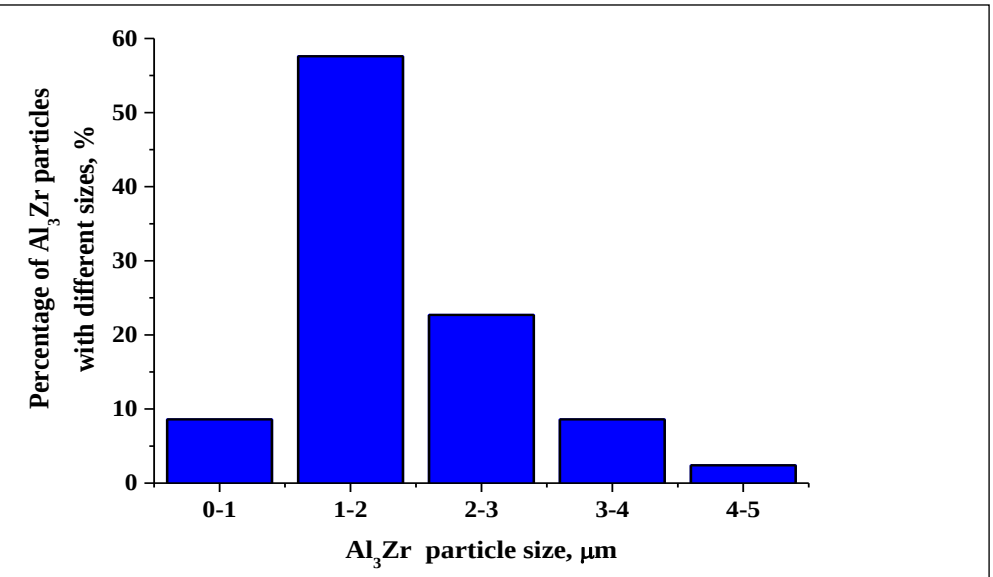

Figure 4. 9 Percentage of different sizes of Al_3Zr particles in the composite

Grain refinement due to Al_3Zr and Al_3Ti particles can also be understood with the help of Al-Zr and Al-Ti phase diagram obtained by using thermo-cal software (Figure 2.4 and 2.5, respectively). According to the phase diagram, the peritectic reaction takes place according to:

$L + Al_3Ti \rightarrow \alpha\ Al$ (at 665 ˚C) 4.6

$L + Al_3Zr \rightarrow \alpha\ Al$ (at 665 ˚C) 4.7

The reaction product of the above equations is a new phase precipitated on Al_3Ti and Al_3Zr which acts as a heterogeneous nucleating agent. This is confirmed by the microstructures shown in Figure 4.3 (b-d) and Figure 4.4 (a-c).

From mechanical properties point of view, thermodynamically unstable particles can be detrimental because they can form reaction product around the reinforcing particles by reacting with molten metal [223]. Therefore, clean interface between the particle and the matrix is always desired which enhance the capacity of the composite to bear load and hence, mechanical properties are improved. Figures. 4.10 (a) and 10 (b) show TEM micrographs of the area containing Al_3Ti particle and SAED pattern of an Al_3Ti particle, respectively. It is evident from the TEM analysis that the interface between the Al matrix and Al_3Ti particles is clean (Figure 4.10 a) without the presence of porosity or any reaction product. The in-situ formation of Al_3Ti particles within melt reduces the possibility of oxidation of the particles, thus improving the interfacial bonding between matrix and particles [224,225]. Dislocations around the Al_3Ti, which are generated due to difference in CTE between matrix and particles, also contribute to strength and hardness of the composites (Figure 4.10 a). The TEM micrographs of the Al_3Zr reinforced composite is shown in Figure 4.11. High dense dislocations are noticed around Al_3Zr particulates and in the aluminium matrix as shown in Figure 4.11 (a-c). These dislocations are generated when there is a significant difference in CTE between the matrix (CTE of Al: $25.2 \times 10^{-6}\ K^{-1}$[226]) and the reinforced particles (CTE of Al_3Ti: $13.0 \times 10^{-6}\ K^{-1}$ [227] and Al_3Zr: $15.5 \times 10^{-6}\ K^{-1}$ [221]). This difference in CTE creates volumetric strain in the composites which produce geometrically necessary dislocations (GND) around the particles [228–232]. The SAED pattern of an Al_3Zr particles which confirms that the Al_3Zr particles formed in the composites are tetragonal in structure as shown in Figure 4.11 (d). The interface between the Al matrix and the Al_3Zr particle is

shown in Figure 4.11 (e). The interface is free from micro pores, undesirable reaction product, and is continuous and plain which indicate that Al_3Zr is well bonded with Al matrix. This improvement in interfacial bonding between the particles and the matrix can be attributed to the formation of particles within the melt which limits the chance of the particles to get oxidized [225]. The absence of oxidized surface not only enhance wettability by reducing wetting angle between the Al_3Zr particles and the Al matrix but also enhance interfacial integrity [199]. Due to exothermic nature of the reaction, the increase in the temperature of molten Al further ensures good wettability. Although homogeneous distribution enhances mechanical properties, good interfacial bonding is also desired. The HRTEM of the selected area of the interface, marked by yellow box in the Figure 4.11 (e), is shown in Figure 4.11 (f) which confirms that the interface is coherent with the small lattice misfit between Al and Al_3Zr. It is observed from (Inverse Fast Fourier Transform) IFFT image of the outlined area, marked by yellow box in Figure 4.11 (f), that the fringes of Al_3Zr particle are aligned along (004) plane and there interplanar spacing is 0.227 nm.

The experimental density of the base Al alloy and composites was calculated by Archimedes principle [233]. The porosity content P in the composite specimens is determined as

$$P\ (\%) = (1 - \frac{\rho}{\rho_o}) \times 100 \qquad 4.8$$

where the actual density of the specimen ρ is obtained by Archimedes' method: $\rho = W_a/(W_a - W_w)$ where W_a and W_w are the weight of samples in the air and the weight of samples in water, respectively. The theoretical density ρ_o is calculated using the rule of mixture: $\rho_o = V_{f,p} \times \rho_p + (1 - V_{f,p}) \times \rho_m$, where $V_{f,p}$ is the volume fraction of the particle (Table 5), ρ_p is the density of the particle which is 3.4 g cm^{-3} and 4.14 g cm^{-3} for Al_3Ti and Al_3Zr, respectively and ρ_m is the density of the matrix (2.7 g cm^{-3}). The values of theoretical density and actual density for Al_3Ti and Al_3Zr reinforced composite are shown in Table 4.1. The percentage of porosity of the composites is found to be lower than that of the base Al

alloy because of ultrasonic degassing. Degassing of the melt during ultrasonication happens in three stages [128]: Stage I: Bubbles are formed in the melt and their sizes increase due to transformation of gasses from the surrounding melt. Stage II: These bubbles get consolidated and form large bubbles. Stage III: The large bubbles float to the top surface of the liquid metal and collapse releasing gas to the environment. So, when the duration of ultrasonic stirring is increased, the dissolved gases in the liquid metal are removed effectively and composites with less porosity can be formed.

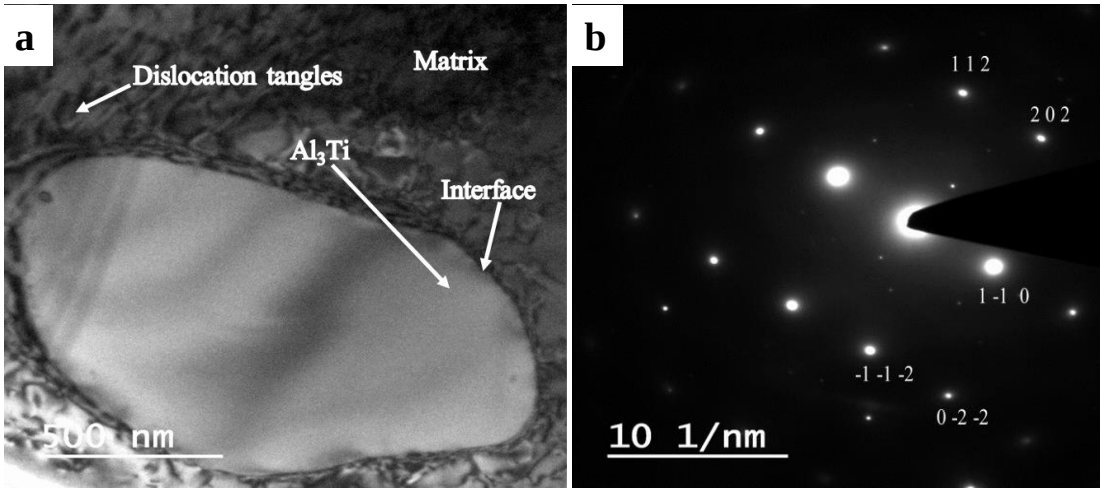

Figure 4. 10 TEM micrograph (a) showing clear interface between in-situ Al_3Ti particles and Al matrix. Dislocation tangles are present around the particles contributing to the strength and hardness of the composite. (b) SAED pattern of Al_3Ti particle.

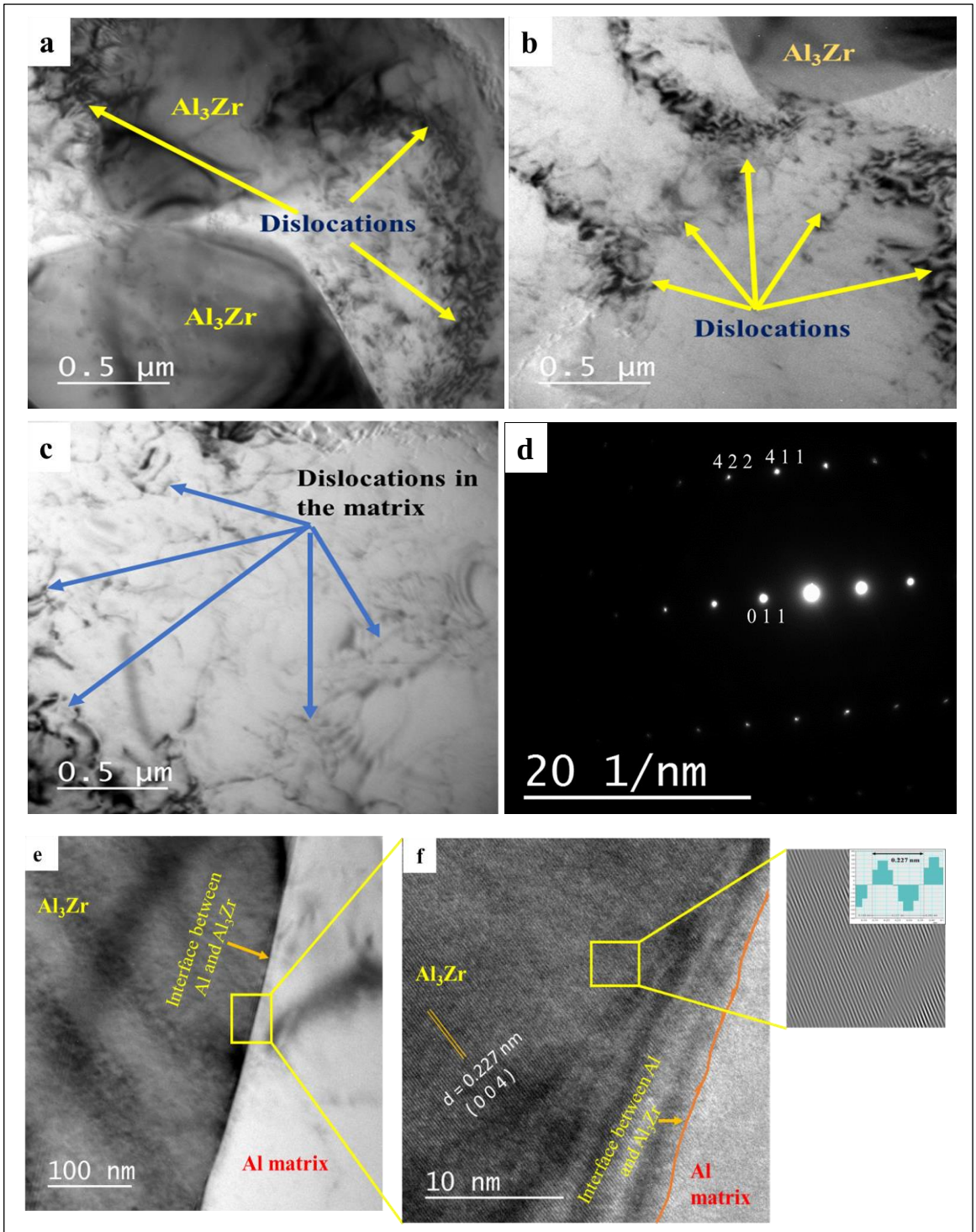

Figure 4. 11 TEM micrograph (a) and (b) showing the generation of dislocations around the particles which contributes to the strength and hardness of the composite, (c) showing the dislocations in the matrix, (d) SAED pattern of the Al_3Zr particle which confirms the tetragonal structure ($D0_{23}$) of the Al_3Zr, (e) indicate clean interface between Al matrix and in-situ Al_3Zr particles, (f) showing HRTEM of the interface between particle and matrix, and (g) showing IFFT (inverse fast Fourier transform) image to calculate the interplanar spacing.

Table 4. 1 Density and porosity of as cast base Al alloy and composites.

Material developed	Theoretical density ($g\ cm^{-3}$)	Experimental density ($g\ cm^{-3}$)	Porosity (%)
Base Al alloy	2.70	2.55	5.5
C1U	2.72	2.68	1.5
C2U	2.73	2.67	2.2
C3U	2.75	2.67	2.9
C*1U	2.73	2.70	1.1
C*2U	2.75	2.69	2.1
C*3U	2.78	2.71	2.5

4.1.1.2 Mechanical properties:

4.1.1.2.1 Hardness:

The Brinell hardness of the base Al alloy, Al_3Ti and Al_3Zr reinforced composite is shown in Figure 4.12. It is evident from the figure that the developed composites have higher hardness as compared to the base Al alloy. It is well established fact that the reinforcement of hard particles into the ductile matrix increase its hardness [234]. Al_3Ti and Al_3Zr particle, as a hard reinforcement, provide inherent property of hardness to the matrix material which enhance its ability to resist deformation [235]. With increasing number of reinforced particles, hardness of the composites is also increased. It is also observed that the hardness is increased due to refinement of the matrix phase because, during deformation, movement of dislocations are effectively resisted by the increased grain boundaries. As shown in Figure 4.7, developed composites have smaller grain size than that of the base Al alloy. The hardness of the composites also improves when dislocations are generated around the particles due to difference in CTEs between reinforced particles and Al matrix [235]. The composites have clean interface between the Al matrix and in-situ formed particles which provide better bonding between them and as a result the capacity of the composite to bear load is increased. Therefore, improvement in the hardness of the composites is observed. The hardness of Al_3Zr reinforced composites is higher than the Al_3Ti reinforced composite

which may be attributed to the smaller size of Al_3Zr particles, than that of Al_3Ti particles which effectively resist the movement of dislocations.

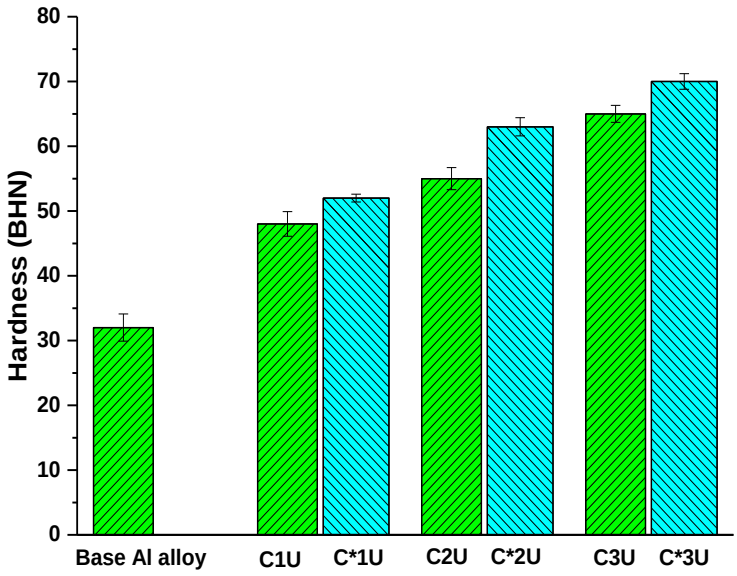

Figure 4. 12 Variation in hardness of base Al alloy and the developed composites

4.1.1.2.2 Tensile properties:

Engineering stress-strain curves of the Al_3Ti and Al_3Zr reinforced composites are shown in Figure 4.13 and 4.14, respectively. Values of their tensile properties are listed in Table 4.2. In comparison with the base Al alloy, higher values of YS and UTS are observed in the composites. Generally, tensile properties of composite depend on the properties of reinforced particles and matrix, and compatibility between them. During deformation, dislocations, which are generated in the matrix, interacts with the reinforced particles present in the matrix and the movement of dislocations is resisted. Additional stress is required to move these dislocations which results in increased UTS and YS of the composites [236]. The grain refinement of the matrix, uniform distribution of the particles in the matrix, clean interface between reinforced particles and Al matrix resisting the initiation of crack at the interface due to efficient transfer of load from the matrix to the particle, and presence of dislocations around the particles are other factors which contribute in the improvement of tensile strength of the composites [237–239].

It is also observed from the figure that there is a significant improvement in the ductility (% elongation) of the composites as compared to the base alloy. This improvement can be attributed to the ability of the particles to resist the propagation of crack during deformation. Therefore, ductility of the composite can be improved by providing resistance in the direction of crack propagation [199]. Small grains of the matrix, which do not facilitate crack propagation, good interfacial bonding between the particles and Al matrix, and presence of less porosity, due to ultrasonication, which act as a weak point in the composites, are other factors which contribute in the improvement of ductility of the composites [226,238].

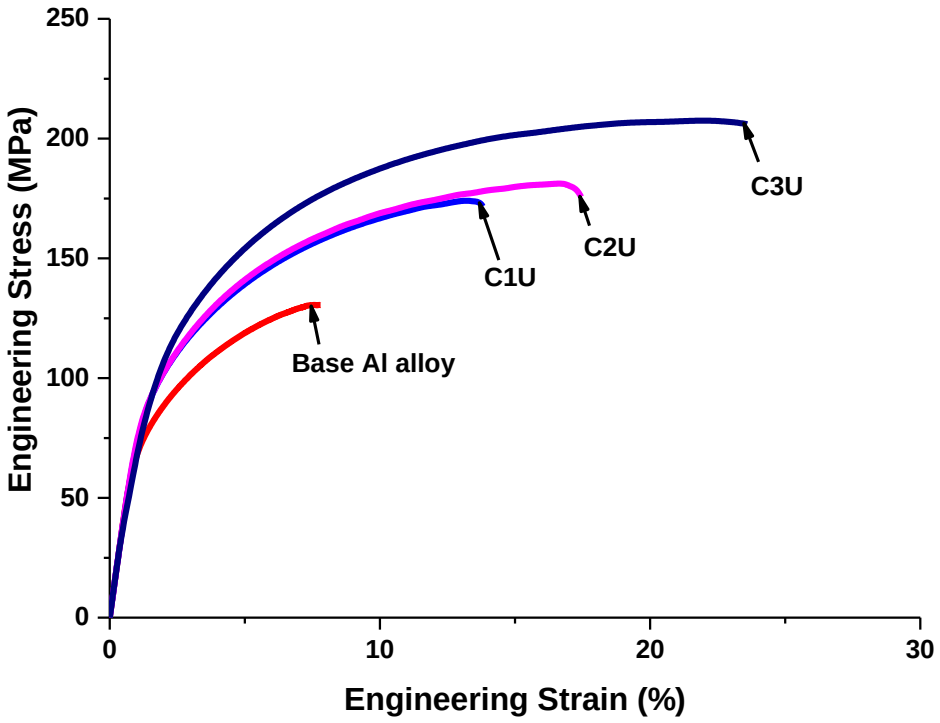

Figure 4. 13 A comparison of the tensile stress versus strain curves for the base Al alloy and Al_3Ti reinforced Al composites

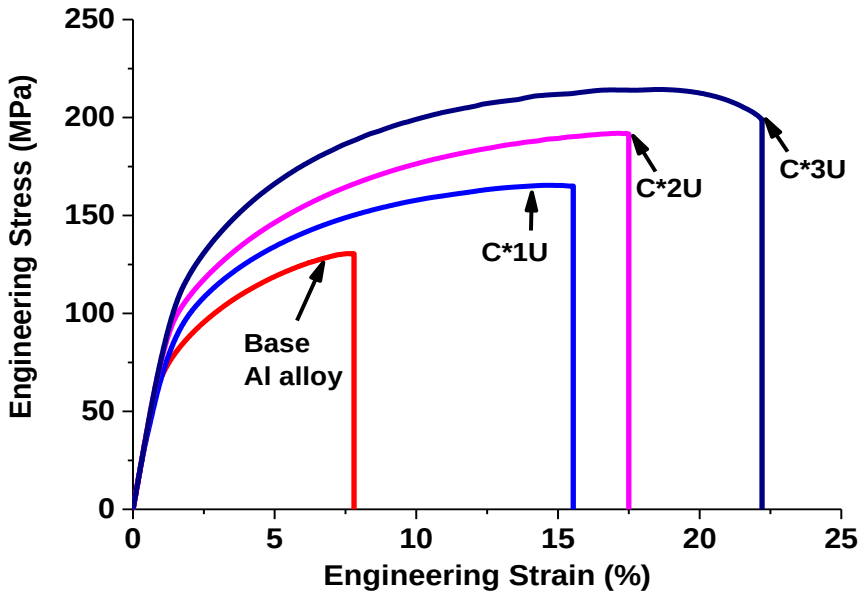

Figure 4. 14 A comparison of the tensile stress versus strain curves for the base Al alloy and Al_3Zr reinforced Al alloy composites

Table 4. 2 Variation in UTS, YS and elongation of as cast and composites

Casting condition	UTS (MPa)	YS (MPa)	Elongation (%)
Base Al alloy	130 ± 5	59 ± 3	7.7 ± 2.1
C1U	175 ± 4	66 ± 2	13.8 ± 3.1
C2U	188 ± 3	74 ± 2	16.5 ± 1.5
C3U	208 ± 3	84 ± 2	23.5 ± 2.6
C*1U	166 ± 5	72 ± 2	15.6 ± 3.4
C*2U	192 ± 2	81 ± 3	17.5 ± 3.0
C*3U	214 ± 5	91 ± 2	22.2 ± 3.0

To study the effects of reinforcement particles on the strength of the composites, two approaches are considered which are based on continuum mechanics and micromechanics strengthening, respectively. In continuum mechanics, the load transfer to reinforcement particle is due to good bonding between the matrix and the particles. Whereas in micromechanics, the strengthening effect of the particles is the basis for improved strength. In the continuum mechanics approach, the yield strength of composites (σ_{yc}) can be expressed as [240,241]

$$\sigma_{yc} = \sigma_{ym}\left[V_p\left(\frac{2+S}{2}\right) + (1 - V_p)\right] \quad 4.9$$

where σ_{ym} is the yield stress of the matrix phase, *Vp* is the particle volume fraction in the composites and *S* (l/w) is the aspect ratio of the reinforcing particles.

In the micromechanics approach, the yield strength of the metallic matrix (σ_{ym}) is calculated by considering the grain refinement strengthening ($\Delta\sigma_{HP}$), Orowan strengthening ($\Delta\sigma_{Or}$) and strengthening due to thermal mismatch($\Delta\sigma_{CTE}$), and can be expressed as [241]

$$\sigma_{ym} = \sigma_o + \Delta\sigma_{HP} + \sqrt{(\Delta\sigma_{Or})^2 + \Delta\sigma_{CTE}{}^2} \quad 4.10$$

where σ_o is the yield strength of the as cast sample (base alloy).

In the strengthening due to grain refinement, grain boundaries resist the motion of dislocation due to the high lattice disorder of the grain boundary region and misorientation of adjacent grains [50]. By refining the grains of aluminium alloy, grain boundary area can be increased which further increase the resistance to the motion of dislocation improving the yield strength of the matrix. This improvement in yield strength due to grain refinement can be calculated by using Hall-Petch relationship [241,242]

$$\Delta\sigma_{HP} = k\left(d^{-\frac{1}{2}} - d_o^{-\frac{1}{2}}\right) \quad 4.11$$

where *k* is the Hall-Petch slope, *d* (μm) is the average grain size of the composites and d_o (μm) is the average grain size of as-cast alloy. By putting the values of *d*, d_o and *k* in eqn. 8, the increment in the yield stress due to grain refinement for different composites is calculated and shown in Table 4.4.

The yield strength of the matrix is increased when particulate reinforced composites are quenched from the working temperature (750 ^oC) to room temperature. According to the Taylor strengthening mechanism, volumetric strain occurs in the composite due to significant differences in CTE between the matrix and the reinforced particles. To accommodate the CTE difference, geometrically necessary dislocations (GND) are produced around the particles which increases the flow stress in the matrix [232]. Hence,

the yield strength of the matrix is improved due to CTE mismatch strengthening (σ_{CTE}) which can be described as [242]

$$\Delta\sigma_{CTE} = \beta G b\sqrt{\rho} \quad 4.12$$

where β is a constant; G and b are the shear modulus of the matrix and the Burgers vector, respectively; ρ is the dislocation density induced by the CTE mismatch, which can be estimated as [226]

$$\rho = \frac{12\,\Delta\alpha\,\Delta T\,Vp}{b\,D\,(1-Vp)} \quad 4.13$$

where Δα is the CTE mismatch between the matrix and the reinforcing particles; ΔT (K) is the difference between solidification start temperature and test temperature; V_p is the volume fraction of the particles and D (μm) is the diameter of the particles. By using eqn. 4.12 and 4.13, the increment in the yield strength due to difference in CTE is calculated and shown in Table 4.4.

In Orowan strengthening, precipitate particles hinder the movement of dislocations. With the application of stress, the dislocation on interaction with the precipitates are first bowed, then reconnected, and finally the dislocation loops are formed around the particles. These dislocation loops hinder the movement of subsequently formed dislocations and thereby improve the strength of the composite [232].

However, the Orowan-strengthening is initiated when the reinforcement particles are smaller than 1μm [232,243]. In this work, the average size of the particles in all the composites are greater than 1 μm. Hence, Orowan mechanism is not expected to contribute to strengthening. So, eqn. 4.10 can be modified as:

$$\sigma_{ym} = \sigma_o + \Delta\sigma_{HP} + \Delta\sigma_{CTE} \quad 4.14$$

Table 4. 3 Useful parameters for calculating the strengthening mechanism in Al-Al_3Ti and Al-Al_3Zr composites

Parameter	Description	Value	Reference/Comment
V_p	Volume fraction of particles	0.022, 0.043 and 0.065	Calculated for C1U, C2U and C3U composites, respectively
		0.019, 0.038 and 0.056	Calculated for C*1U, C*2U and C*3U composites, respectively
S	Aspect ratio	1.8, 2.8 and 2.7	Calculated for C1U, C2U and C3U composites, respectively
		1.7, 2.1 and 2.8	Calculated for C*1U, C*2U and C*3U composites, respectively
k	Hall-Petch slope	74×10^{-3} MPa$\sqrt{m}$	[226]
d_o	Average grain size of base Al alloy	213 µm	Calculated
d	Average grain size of the composites	104, 76 and 57 µm	Calculated for C1U, C2U and C3U composites, respectively
		120, 93 and 79 µm	Calculated for C*1U, C*2U and C*3U composites, respectively
β	Constant	1.25	[243]
G	Shear modulus	26 GPa	[226]
b	Burgers vector	0.286 nm	[226]
α_{Al}	CTE of Al	25.2×10^{-6} K^{-1}	[226]
α_p	CTE of Al_3Zr	15.5×10^{-6} K^{-1}	[221]
α_p	CTE of Al_3Ti	13.0×10^{-6} K^{-1}	[227]
σ_o	Yield strength of the base Al alloy	59 MPa	Calculated
$T_{process}$	Processing temp.	940 K	Solidification start temp. of Al
T_{test}	Testing temp.	298 K	Room Temperature
D	Average particle size	3.3, 2.9, and 3.8	Calculated for C1U, C2U and C3U composites, respectively
		1.2, 1.6 and 1.9 µm	Calculated for C*1U, C*2U and C*3U composites, respectively

Using the above equations and values taken from the literature (Table 4.3), comparison between experimentally obtained YS and theoretically calculated YS of the composites is done as shown in Table 4.4. The experimental values of yield strengths of C1U, C2U and C3U composites are 1.2, 1.2 and 1.1 times smaller than their respective predicted values whereas, for C*1U, C*2U and C*3U composites, it is 1.1, 1.1 and 1.0 times smaller than their respective predicted values. This difference between the predicted and experimental values may be attributed to the less uniformity in particle distribution in the matrix and measurement error of average grain size, average particle size and aspect ratio of the particle. Improvement in yield strength due to thermal mismatch is more as compared to

that due to grain refinement which suggests that thermal mismatch strengthening is the dominant strengthening mechanism in the developed composites.

Table 4. 4 Predicted, experimental and contribution of different strengthening mechanisms to the yield strength of composites: σ_{ym}, YS of matrix; $\sigma_{yc,p}$, Predicted YS; $\sigma_{yc,e}$, Experimental YS.

Casting condition	$\Delta\sigma_{Hall\text{-}Petch}$ (MPa)	$\Delta\sigma_{CTE}$ (MPa)	σ_{ym} (MPa)	$\sigma_{yc,p}$ (MPa)	$\sigma_{yc,e}$ (MPa)	Absolute error (%)
C1U	2.2	14.0	75.2	76.7	66	16.2
C2U	3.4	21.0	83.4	88.4	74	19.4
C3U	4.7	23.0	86.7	94.5	84	12.5
C*1U	1.7	19.1	79.8	81.1	72.0	12.6
C*2U	2.6	23.6	85.2	88.6	81.0	9.4
C*3U	3.3	26.6	88.9	95.8	91.0	5.3

4.1.1.2.3 Fractography:

The fracture surface analysis is very helpful to identify the contribution made by different mechanism to failure process and to identify the dominant failure mechanism. Therefore, to identify the failure mechanisms operating in the composite, fractographical examination of the fractured surface of the tensile specimen is conducted which has been successfully used on monolithic metals to identify their failure mechanisms. Fractured surface of the base alloy, C1U, C2U and C3U are shown in Figure 4.15 (a-d) and fractured surface of C*1U, C*2U and C*3U are shown in Figure 4.16 (a-c). Base alloy is fractured in a brittle manner as tear ridges and cleavage facets are observed as shown in Figure 4.15 (a). The base alloy has high porosity, low density, as shown in Table 4.1, and coarse grains, as shown in Figure 4.7. Therefore, the base alloy has shown low UTS, YS and poor toughness as shown in Table 4.2. Few dimples and plastic slip bands are observed in C1U composite as shown in Figure 4.15 (b) which indicates the improvement in ductility of the composite over base alloy. It is observed from the Figure 4.15 (c) and (d) that the number of dimples is increased, and the size of dimples is reduced which may be attributed to the improvement in

ductility and refinement of matrix as the amount of reinforcement is increased. The fractured surface of the composites indicates mixed mode fracture dominated by ductile fracture.

The developed composites are failed due to mixed mode fracture dominated by ductile fracture as shown in Figure 4.16 (a-c). In Figure 4.16 (a), plastic slip bands, few dimples and tear ridges are observed which suggests that some plastic deformation occurred in the C*1U composite as compared to the base alloy. The population of tiny dimples are relatively increased in C*2U composite as shown in Figure 4.16 (b) which shows that composite went through more plastic deformation before failure took place. However, step wise facets, formed due to shear fracture, are observed in some regions of the fractured surface of C*2U composite which indicates towards brittle fracture. The amount of the observed tiny dimples is further increased in C*3U composite as shown in Figure 4.16 (c) which indicates improvement in ductility over C*2U composite. It is evident from the Figure that the fracture surface of C*3U composite has uniform distribution of tiny dimples and tear ridges. On increasing the amount of reinforcement, refinement of the Al matrix is occurred which leads to the reduction in dimple size as shown in Figure 4.16 (a-c).

4.1.2 Summary:

Varying amounts of K_2TiF_6 and K_2ZrF_6 powders was reacted with molten Al at 750 ^oC to form in-situ Al_3Ti and Al_3Zr particles, respectively. Uniform dispersion of intermetallics was achieved by applying ultrasonic vibration to the melt for 5 minutes. Blocky morphology of in-situ formed Al_3Ti and Al_3Zr particles was observed with the average size of 3.4 ± 1.2 µm and 1.8 ± 0.8 µm, respectively. UTS, YS and hardness of the developed composites was improved as compared to that of the base Al alloy. During solidification, heterogeneous nucleation was promoted by the particles which acted as a nucleation site for Al matrix and led to the grain refinement of the composites. The best combination of mechanical properties with good UTS, YS and % elongation is obtained in C3U composite with 8.1 wt. % Al_3Ti was and C*3U composite with 9.1 wt. % Al_3Zr. The

well bonded and clear interface between the Al matrix and the in-situ formed particles played important role in the improvement of mechanical properties. It is concluded from the analysis of the strengthening mechanism that the dominant strengthening mechanism in the composites was thermal mismatch strengthening followed by Hall-Petch strengthening. Due to the coarseness of the particles, Orowan strengthening was omitted. It was observed that the mechanical properties of the in-situ Al_3Zr reinforced composite was better than the in-situ Al_3Ti reinforced composite. This was explained as due to the average size of Al_3Zr particles was 1.8 ± 0.8 μm which was around 50% smaller than the in-situ Al_3Ti particles whose average size was 3.4 ± 1.2 μm.

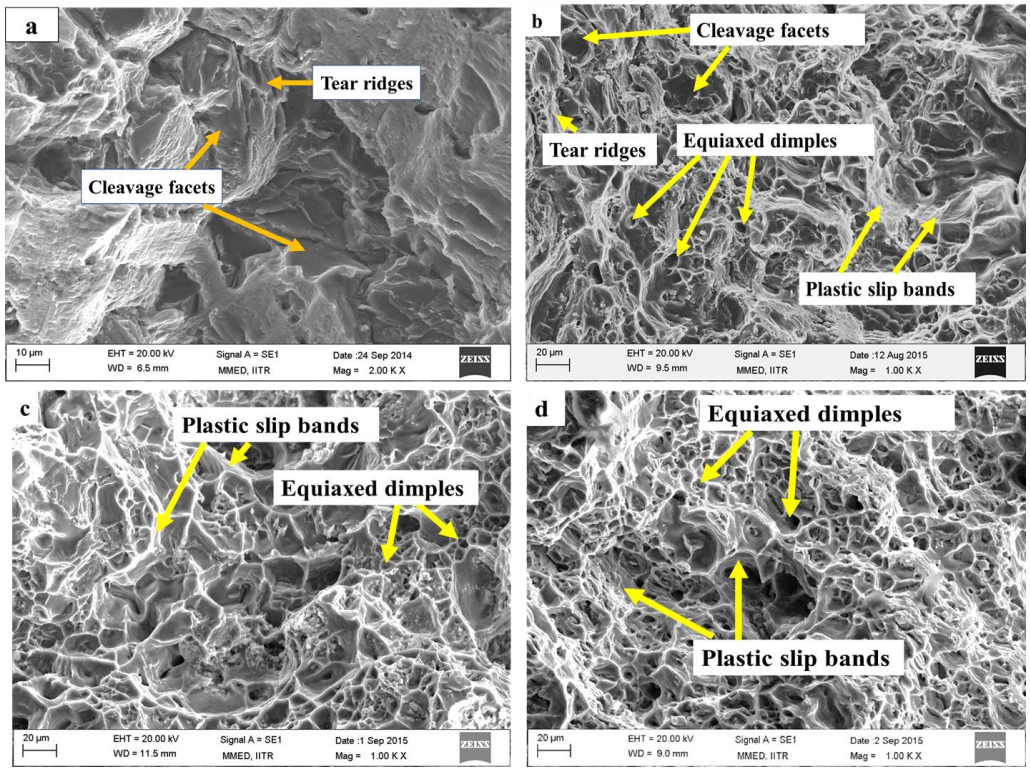

Figure 4. 15 SEM micrograph of the fracture surface of tensile specimens (a) base Al alloy; (b) C1U; (c) C2U and (d) C3U.

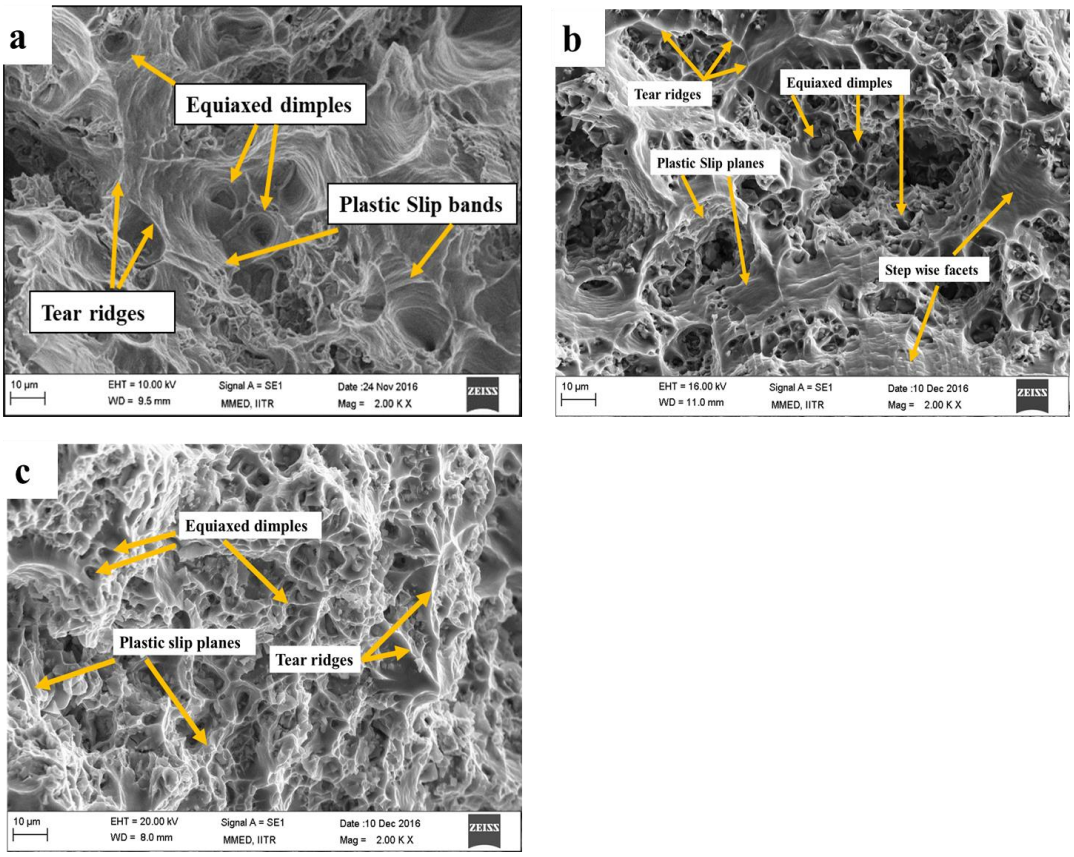

Figure 4. 16 SEM images of the tensile fractured surface of (a) C*1U; (b) C*2U and (c) C*3U

4.2 Impression creep behaviour of Al-Al_3Ti and Al-Al_3Zr composites:

Particulate reinforced aluminium matrix composites are used in the aerospace and automobile industry due to their excellent properties, such as high temperature creep ability, low density, high strength, good thermal stability, etc. [244,245]. At room temperature, aluminium alloys show high strength but their mechanical properties drop to less than 50% at temperatures higher than 473 K, limiting their use at high temperature [246].

Conventional creep test is time consuming and inconvenient because it requires many samples and it is difficult to interpret the mechanisms due to microstructural modification during the test. Therefore, a localized creep in a limited duration as achieved in indentation testing is a better alternative. In indentation creep test, spherical, pyramidal or a conical indenter is used which do not show a steady state at constant load. However, at constant load, cylindrical indenter with a flat end not only reduce the difficulty to find out

the strain rate for a spherical or pyramidal indenter but also provide constant strain rate under constant stress lending to steady state penetrating velocity. Such a creep test is called impression creep [158]. The term "impression creep" was first introduced by Chu and Li [27].

Impression creep has several advantages over conventional creep tests like (i) very small volume of material is required, (ii) relatively short duration of test, (iii) large amount of data can be obtained from a sample which not only reduce sample preparation time but also variation in properties due to involvement of many samples, (iv) due to its non-destructive nature, brittle material can also be tested. Due to these advantages, impression creep test has gained significant attention amongst the researchers in recent decades [247,248]. Apart from the advantages, limitations of this test are (i) due to its non-destructive nature, it is difficult to estimate rupture life of the sample, (ii) due to short duration of time, it is difficult to evaluate changes in creep behaviour of an engineering alloy due to changes in microstructure [248].

Creep behaviour of various aluminium alloys reinforced with different types of reinforcements such as TiC [246], B_4C [249], SiC [250–253], Al_2O_3 [254] have been studied. Among these, silicon carbide (SiC) as the short fibres, particles or whiskers are mostly used as reinforcement in the Al alloys matrix. Many research works on the impression creep properties of the magnesium [255,256] and aluminium alloys matrix composites [257,258] are being carried out, but impression creep study of aluminide reinforced Al composites has not been reported so far. Therefore, the present study aims to investigate the creep properties of in-situ aluminide reinforced Al composite.

4.2.1 Post creep test microstructure:

To study the microstructural changes during creep, the tested samples were sectioned along the impression direction and the microstructure beneath the indentation was examined. Microstructure of a sectioned sample of C3U composite which was creep tested at 573 K

and 141 MPa is shown in Figure 4.17 (a). In the figure, three different zones are observed which is differentiated by curved lines and labelled with different numbers. The line pattern is supposed to be associated with material flow during impression creep. These different deformation features can be attributed to the localised strain and stress field during impression creep [259,260]. The first zone, which is just beneath the indenter, has no microstructural changes due to hydrostatic stress distribution which is also reported by many researchers [153,261,262]. The second zone between the arc lines, where severe deformation occurred composed a semi-spherical zone. The particles are aligned along the flow direction which is indicated by arrows in Figure 4.17 (b). In this process, it is believed that under the applied stress an elastic-plastic zone is pushed into the material. Therefore, the velocity of this zone which proceeds into the material underneath the indenter governs the impression velocity. The diameter of the flow circle is comparable to the diameter of the indenter. The flow lines are more concentrated near the edges of the indenter than in front of the indenter which shows that the most severe plastic deformation takes place at the edges of the indenter. And, in the third zone, which is far away from the indenter is characterized by the particles being randomly distributed indicative of a lack of flow pattern. Also, there is an absence of plastic deformation of the material.

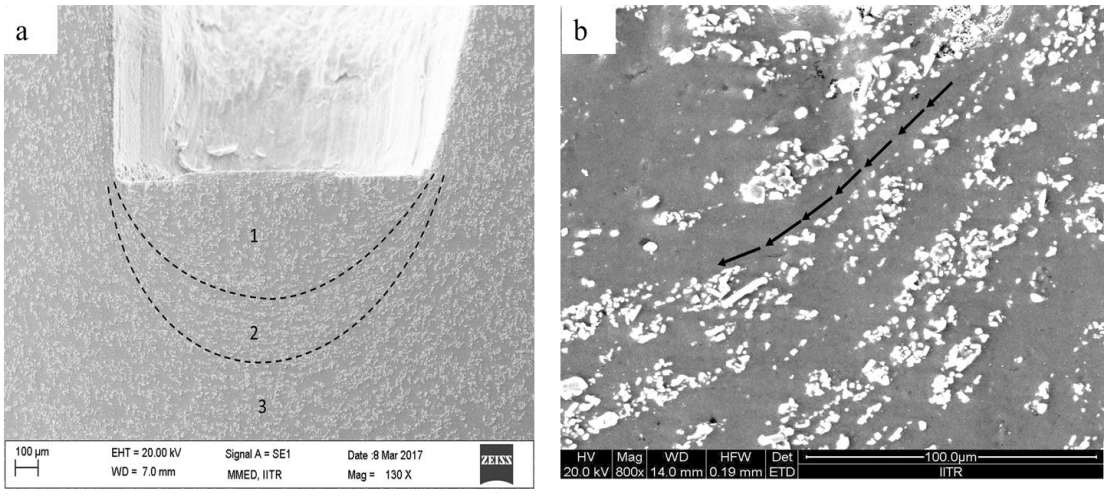

Figure 4. 17 SEM micrograph of the C3U composite after the creep test at 573 K under 141 MPa stress for 10,000 s; (a) beneath the indenter and (b) deformed region.

4.2.2 Impression creep:

The impression creep curves obtained after 10,000 s tests are shown in Figures. 4.18, 4.19, 4.20, 4.21, 4.22, 4.23 and 4.24 for the base Al alloy, C1U, C2U, C3U, C*1U, C*2U and C*3U composites, respectively. It is observed from the curve that primary (Stage 1) creep followed by secondary (Stage 2) creep are observed. The tertiary stage is not observed because rigid (elastic) materials offer restriction by enveloping plastic zone which result in stable deformation under the punch. Therefore, steady state stage is maintained for long period of time and this is a unique advantage of the impression creep test over the conventional tensile creep test.

In the primary stage, creep rate decreases with time as work hardening is dominant in this stage, whereas, in the secondary stage, creep rate is constant because equilibrium is established between the work hardening and recovery. Similar impression creep curves for the other alloys were reported in the published literature by Mohammadi and co-workers [263] and Kutty and co-workers [264]. It is observed from impression creep curves that on increasing temperature and stress, creep rate is also increased. The primary stage in creep curves of base Al alloy, C1U, C2U, C3U, C*1U, C*2U and C*3U at temperature 603 K is small as compared to other temperatures as work hardening effect is low at high temperature.

The minimum impression rate, $\dot{\varepsilon}$, during the steady state is determined by

$$\dot{\varepsilon} = \frac{\partial h}{\partial t} \qquad 4.15$$

where ‘h’ (mm) is the depth of indentation and ‘t’ (s) is time

Power law relation is used for dominant creep mechanism which is as follows [262,263]:

$$\dot{\varepsilon} = \frac{A\, D_v G b}{kT} \left(\frac{\sigma}{G}\right)^n \qquad 4.16$$

where D_v is the diffusion coefficient, $\dot{\varepsilon}$ is the minimum creep rate, b is the Burger vector, T is the temperature in Kelvin, A is the constant, k is the Boltzmann constant, G is the shear modulus and ‘n’ is the stress exponent. The equation of D_v is given by [26]

$$D_v = D_o \exp\left(-\frac{Q}{RT}\right) \qquad 4.17$$

where 'Q' is the activation energy, 'R' is the gas constant and 'T' is the temperature in Kelvin. By combining Eqs. (4.16) and (4.17) we get

$$\dot{\varepsilon} = A(\frac{GbD_o}{kT})(\sigma/G)^n \exp(-\frac{Q}{RT}) \quad 4.18$$

For stress exponent 'n', Norton's equation is used [255]

$$\dot{\varepsilon} = A'\sigma^n \exp(-\frac{Q}{RT}) \quad 4.19$$

which can be rewritten by taking logarithm on either side as

$$\ln \dot{\varepsilon} = \ln A' + n \ln \sigma - \frac{Q}{RT} \quad 4.20$$

According to this model, at constant temperature, a plot between ln $\dot{\varepsilon}$ and ln σ gives straight line having a slope equal to the stress exponent 'n'. The values of 'n' at different temperatures for base Al alloy, C1U, C2U and C3U composites, and for C*1U, C*2U and C*3U composites are different as shown in Figure 4.25 and 4.26, respectively and summarised in Table 4.5. These stress exponent values are helpful to identify the dominant creep mechanism in the material. Several operative creep mechanisms have been reported in the literature [264,265]. If the stress exponent 'n' is unity, the dominant creep mechanism is based on diffusional flow such as Nabarro-Herring creep and Coble creep. If 'n' is found to be 2, the creep controlling mechanism is grain boundary sliding. When n = 3, it is a form of creep where the dislocations glide velocity is controlled by solute drag. When 'n' value is in the range of 4-7, the dominant mechanism is climb of edge dislocation. The value of n > 7 can be observed by blocking the dislocation motion, lattice self-diffusion and grain boundary sliding which can be achieved by developing an intermediate phase within the matrix [266].

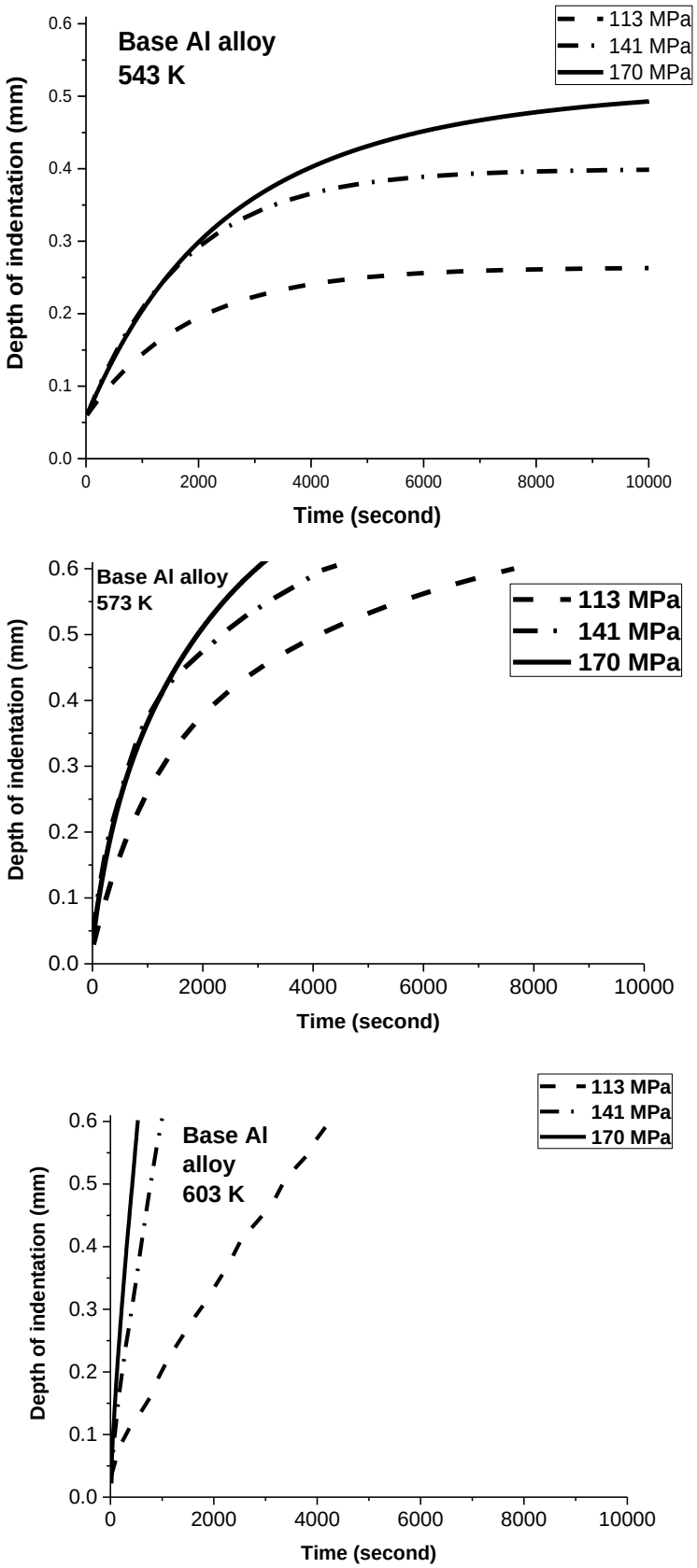

Figure 4. 18 Impression creep test of base Al alloy at 543 K, 573 K and 603 K temperature and stresses at 113 MPa, 141 MPa and 170 MPa

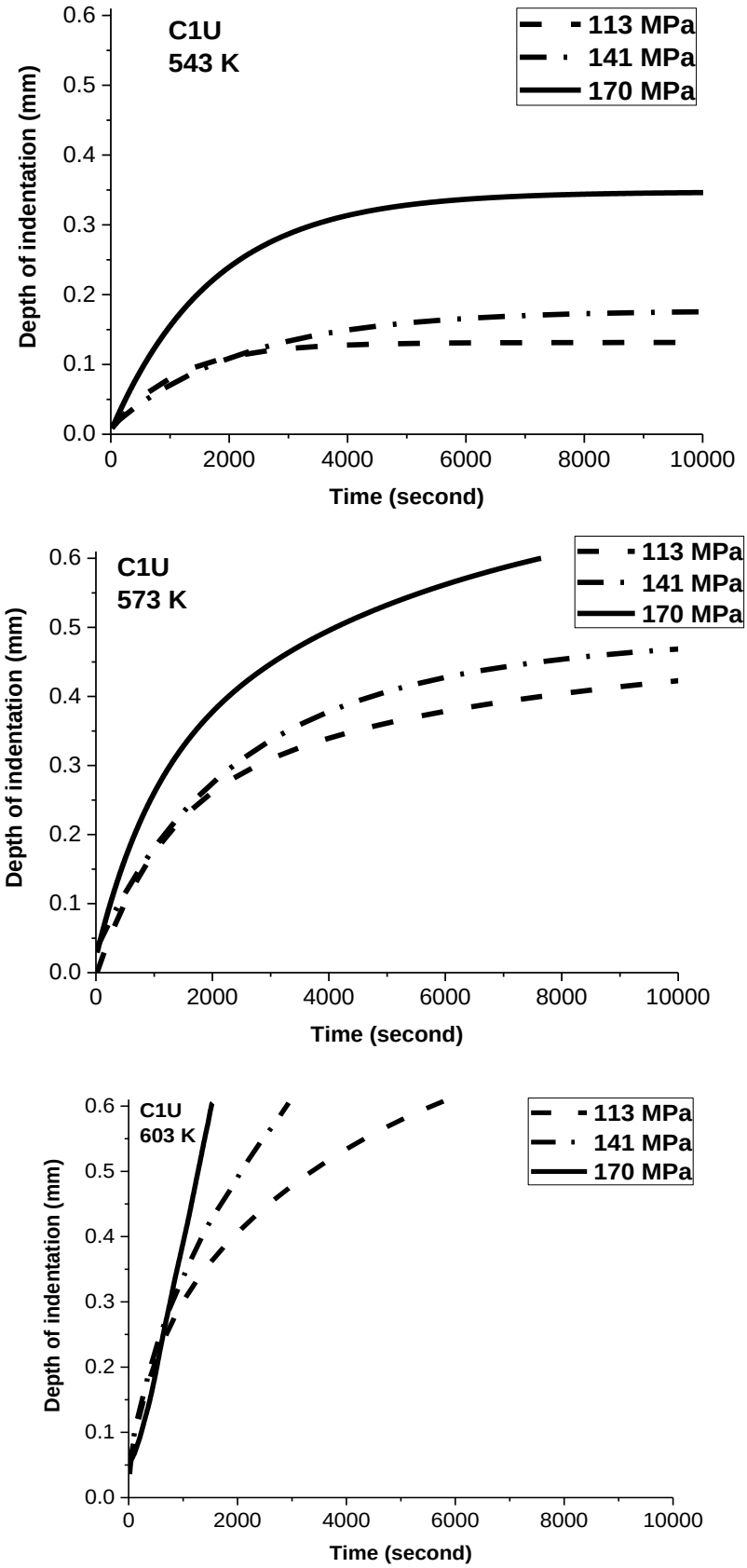

Figure 4. 19 Impression creep test of C1U at 543 K, 573 K and 603 K temperature and stresses at 113 MPa, 141 MPa and 170 MPa

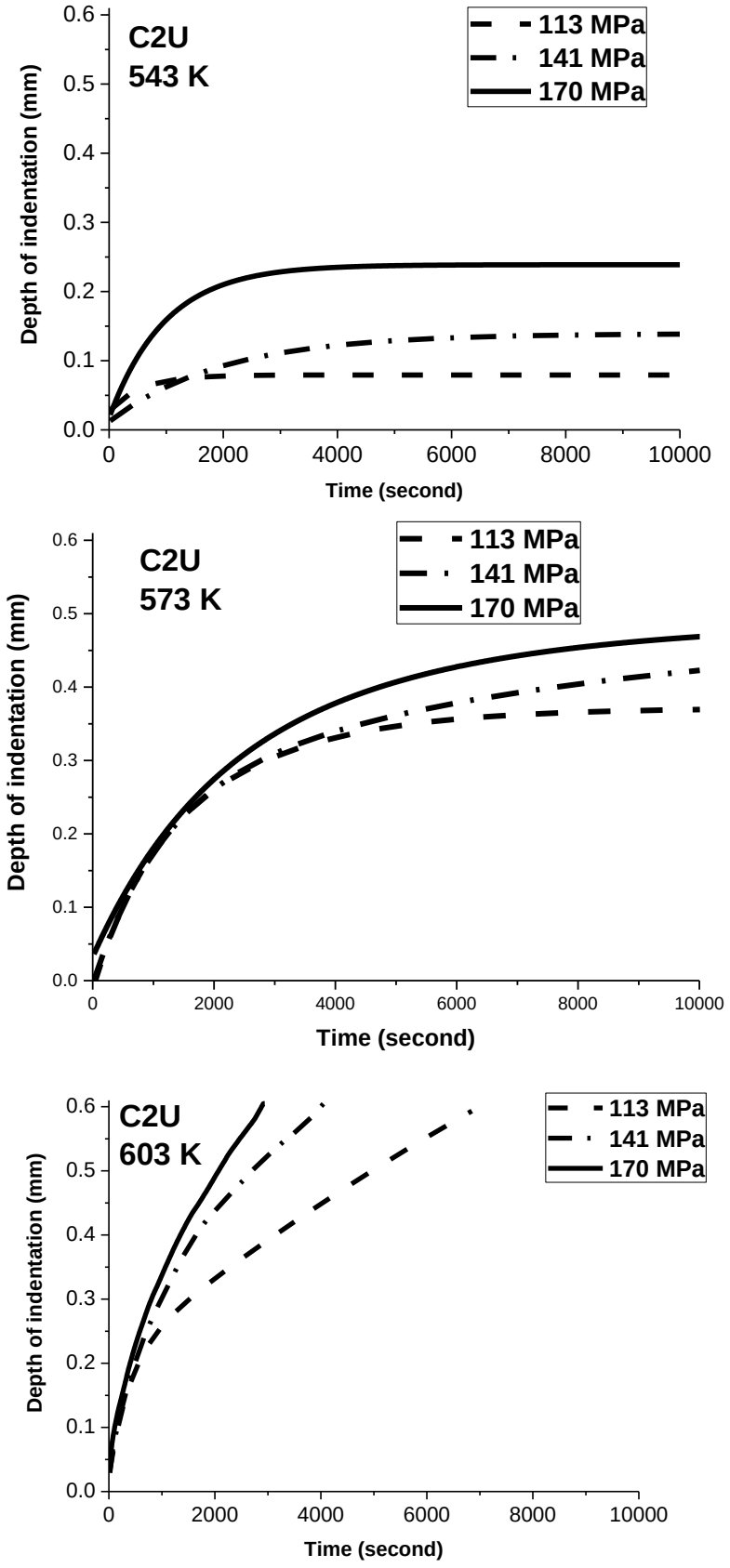

Figure 4. 20 Impression creep test of C2U at 543 K, 573 K and 603 K temperature and stresses at 113 MPa, 141 MPa and 170 MPa

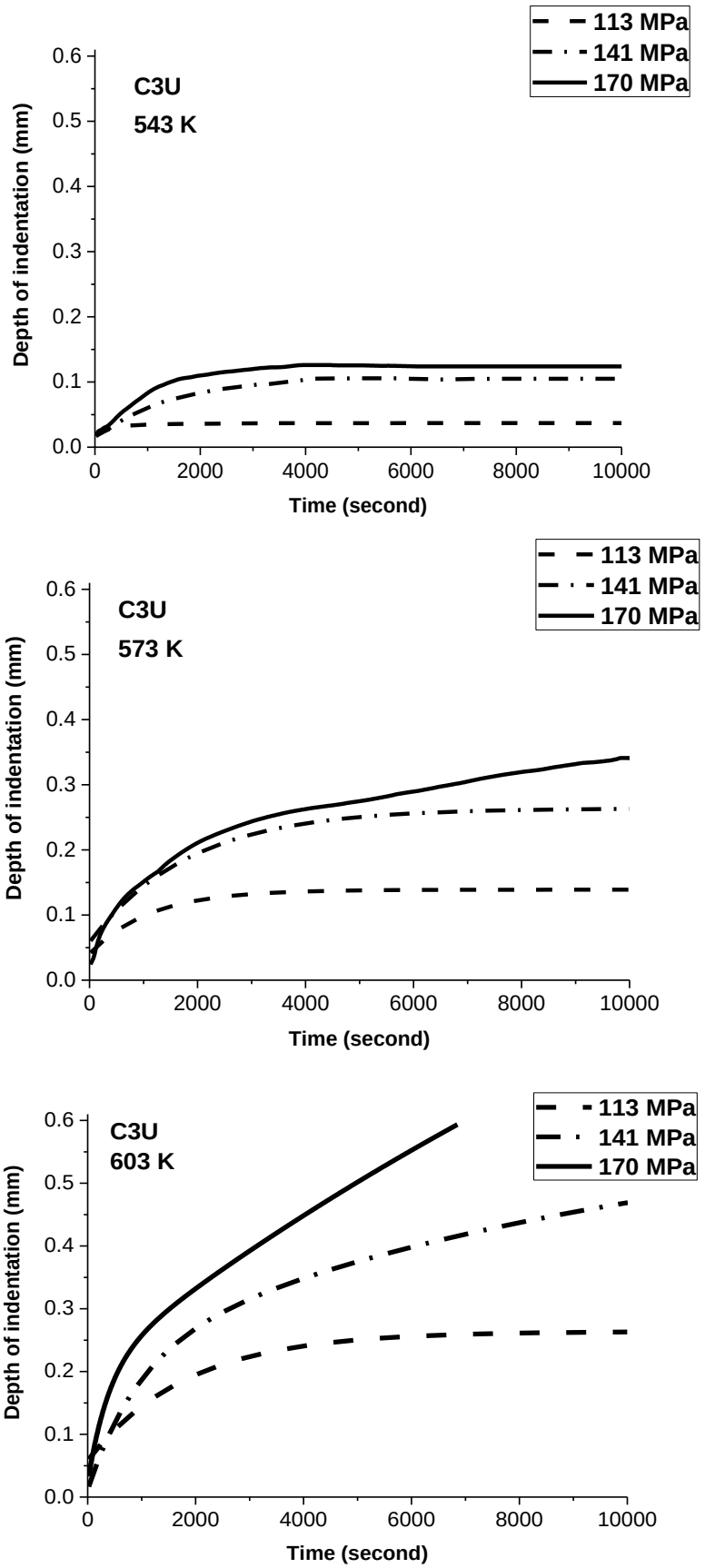

Figure 4. 21 Impression creep test of C3U at 543 K, 573 K and 603 K temperature and stresses at 113 MPa, 141 MPa and 170 MPa

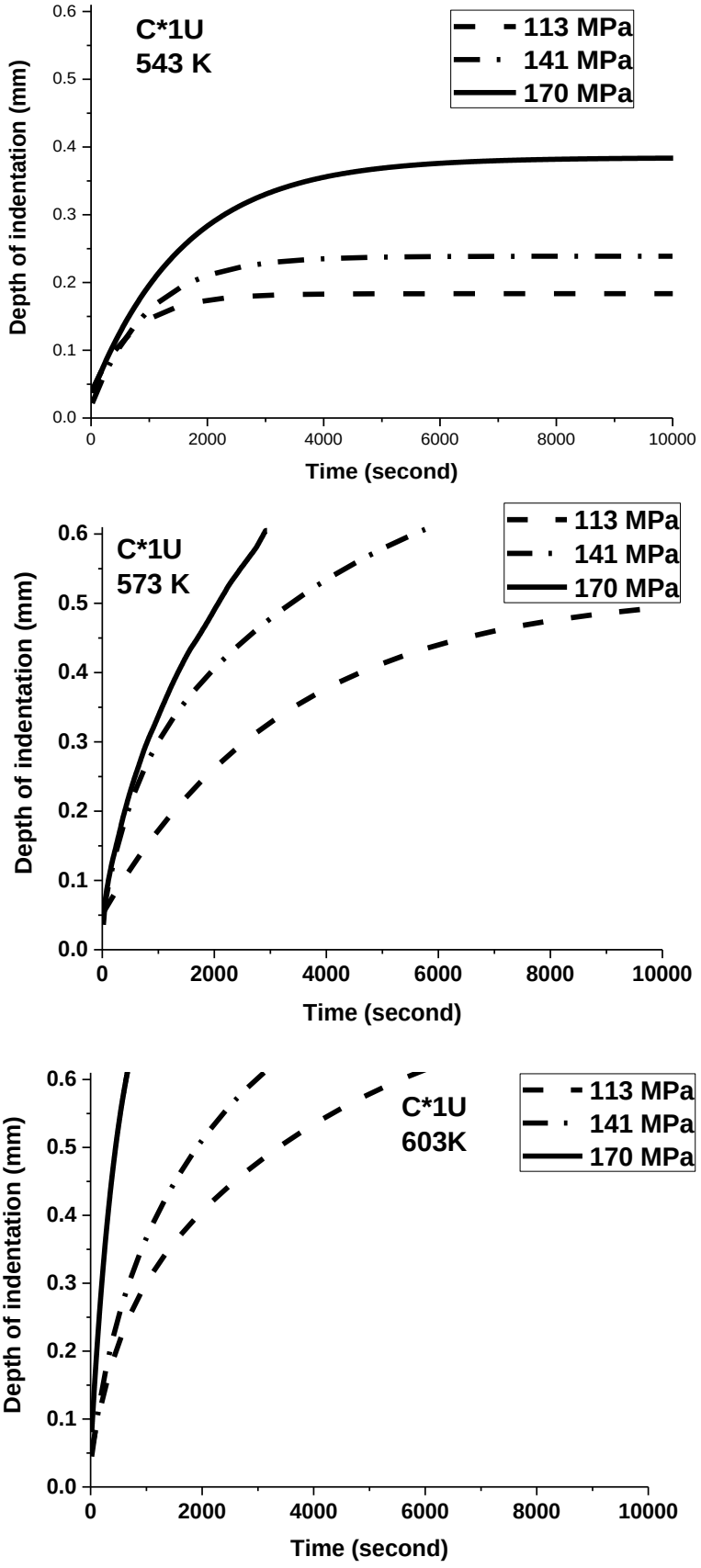

Figure 4. 22 Impression creep curves of C*1U tested at 543 K, 573 K and 603 K temperature and stresses at 113 MPa, 141 MPa and 170 MPa

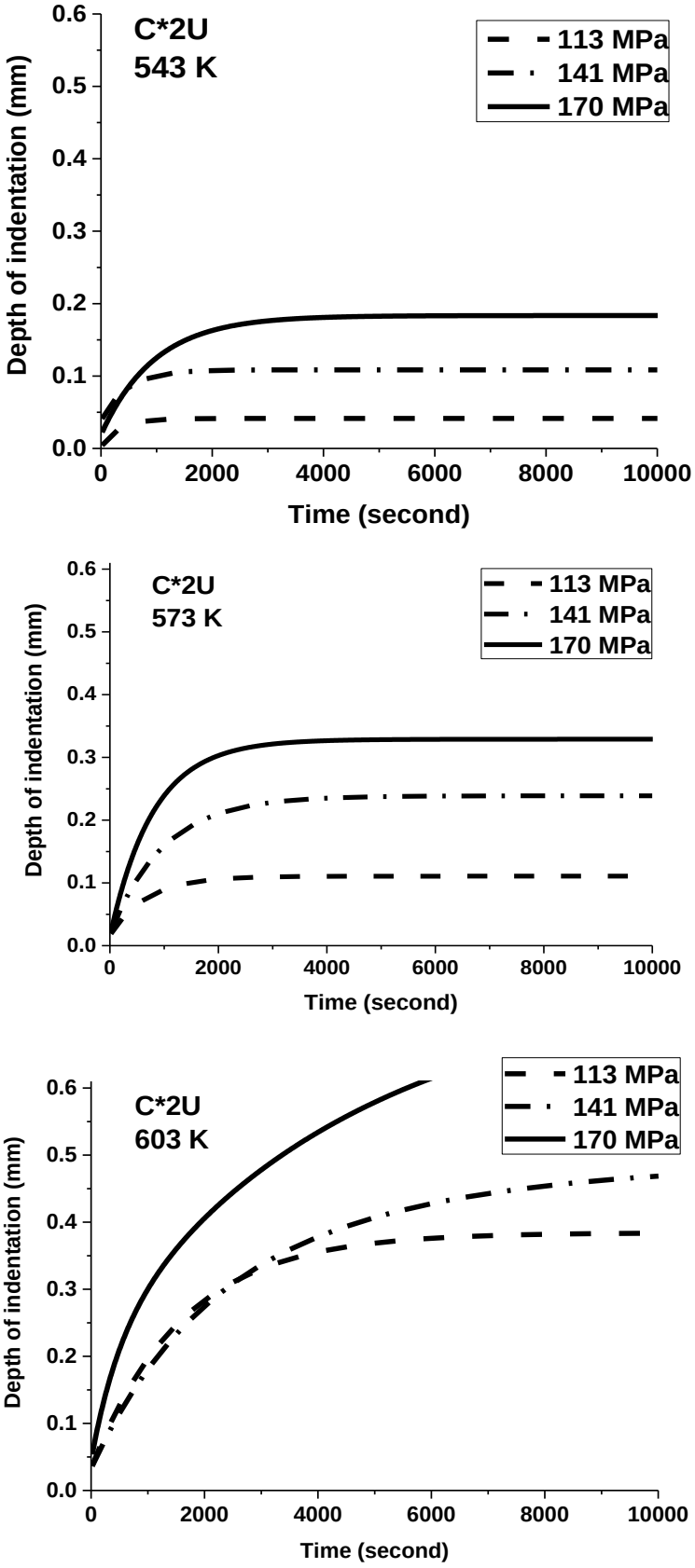

Figure 4. 23 Impression creep curves of C*2U tested at 543 K, 573 K and 603 K temperature and stresses at 113 MPa, 141 MPa and 170 MPa.

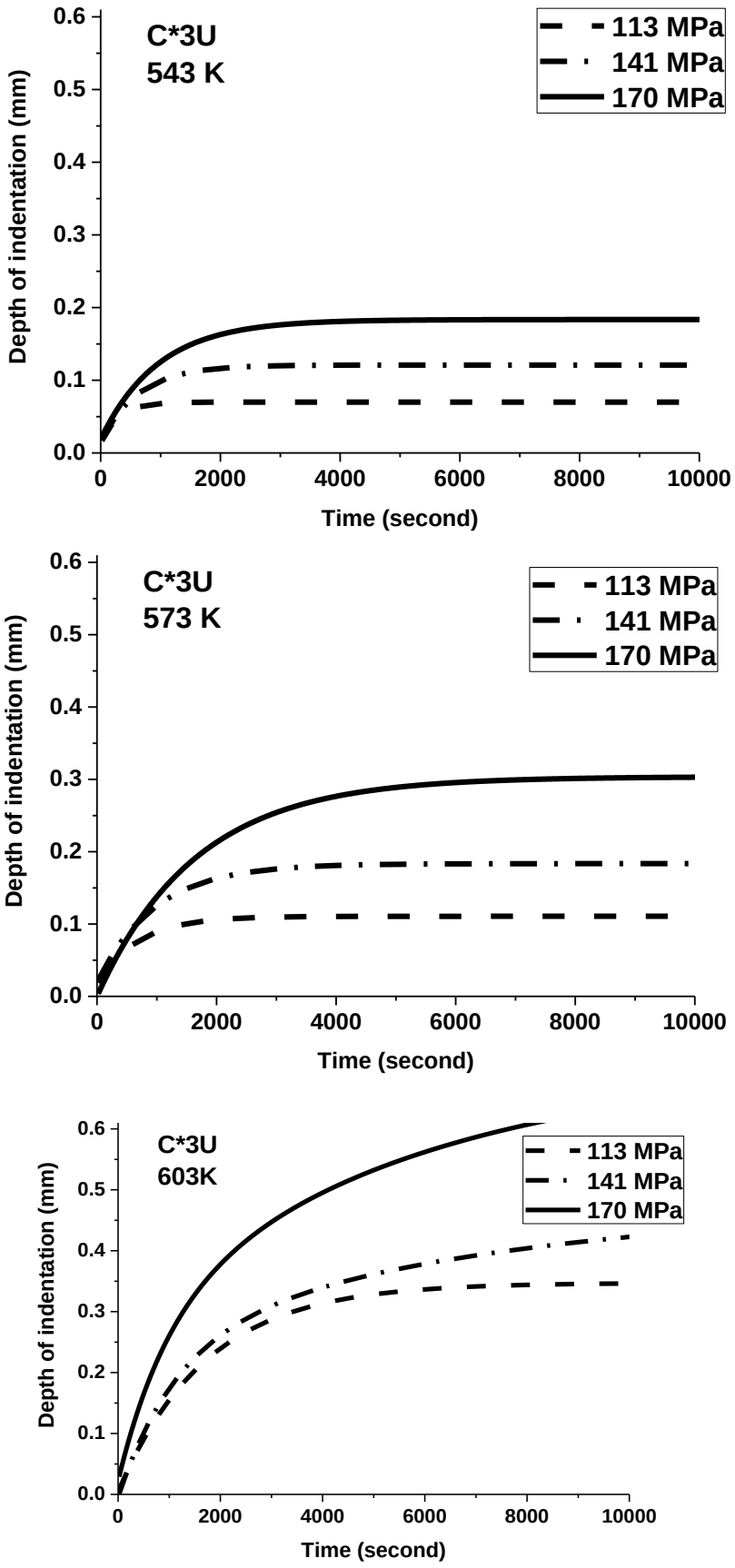

Figure 4. 24 Impression creep curves of C*3U tested at 543 K, 573 K and 603 K temperature and stresses at 113 MPa, 141 MPa and 170 MPa.

The average value of '*n*' for base Al alloy, C1U, C2U, C3U, C*1U, C*2U and C*3U are 3.6 ± 0.2, 4.2 ± 0.2, 5.2 ± 0.2, 5.8 ± 0.3, 4.8 ± 0.2, 5.4 ± 0.2 and 6.7 ± 0.3, respectively which indicates that the dominant creep mechanism in all the composites is the dislocation climb. As demonstrated, the stress exponent significantly decreased from 3.9 to 3.2, 4.6 to 4.2, 5.5 to 4.8, 6.4 to 5.4, 5.2 to 4.5, 5.7 to 5.1 and 7.2 to 6.3 for base Al alloy, C1U, C2U, C3U, C*1U, C*2U and C*3U, respectively with increasing temperature from 543 to 603 K. The drop of '*n*' values with temperature reflects the instability of the microstructure at high deformation temperatures. The observed instability may be attributed to the softening of Al alloy matrix at high temperature.

This mechanism is independent of grain size (q = 0) [267,268] which is concluded from the ln $\dot{\varepsilon}$ vs. ln d plot as shown in Figure 4.27 and 4.28. It is observed from the plot that the creep rate decreases as grain size of the composites decrease which means that the grain size of the composites does not adversely affect the creep rate. Also, the increase in creep resistance due to the reinforced particles cancel out the adverse effect which arise due to grain refinement, if any.

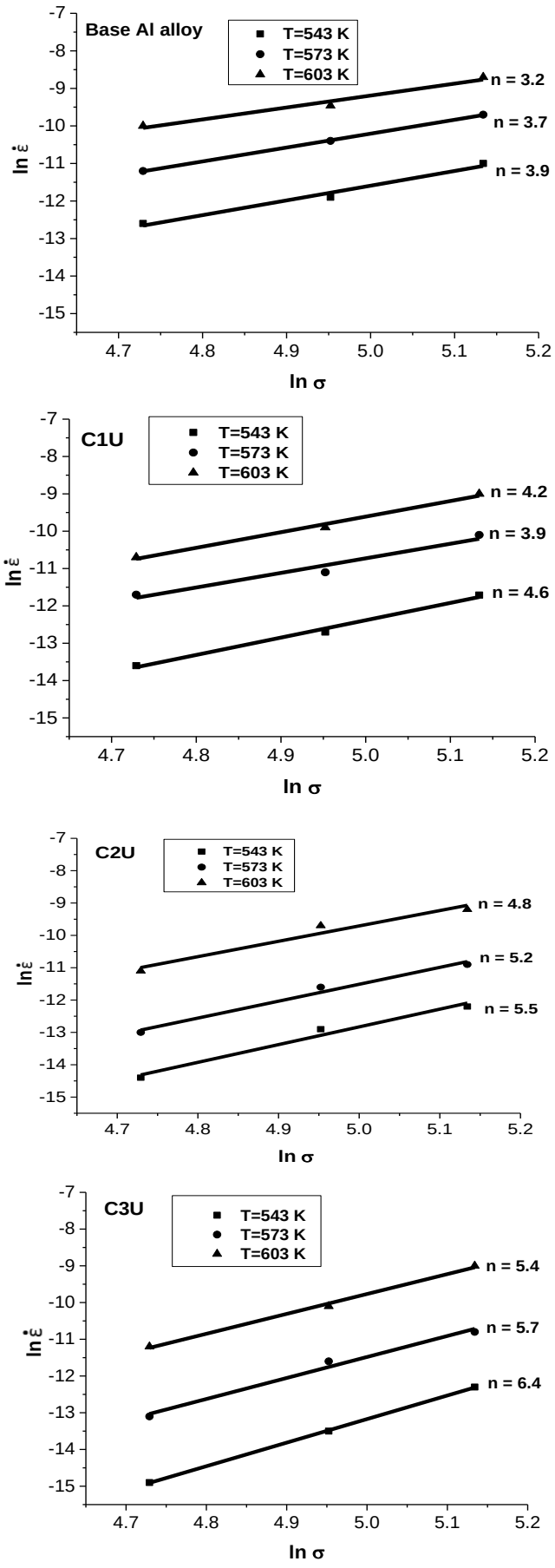

Figure 4. 25 Plot of ln $\dot{\varepsilon}$ vs. ln σ for calculating the stress exponent for base Al alloy, C1U, C2U and C3U

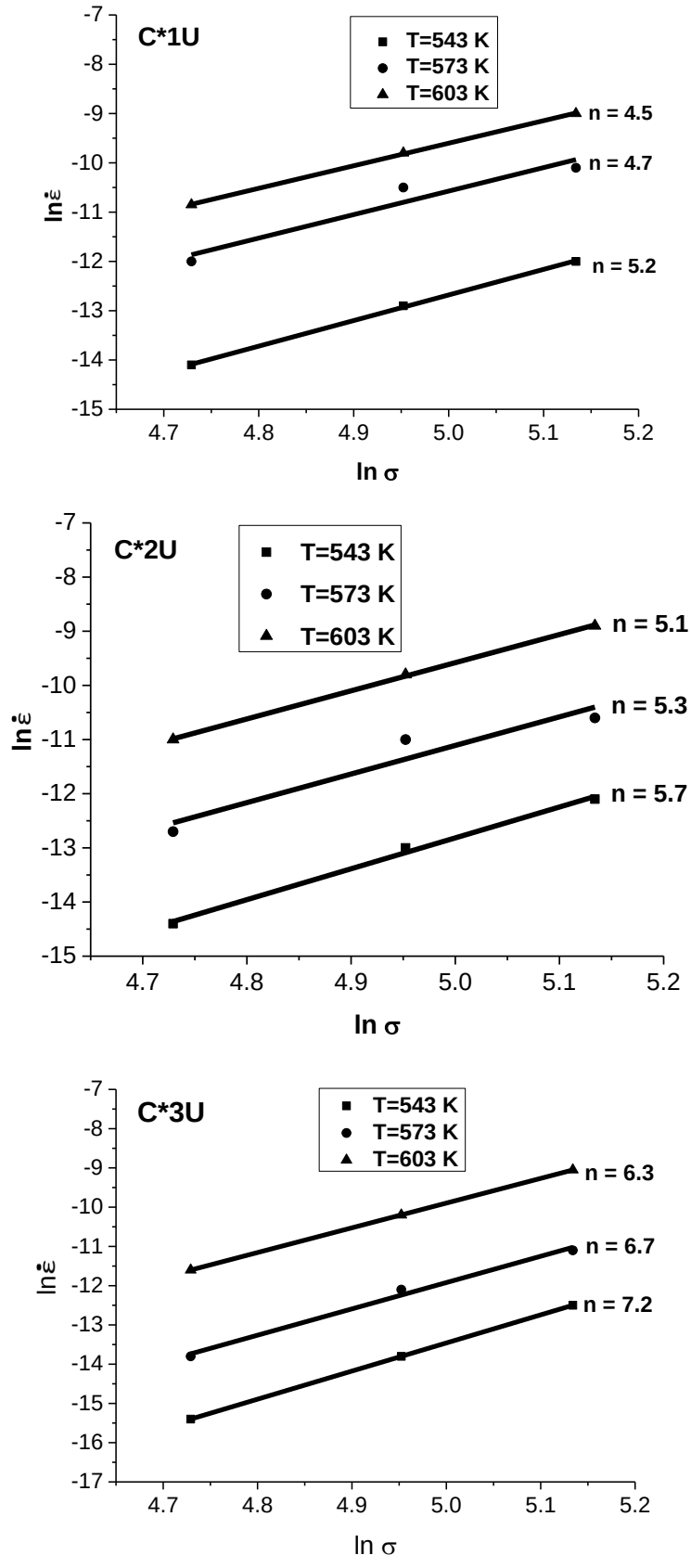

Figure 4. 26 Plot of ln **ε̇** vs. ln σ for calculating the stress exponent for C*1U, C*2U and C*3U

Table 4. 5 Stress exponent 'n' values for different composites

Composite	Creep test temperature, K	Stress exponent, *n*
Base Al alloy	543	3.9
	573	3.7
	603	3.2
C1U	543	4.6
	573	3.9
	603	4.2
C2U	543	5.5
	573	5.2
	603	4.8
C3U	543	6.4
	573	5.7
	603	5.4
C*1U	543	5.2
	573	4.7
	603	4.5
C*2U	543	5.7
	573	5.3
	603	5.1
C*3U	543	7.2
	573	6.7
	603	6.3

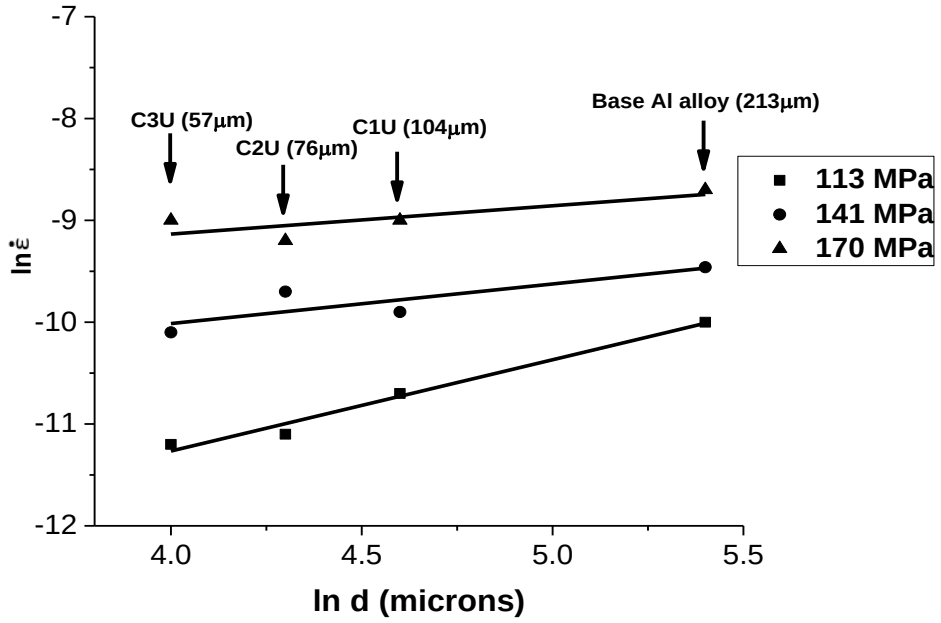

Figure 4. 27 Plot of ln $\dot{\varepsilon}$ vs. ln d for calculating grain size exponent 'q' for all the three samples at 603 K temperature

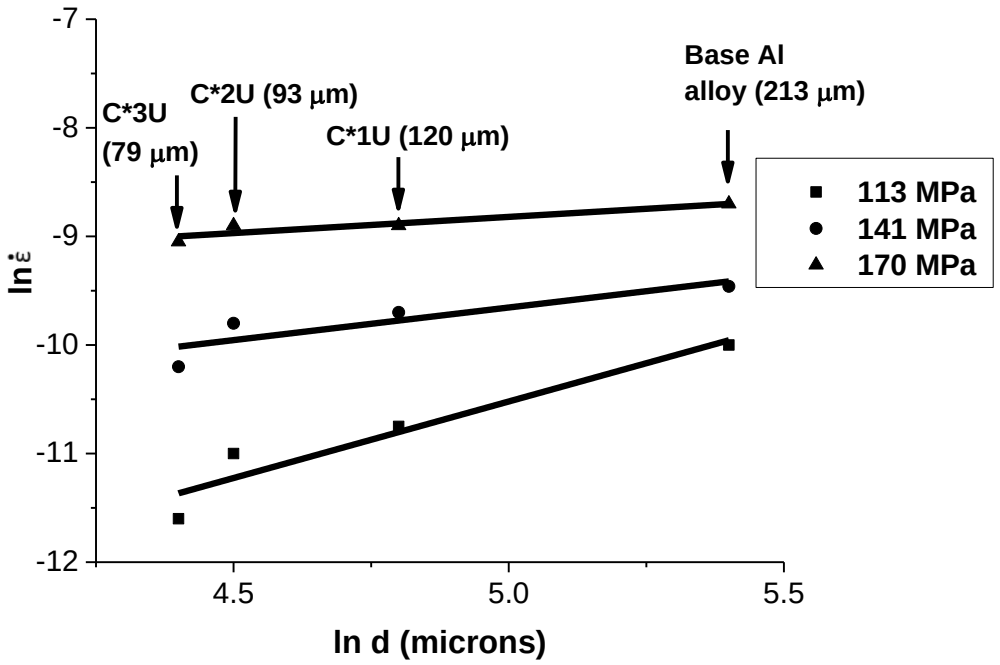

Figure 4. 28 Plot of ln $\dot{\varepsilon}$ vs. ln d for calculating grain size exponent 'q' for all the three samples at 603 K temperature

In the deformation process, thermal activation is mainly responsible for creep and without thermal fluctuation creep cannot occur in the material. The activation energies for creep provide better understanding of the mechanism contributing to creep in the material. These mechanisms can be identified by their respective activation energy [269]. So, this activation energy is calculated using Arrhenius type rate equation [135]:

$$\dot{\varepsilon} = Ae^{-Q/RT} \qquad 4.21$$

For a constant stress, the plot between ln $\dot{\varepsilon}$ vs. 1/T is a straight line which has a slope equal to *Q/R* where *R* is the gas constant (8.3 J/mol) and *Q* is the activation energy. The obtained values of Q are 111 ± 4 kJ/mol, 127 ± 3 kJ/mol, 143 ± 4 kJ/mol and 157 ± 5 kJ/mol for base Al alloy, C1U, C2U and C3U, respectively as shown in Figure 4.29, and 142 ± 3 kJ/mol, 148 ± 3 kJ/mol and 163 ± 4 kJ/mol for C*1U, C*2U and C*3U, respectively as shown in Figure 4.30. The standard deviation of the mean is reported as the error values. The activation energy of base Al alloy, Al_3Ti reinforced composites and Al_3Zr reinforced composites are close to lattice self-diffusion (142 kJ/mol) [270]. It indicates that the velocity of dislocation climb is controlled by diffusion of Al atoms through lattice. It is observed

from the Figure 4.29 and 4.30 that the values of activation energy are decreased as stress is increased. This can be attributed to the formation of higher density of dislocation under an application of higher stresses. As a result, more rate of materials flow by diffusion through dislocation pipe than that through the lattice which lowers the activation energy [271,272]. Therefore, on the basis of stress exponent and activation energy values, it can be concluded that lattice diffusion-controlled dislocation climb is the dominant creep mechanism in the base Al alloy and the developed composites.

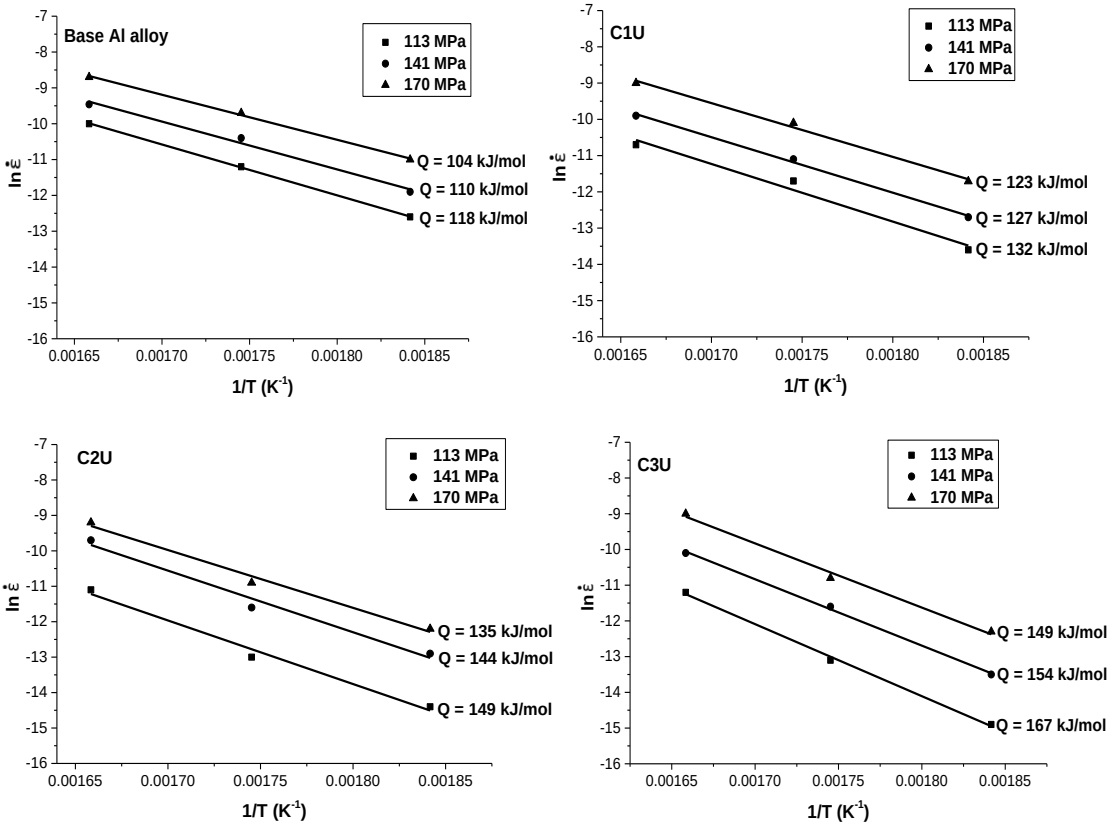

Figure 4. 29 Plot of ln $\dot{\varepsilon}$ vs. 1/T for calculating the activation energy for base Al alloy, C1U, C2U and C3U.

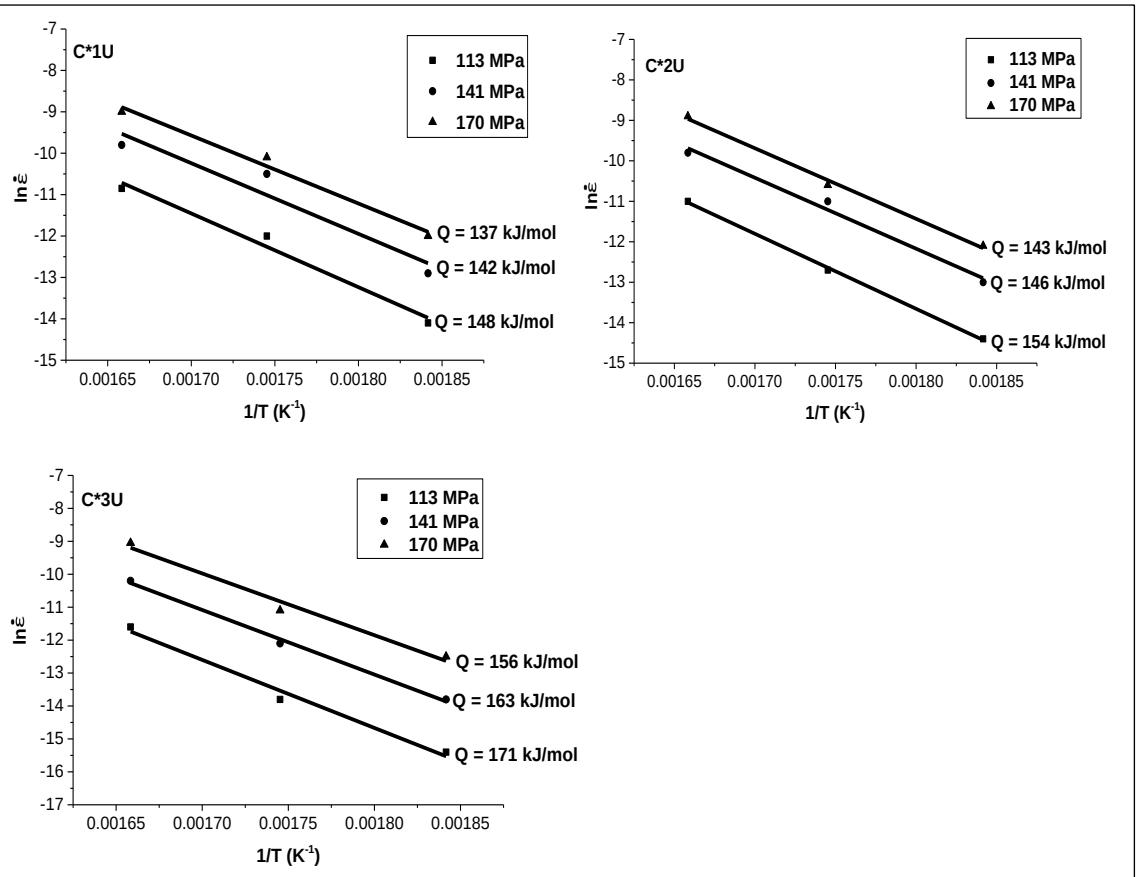

Figure 4. 30 Plot of ln $\dot{\varepsilon}$ vs. 1/T for calculating the activation energy for C*1U, C*2U and C*3U.

Minimum impression rate or steady state impression rate comparison between Al_3Ti and Al_3Zr reinforced composites at different temperature and stresses is shown in Figure 4.31. From these figures, it is observed that steady state impression rate of base Al alloy is higher than that of composites at all the test temperatures. This is because dislocation creep or power law creep is governed by the movement of dislocations assisted by dislocation climb aided by diffusion of vacancy [135]. This movement of dislocation is dependent on activation energy. The value of activation energies of the composites is larger than that of base Al alloy as shown in Figure 4.29 and 4.30. For large activation energy, diffusion of vacancy is low which resist the movement of dislocation and thus, the creep rate is low. The C*3U composite has the lowest impression rate among all the composites because it has the largest activation energy. It is also observed from the figure that the steady state impression rate is higher at higher temperature than that at lower temperature for a given stress. At higher temperatures, the ability of dislocations to climb over particles is apparently fast

enough to render the particles as ineffective dislocation barriers. At lower temperatures, the time needed for a dislocation to climb around a particle (for a given stress) is much longer, so the creep resistance is significantly improved [273].

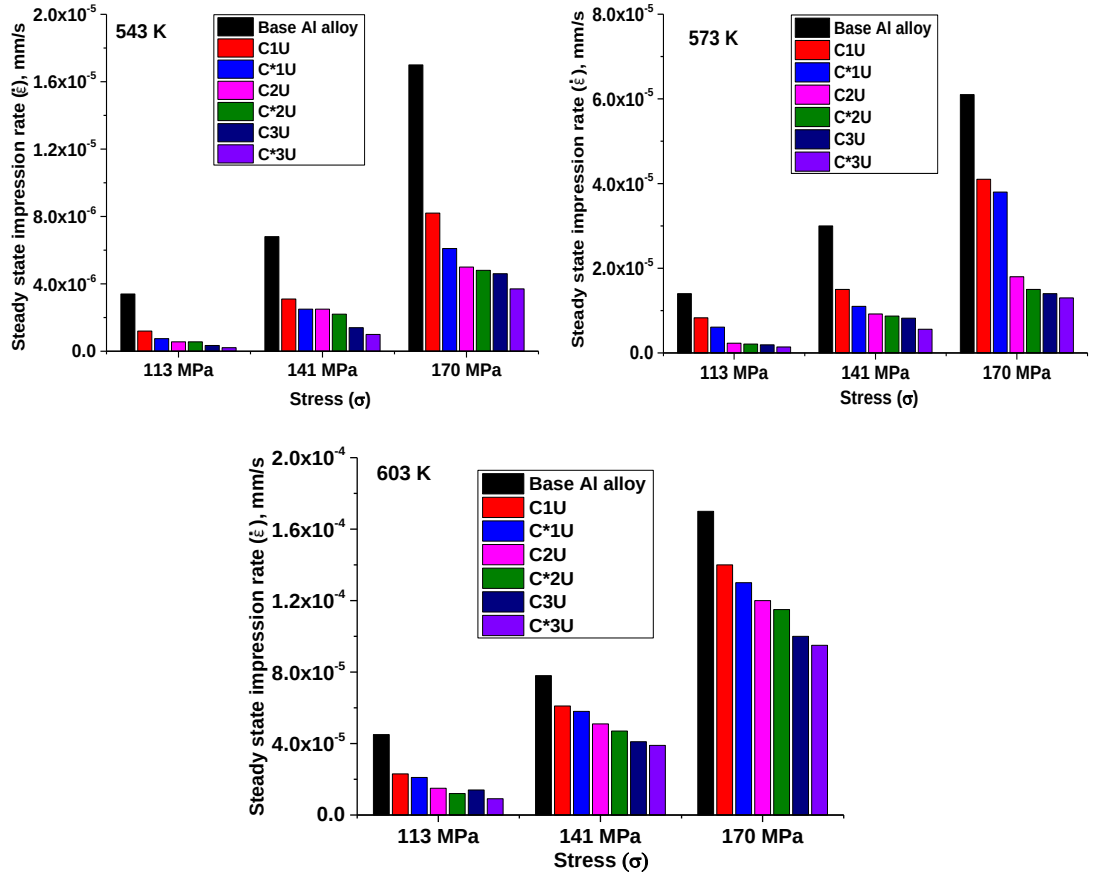

Figure 4. 31 Comparison of impression rate for base Al alloy and the composites under different stresses tested at 543 K, 573 K and 603 K.

Creep resistance of the composite also depends on coherency between matrix and reinforcement particles. A large mismatch in lattice coherency between matrix and reinforced particles give undesirable microstructure that have poor mechanical properties at elevated temperatures. A non-coherent particle having no crystal structural relationship with the aluminium atoms as illustrated in Figure 4.32 (a). When there is a lattice coherency, these dispersed particles are highly stable and provide good mechanical properties for the composite at elevated temperatures [274]. A coherent particle that has similar lattice parameters and crystal structure relationship with the surrounding aluminum matrix atoms as illustrated in Figure 4.32 (b). It has already been shown in the section 4.1.1.1 that in-situ

formed Al_3Ti and Al_3Zr particles have fairly good lattice match with α-Al and therefore, enhances creep property of the composites.

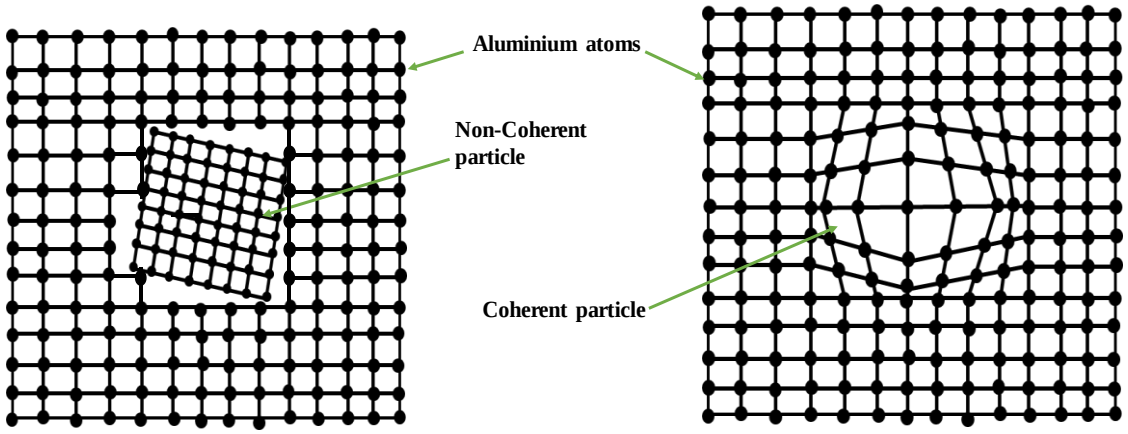

Figure 4. 32 (a) illustrates a non-coherent particle. (b) illustrates a coherent particle that has similar crystal structure relationship with the surrounding aluminium matrix atoms.

Intermetallic particles enhance creep properties by either resisting grain boundary sliding or suppressing dislocation annihilation (recovery) [272,275,276]. The high melting point of the particles confirm their stability at the creep test temperature. Therefore, it seems that the presence of the particles inside the matrix phase enhances the creep properties of the composites by preventing dislocation easy gliding during the creep deformation. Further, the presence of the particles in the matrix improve its resistance to plastic deformation which also increases creep resistance of the composite. Therefore, it can be observed from Figures. 4.18, 4.19, 4.20, 4.21, 4.22, 4.23 and 4.24 that at a particular stress and temperature the penetration depth of the indenter for any duration of time is decreased as the amount of reinforcement is increased.

4.2.3 Summary:

The creep behaviour of Al-Al_3Ti and Al-Al_3Zr composites is investigated at various temperatures ranging from 543 K to 603 K and under stresses between 113 MPa and 170 MPa. Creep resistance of the composites are higher than that of the base Al alloy suggesting that Al_3Ti and Al_3Zr particles addition is beneficial. Composite with the highest particle addition is the most creep resistant. The creep resistance is attributed to the lattice coherency

between the reinforced particles and Al matrix reflected in higher activation energy values which resist the movement of dislocation. The values of calculated stress exponent 'n' lie in the range of 3-7 for base Al alloy and the composites suggesting that the dominant creep mechanism is the dislocation creep. The activation energy value for the creep of base Al alloy and the composites are close to that of the lattice self-diffusion (142 kJ/mol) of aluminium. This implies that the dominant creep mechanism in base Al alloy and the composites is the lattice self-diffusion-controlled dislocation creep. Since creep controlling mechanism is dislocation creep mechanism which is independent of grain size, the refinement in microstructure of the composites, obtained from the incorporation of uniformly distributed in-situ particles throughout the matrix, achieved by ultrasonication of the melt, do not affect the creep behaviour of the composites. Both the composites have shown similar creep behaviour under the selected range of temperatures and stresses.

4.3 High cycle fatigue behaviour of Al-Al_3Ti and Al_3Zr composites:

In aerospace industries, commercial sectors and transport, the demand of particulate reinforced Al matrix composites (PRAMMCs) have increased due to their stiffness and high specific strength. In aerospace applications, components, in their service life, are undergone through many cyclic stresses which can degrade the materials due to fatigue. Therefore, it is very crucial from design aspect to investigate the fatigue behaviour of the components fabricated from these materials to know the life and reliability of these components [277].

There are several factors which affects the fatigue properties of PRAMMCs. These include temperature, composition, type and frequency of loading, microstructure, operating test conditions such as stress or strain controlled, aging treatment of the matrix, bonding between particle and matrix, size of reinforced particle, volume fraction of reinforcement and its distribution, etc. [278].

There are three different stages in the process of fatigue damage of the composite which is similar to the alloy. These stages are: (1) fatigue crack initiation (Stage I); crack

propagation (Stage II); ultimate fracture (Stage III). In stage I, inclusions and the reinforced particles are considered as an initiation sites for fatigue crack. Stage II can reveal the relationship between damage mechanisms and microstructure as microstructural features govern the damage process. In stage III, dimple formation and the particle fracture, similar to the tensile fracture, are the main features of the fatigue fracture [279–282].

In recent years, in-situ metal matrix composites have gained lot of attention because of their good machinability [283,284] and mechanical properties [285–290]. The good mechanical properties are required in the field of structural engineering which involve dynamic high-cyclic loading during their long-term period. Therefore, it is of great interest to investigate high-cyclic fatigue behaviour of in-situ metal matrix composites as it has been reported that the in-situ metal matrix composite shows improved HCF limit as compared to the unreinforced alloys [291–294].

Many researches have been carried out on ex-situ particle reinforced composites to study their HCF damage which was commonly fabricated by powder metallurgy route [29,295–297]. It has been observed that the damage occurred in those composites are mainly due to interface debonding and particle fracture. The morphology and the size of reinforced particles affect HCF properties of composites. The reinforced particles which have sharp edges can act as a site for crack initiation and leads to brittle fracture because these sharp edges increase stress concentration during HCF [279–282]. Also, small sized particles may substantially improve HCF of composites [29,298,299]. The in-situ composites which have small sized reinforced particles will have noticeable effect on HCF behaviour. The most Common reinforcement for Al based MMCs are oxides (SiO_2, Al_2O_3), carbides (TiC, SiC) and borides (ZrB_2, TiB_2).

High cycle fatigue study of aluminide reinforced Al composites has not been reported so far. Therefore, present study aims to investigate and compare high cycle fatigue behaviour of in-situ formed Al_3Ti and Al_3Zr reinforced composites.

4.3.1 Fatigue properties:

The S–N curves of the base Al alloy and the developed composites are shown in Figure 4.33. It is observed that fatigue life is increased as the amount of reinforcement is increased. In high cycle fatigue test, a significant part of the total fatigue life is the crack initiation [300]. Therefore, when the particles are formed in the aluminium alloys, they provide higher resistance to crack initiation. Therefore, C3U and C*3U among Al_3Ti and Al_3Zr reinforced composites, respectively exhibit longer fatigue life under any amplitude. It has been reported in the literature that high cycle fatigue life of PRMMCs is improved [301,302]. The reason behind this improvement can be attributed to the transfer of load from the matrix to the particle.

Strain amplitude has strong influence on the fatigue process which was demonstrated by Park et al. [300]. The presence of high strength and high modulus particles in the matrix lower the total strain at any stress level. Thus, fatigue life of the composites is improved as they experience lower strain as compared to the base Al alloy at the same stress level. On the other hand, it is known that crack is initiated when there is the cyclic slip in the slip bands [301]. However, the presence of small reinforced particles can delay the crack initiation by acting as a barrier to the development of slips bands which leads to decrease in slip distance [303]. Thus, resistance to crack initiation is enhanced.

It has been reported that several factors affect the HCF performance of PRMMCs such as the volume fraction and the particle size [303]. Fatigue resistance can be enhanced either by decreasing the particle size or increasing the volume fraction due to a combination of direct and indirect strengthening [36].

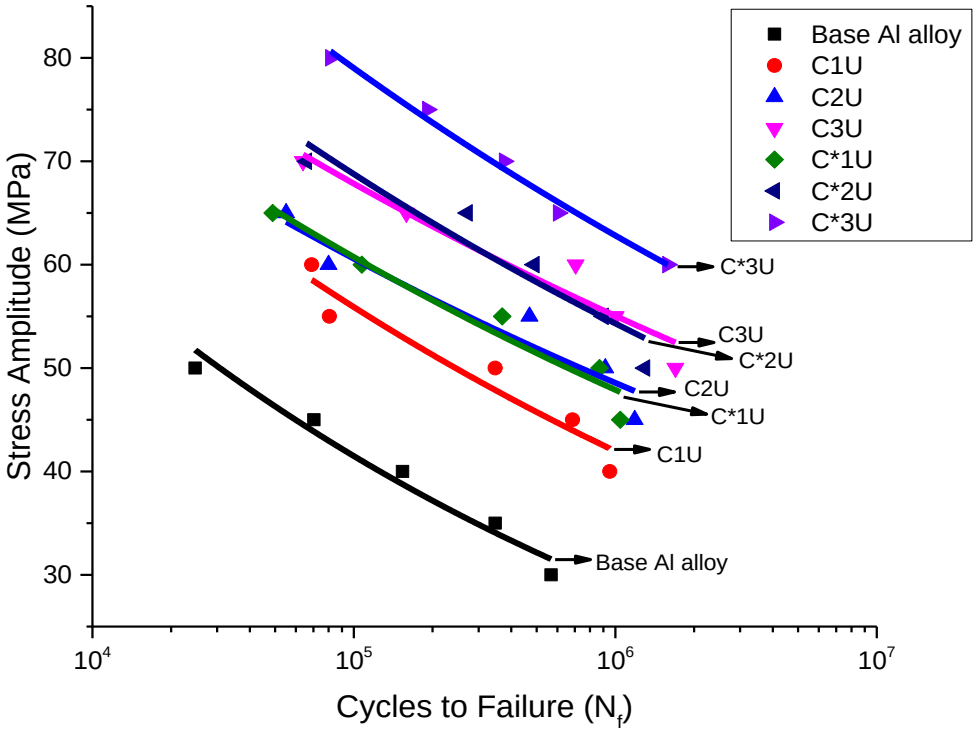

Figure 4. 33 S-N curves of the base Al alloy, Al_3Ti reinforced composites and Al_3Zr reinforced composites

In the high cycle fatigue regime where stresses are low, these improvements are more pronounced than that where stresses are high. For a given reinforcement volume fraction, when the particle size is decreased, interparticle spacing is also decreased which offer more resistance to the motion of reversible slip during fatigue and localized strain is also decreased due to cyclic slip refinement. Above a critical particle size, the propensity of the particle cracking is increased with the increasing particle size which results in predominant fracture of reinforcement contributing to premature fatigue failure. Fatigue life can also be improved by narrowing the particle size range distribution because larger particles are more prone to cracking [36]. It has been reported by Wallin et al. [304] that as the particle size is increased its probability to fracture is also increased, which is described by the following equations:

$$P(fr) = 1 - \exp\left[-\left(\frac{d}{\bar{d}}\right)^3 \times f(\sigma)\right] \qquad 4.22$$

where $f(\sigma)$ is defined as

$$f(\sigma) = \left(\frac{\bar{d}}{d_N}\right)^3 \times \frac{\left(\sigma_{flow}^{matrix} - \sigma_{min}^{matrix}\right)^m}{\sigma_1^m} \qquad 4.23$$

where d refers to the particle size. The other terms are defined on page xv

From the above equation, it can be concluded that the probability of the small sized reinforced particles to be fractured is also small.

Other factors that affect high cycle fatigues are matrix microstructure and particle–matrix bonding. Armstrong et al. [305] have proposed that the effect of grain size on the fatigue limit stress (σ_{FL}) can be given as:

$$\sigma_{FL} = \sigma_{o_{FL}} + k_{FL} d^{-1/2} \quad 4.24$$

where σ_{FL}, σ_{0FL}, k_{FL} and d are the fatigue limit, original fatigue limit, constant and average grain size, respectively. It is observed that the fatigue limit is inversely proportional to the average grain size which means that the fatigue life is improved as the average grain size is decreased. Therefore, increased HCF life of the composites over the base Al alloy is observed due to finer grains of the matrix.

In in-situ technique, bonding between particle and matrix is very strong as no reaction layer is formed which enhance the load bearing capacity of the composite. The clean interface between matrix and reinforced particle improves high cycle fatigue of the composites.

In this work, the developed composites have shown improved high cycle fatigue over the base Al alloy due to higher elastic modulus of the reinforced particles, the finer grains size of the matrix, clean interface between Al matrix and the particles, and uniform distribution of the particles throughout the matrix. However, Al_3Zr reinforced Al composites has shown improvement in HCF over the Al_3Ti reinforced composites, although volume fraction of the reinforced particles and average grain size of the developed composites are almost similar. This improvement can be attributed to the presence of Al_3Zr particles in the matrix which is around 50 % smaller in diameter than the Al_3Ti particles due to which its probability to be fractured is also less than that of Al_3Ti particle.

In Al alloy, persistent slip bands (PSBs) are major intrinsic sites to initiate crack, whereas, in the Al matrix composites, both PSBs and fractured reinforced particles are major intrinsic sites to initiate failure [300]. However, in the HCF regime, initiation of fatigue crack at the PSBs is significantly reduced due to existence of extrinsic crack initiation sites [306,307].

The size of the reinforcing particles governs the intrinsic crack initiation site. In the particle reinforced composites, the crack initiations occur at the sites where large size particles fracture [308]. Many researchers drew the same conclusions for the composites reinforced with particles which are large in size [295,309].

The sites for extrinsic crack initiation are related with the presence of porosity and clusters of the particle in the matrix. Particle clusters are broken by ultrasonication as discussed above. Porosity due to gas entrapment is also significantly reduced by ultrasonication [310].

The crack initiation and the crack growth rate govern fatigue life. In metallic materials, fraction of the total life to initiate crack is defined by the ratio between the crack initiation life (N_i) and the total fatigue life (N_f). Crack initiation occurs very early in fatigue life in the low cycle fatigue regime. Therefore, the life of crack growth dominates the fatigue life, and the N_i/N_f is low. In the HCF regime, crack initiation dominates the fatigue life which means Ni/Nf is close to unity [311,312]. Therefore, HCF should be investigated by considering the crack initiation.

4.3.2 Fractography:

The crack initiation point in the fracture surface of the base Al alloy and the composites is shown in Figure 4.34. Cracks often initiated at defects or weak points on the specimen surface as discussed above. However, crack initiation sites in PRMMCs are more diverse due to the particle additions. The interface between matrix and the particle is an important crack initiation site [313]. During cyclic deformation, stresses are concentrated at

and near the interface between the matrix and the particle due to the mismatch that exists between them, which may cause the separation of the particles from the matrix or premature failure of the matrix. Llorca and Poza [309], on the other hand, reported that under cyclic deformation, reinforcement fracture was the dominant damage mechanism. Besides intrinsic sites, there may be extrinsic sites such as porosity, particle clusters and other casting defects which cause crack initiation.

It is also observed from the Figure 4.34 (b) and (c) that the composites have undergone more plastic deformation as more dimples are formed than that of the base Al alloy, as shown in Figure 4.34 (a), where fewer dimples and tear ridges are formed due to stress localization. The driving force relative to the facet type brittle fracture may decrease due to the formation of dimples. As a result, the crack propagation rate is lower in the composite than that in the base Al alloy because plastic deformation at a crack tip leads to crack blunting.

The striation marks in the base Al alloy and the developed composites is shown in Figure 4.35. The micrographs show fatigue striations of approximately 1 μm in the base Al alloy as shown in Figure 4.35 (a). During cyclic loading, fatigue crack growth is indicated by these striations. For understanding the growth of fatigue crack under the process of cyclic slip, various models have been proposed [314]. According to these models, during one cycle of fatigue, continuous sharpening, blunting and re-sharpening of crack tips form fatigue striations. These striations are nothing but closely spaced tiny ridges and the distance between them govern the growth of the fatigue crack. The fatigue crack growth will be more if the distance between the striations is large as reported in the literature [314].

The fracture surface of the composite, as shown in Figure 4.35 (b-g), reveals fine gentle steps of the fatigue striations as compared to the base Al alloy which can be attributed to the presence of the in-situ particles. As observed from the figure, the width of these striations is ~0.2 μm which is less than that of the base Al alloy. This indicates that due to

low fatigue crack growth rate, the fatigue strength of the developed composites is improved over the base Al alloy.

It has been reported that the coherency of the particles with the matrix also governs the fatigue crack growth rate. The presence of coherent particles in the composite reduce fatigue crack growth because it favours zig-zag crack growth and the planar reversible slip [315]. Some secondary cracks with different depth between fatigue striations are observed as shown in Figure 4.35 (c) and (d). These secondary cracks are formed due to the stress concentration [316].

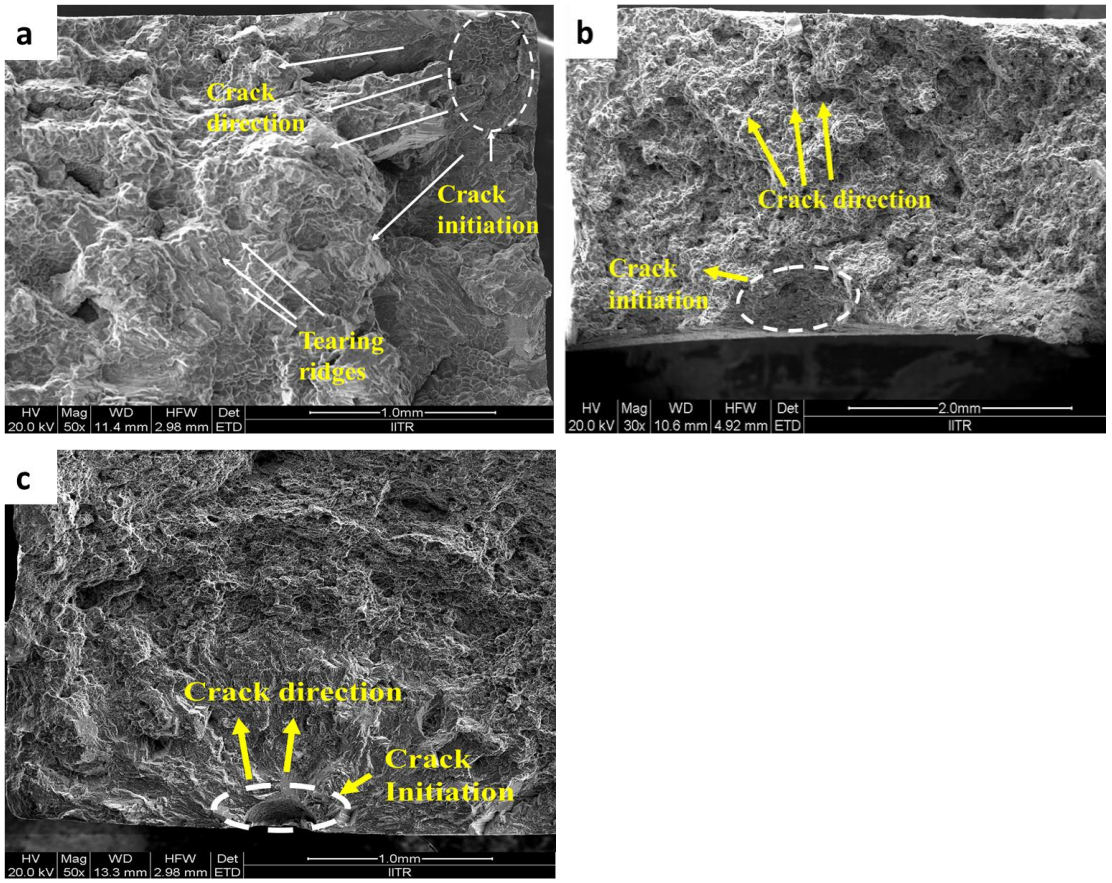

Figure 4. 34 SEM micrograph of crack initiation and propagation direction of (a) base Al alloy; (b) Al_3Ti reinforced Al alloy composite and (c) Al_3Zr reinforced Al alloy composite

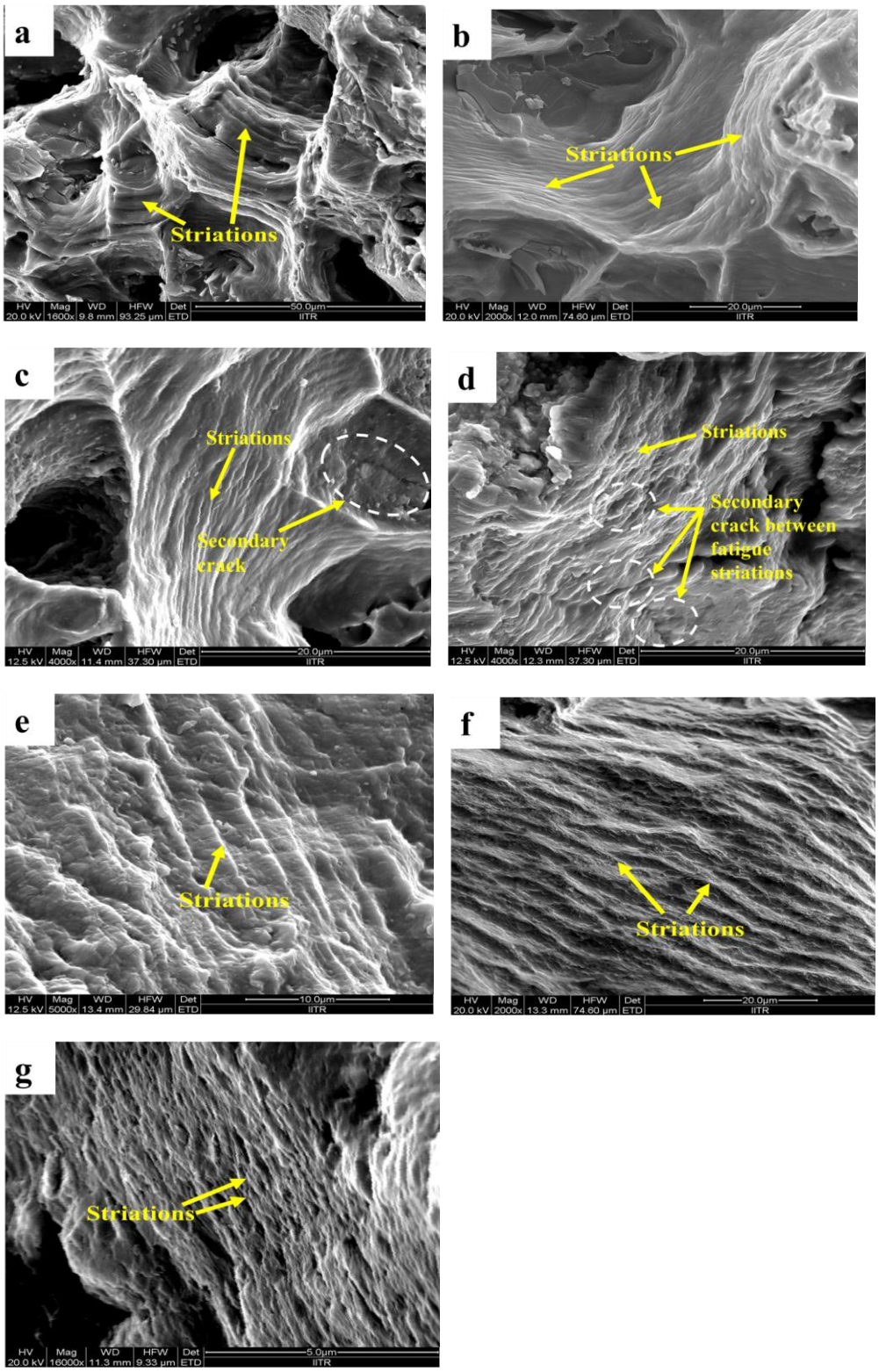

Figure 4. 35 SEM micrograph of striations mark in (a) base Al alloy, (b) C1U, (c) C2U, (d) C3U, (e)C*1U, (f) C*2U and (g) C*3U

4.3.3 Summary:

High cycle fatigue behaviour of in-situ Al-Al_3Ti and Al-Al_3Zr composites is investigated. The S-N curves indicate that the fatigue resistance of the composites improved over the base Al alloy suggesting that particle addition is beneficial. The reinforced particles lowered crack propagation rates by acting as crack stoppers or/and deflecting the growth planes of the main and secondary cracks. Therefore, as the amount of reinforcement is increased, the fatigue life of the composites also increased. Composites reinforced with Al_3Zr particles shown improved fatigue resistance over the composites reinforced with Al_3Ti particles because in-situ formed Al_3Zr particles, which had average size of 1.8 ± 0.8 μm, were smaller in size than the in-situ formed Al_3Ti particles which had average size of 3.4 ± 1.2 μm. Due to smaller particle, no particle cracking was observed in the process of crack initiation and propagation. Grain refinement of the matrix due to the presence of the particles, uniform distribution of the particle and removal of the porosity due to ultrasonication, clean interface and coherency between particle and matrix also contributed in the improvement of fatigue life. The fatigue resistance of in-situ composite tended to decrease with increasing stress amplitude. The fracture surface of the base Al alloy was brittle in nature consisting of tear ridges while the fracture surface of the composites was appeared to be ductile with dimples which was formed due to nucleation and growth of voids. Also, finer striations marks were observed in the composites indicative of low fatigue crack growth compared to the base alloy.

CHAPTER 5
CONCLUSIONS AND FUTURE SCOPE

The following conclusions are drawn from the present research work:

1. Aluminium composites with different weight percent of Al_3Ti and Al_3Zr particles were developed by in-situ reaction of aluminium alloy with potassium hexafluorotitanate (K_2TiF_6) and potassium hexafluorozirconate (K_2ZrF_6) respectively. Ultrasonication of the aluminium melt during salt reaction was carried out to refine the cast microstructure and achieve better dispersion of in-situ formed Al_3Ti and Al_3Zr particles. These particles generated in the melt promoted heterogeneous nucleation, which was responsible for grain refinement of the cast microstructure. The well dispersed particles significantly improved the mechanical properties including ductility, yield strength (YS), ultimate tensile strength (UTS) and hardness. The contribution of different strengthening mechanisms namely Hall-Petch strengthening and thermal mismatch strengthening in the yield strength of the composites were quantified. However, the contribution by thermal mismatch strengthening in yield strength was more as compared to Hall-Petch strengthening. The mechanical properties of the in-situ Al_3Zr reinforced composite was better than the in-situ Al_3Ti reinforced composite.
2. Creep analysis of the developed composites was carried out in the temperatures ranging from 543 to 603 K, and stresses between 113 and 170 MPa. The results obtained from creep analysis revealed that the composites had higher activation energy and stress exponent compared to the base alloy. The improved creep behaviour is attributed to the presence of homogeneously distributed these particles in the aluminium matrix. The obtained stress exponent and activation energy values suggest that the main creep mechanism in the base Al alloy and the developed composites was lattice diffusion-controlled dislocation climb.

3. High cycle fatigue behaviour of the developed composites was investigated for stress ratio R = 0.1 and compared with each other. The results obtained from high cycle fatigue analysis revealed that both the composites had higher fatigue life as compared to the base Al alloy due to uniform dispersion of reinforced particles, refinement of the matrix and clear interface between the particles and the matrix. It was observed from the comparison of high cycle fatigue between the two developed composites that the Al_3Zr reinforced Al composites had higher fatigue life as compared to Al_3Ti reinforced composites under any stress amplitude. This improvement was mainly due to presence of fine in-situ Al_3Zr particles, whose average size was 1.8 ± 0.8 μm, which was around 50% smaller than the in-situ Al_3Ti particles whose average size was 3.4 ± 1.2 μm.

5.1 Future scope:

The following open questions need to be addressed before these composites find applications as automobile components:

1. Studies on impression creep at high temperature and low stress can be conducted to analyse the diffusional creep in the composites.
2. Low cycle fatigue behaviour and fracture toughness of the composites need to be analysed.
3. Ultrasonication with continuous cooling can be done for incorporating the refinement of the matrix due to cavitation.
4. The phenomena of improvement of ductility with increased reinforcement of ultrasonically treated composite is to be studied further.

LIST OF PUBLICATIONS

Journal papers

1. **Rahul Gupta,** G.P. Chaudhari, B.S.S. Daniel, "Strengthening mechanisms in ultrasonically processed aluminium matrix composite with in-situ formed Al_3Ti reinforcement by salt addition" Composites Part B (Elsevier), Vol. 140, pp. 27-34, 2018.
2. **Rahul Gupta,** B.S.S. Daniel, "Impression creep of ultrasonically prepared in-situ Al_3Ti reinforced aluminium composite" Material Science and Engineering A (Elsevier), Vol. 733, pp. 257-266, 2018.
3. **Rahul Gupta**, B.S.S. Daniel, "Study on microstructure and mechanical Properties of ultrasonically processed in-situ Al_3Zr reinforced Al6061 alloy composite" (To be submitted).
4. **Rahul Gupta**, B.S.S. Daniel, "Impression creep behaviour of ultrasonically processed aluminium matrix composite reinforced with in-situ Al_3Zr" (To be submitted).
5. **Rahul Gupta**, B.S.S. Daniel, "High cycle fatigue behavior of ultrasonically processed in-situ Al 6061-Al_3Ti/Al_3Zr composites" (To be submitted).

Conference proceedings

1. **Rahul Gupta,** G.P. Chaudhari, B.S.S. Daniel, "Effect of in-situ formed Al_3Ti particles on the microstructure and mechanical properties of 6061 Al alloy ", IOP Conf. Series: Materials Science and Engineering, Vol. 330 (2018) 012012.
2. **Rahul Gupta,** B.S.S. Daniel, "Impression creep behaviour of in-situ Al_3Ti reinforced Al alloy composite fabricated by salt-melt reaction technique" Materials Today: Proceeding (Elsevier), Vol. 5, pp. 16936-16945, 2018.

Conference abstracts

1. **Rahul Gupta**, B.S.S. Daniel, “Impression creep behaviour of in-situ Al_3Ti reinforced Al alloy composite fabricated by salt-melt reaction technique”, in International conference (AMPCO, IIT Roorkee), 2017.
2. **Rahul Gupta**, B.S.S. Daniel, “In-situ Al_3Zr reinforced aluminium alloy composite by ultrasonic assisted salt-melt reaction technique”, in International conference (NMD-ATM), 2017.
3. **Rahul Gupta**, B.S.S. Daniel, “Effect of in-situ formed Al_3Ti particles on the microstructure and mechanical properties of 6061 Al alloy", in International Conference (ICRAMME, Hyderabad), 2017.
4. **Rahul Gupta**, B.S.S. Daniel, “Impression creep test of in-situ Al_3Ti reinforced Al6061 alloy composite using ultrasonication” in International conference (NMD-ATM), 2016.
5. **Rahul Gupta**, B.S.S. Daniel, “Processing and characterization of in-situ intermetallic Al_3Ti particles reinforced aluminium alloy metal matrix composite”, in International conference (NMD-ATM), 2015.
6. **Rahul Gupta**, B.S.S. Daniel, “In-situ intermetallic Al_3Ti particles reinforced aluminium alloy composite”, in International conference (NMD-ATM), 2014.

REFERENCES

[1] J. Chen, J. Li, Y. Zhou, In-situ Synthesis of Ti_3AlC_2/TiC-Al_2O_3 Composite from TiO_2-Al-C System, J. Mater. Sci. Technol. 22 (2006) 455–458.

[2] J. Zhang, H. Yu, H. Chen, G. Min, Al-Si/Al_2O_3 in situ composite prepared by displacement reaction of CuO/Al system, China Foundry. 7 (2010) 19–23.

[3] F. Technology, Preparation of Al – Al_2O_3 in-situ particle composites by addition of Fe_2O_3 particles to pure Al melt, J. Mater. Sci. Lett. 6 (1997) 1224–1226.

[4] D.. Dunand, B. Derby, Fundamentals of Metal Matrix Composites, Butterworth-Heinneman, Boston, 1993.

[5] M.K. Surappa, Aluminium matrix composites: Challenges and opportunities, Sadhana. 28 (2003) 319–334. doi:10.1007/BF02717141.

[6] R. Dasgupta, Aluminium Alloy-Based Metal Matrix Composites: A Potential Material for Wear Resistant Applications, ISRN Metall. 2012 (2012) 1–14. doi:10.5402/2012/594573.

[7] D.J. Lloyd, Particle reinforced aluminium and magnesium matrix composites, Int. Mater. Rev. 39 (1994) 1–23. doi:10.1179/imr.1994.39.1.1.

[8] D.J. Lloyd, The Solidification Microstructure of Particulate Reinforced Aluminium / SiC Composites, Comp. Sci. Tech. 35 (1989) 159–179.

[9] A. Kolsgaard, S. Brusethaug, Fluidity of aluminium alloy AlSi7Mg – SiC particulate composite melts Fluidity of aluminium alloy AISi7Mg-SiC, Mater. Sci. Tech. 10 (1994) 545-551.

[10] A. Luo, Processing, Microstructure and Mechanical behaviour of Cast Magnesium Metal Matrix Composites, Metall. Mater. Trans. A 26 (1995) 2445–2455.

[11] B.S.S. Daniel, V.S.R. Murthy, G.S. Murty, Metal-ceramic composites via in-situ methods, J. Mater. Proc. Techn. 68 (1997) 132-155.

[12] I.. Clyne, P.. Withers, An Introduction to Metal Matrix Composites, Cambridge

University Press, U.K, 1993.

[13] S. Hong, H. Kim, D. Huh, C. Suryanarayana, Effect of clustering on the mechanical properties of SiC particulate- reinforced aluminum alloy 2024 metal matrix composites, Mater. Sci. Eng. A 347 (2003) 198–204.

[14] J. Hashim, L. Looney, M.S.J. Hashmi, Metal matrix composites : production by the stir casting method, J. Mater. Proc. Techn. 92-93 (1999) 1–7.

[15] X. Jian, H. Xu, T.T. Meek, Q. Han, Effect of power ultrasound on solidification of aluminum A356 alloy, Mater. Lett. 59 (2005) 190–193.

[16] S. Djordjevic, The effects of ultrasonic solidification on aluminum, J. Min. Metall. 39 (3-4)B (2003) 527–532.

[17] V. Laurent, P. Jarry, G. Regazzoni, D. Apelian, Processing-microstructure relationships in compocast magnesium/SiC, J. Mater. Sci. 27 (1992) 4447–4459.

[18] B. Patel, G.P. Chaudhari, P.P. Bhingole, Microstructural evolution in ultrasonicated AS41 magnesium alloy, Mater. Lett. 66 (2012) 335–338.

[19] Y. Tsunekawa, H. Suzuki, Y. Genma, Application of ultrasonic vibration to in situ MMC process by electromagnetic melt stirring, Mater. Des. 22 (2001) 467–472. doi:10.1016/S0261-3069(00)00079-0.

[20] G.I. Eskin, D.G. Eskin, Production of natural and synthesized aluminum-based composite materials with the aid of ultrasonic (cavitation) treatment of the melt, Ultrason. Sonochemistry 10 (2003) 297–301.

[21] Y. Yang, J. Lan, X. Li, Study on bulk aluminum matrix nano-composite fabricated by ultrasonic dispersion of nano-sized SiC particles in molten aluminum alloy, Mater. Sci. Eng. A 380 (2004) 378–383. doi:10.1016/j.msea.2004.03.073.

[22] J. Lan, Y. Yang, X. Li, Microstructure and microhardness of SiC nanoparticles reinforced magnesium composites fabricated by ultrasonic method, Mater. Sci. Eng. A. 386 (2004) 284–290. doi:10.1016/j.msea.2004.07.024.

[23] J. Yuan, Q. Wang, D. Yin, H. Wang, C. Chen, B. Ye, Creep behavior of Mg – 9Gd – 1Y – 0 . 5Zr (wt .%) alloy piston by squeeze casting, Mater. Charact. 78 (2013) 37–46. doi:10.1016/j.matchar.2013.01.012.

[24] A. Vyawahare, A. V Kolhe, Analysis of Thermal Stresses Acting on Piston of C . I . Engine, Inter. J. Scient. Res. Develop. 2 (2015) 413–416.

[25] A. Arunachaleswaran, I.M. Pereira, H. Dieringa, Y. Huang, N. Hort, B.K. Dhindaw, K.U. Kainer, Creep behavior of AE42 based hybrid composites, Mater. Sci. Eng. A. 460–461 (2007) 268–276. doi:10.1016/j.msea.2007.01.043.

[26] A.K. Mondal, S. Kumar, Impression creep behaviour of magnesium alloy-based hybrid composites in the transverse direction, Compos. Sci. Technol. 69 (2009) 1592–1598. doi:10.1016/j.compscitech.2009.02.038.

[27] S.N.G. Chu, J.C.M. Li, Impression creep; a new creep test, J. Mater. Sci. 12 (1977) 2200–2208.

[28] D.H. Sastry, Impression creep technique — An overview, Mater. Sci. Eng. A. 409 (2005) 67–75. doi:10.1016/j.msea.2005.05.110.

[29] N. Chawla, C. Andres, J.W. Jones, J.E. Allison, Effect of SiC Volume Fraction and Particle Size on the Fatigue Resistance of a 2080 Al/SiCp Composite, Metall. Mater. Trans. A. 29 (1998) 2843–2854.

[30] A. Illgen, A. Weidner, H. Biermann, Influence of particle and short-fibre reinforcement on the very high cycle fatigue behaviour of aluminium matrix composites, Int. J. Fatigue. 113 (2018) 299–310. doi:10.1016/j.ijfatigue.2018.04.025.

[31] J.E. Allison, J.W. Jones, Fundamentals of Metal Matrix Composites, Butterworth-Heinemann, Stoneham, massachusetts, 1993.

[32] J.E. Allison, L.. Davis, J.W. Jones, Composites Engineering Handbook, Marcel Dekker, New York, 1997.

[33] M.M. Sharma, C.W. Ziemian, T.J. Eden, Fatigue behavior of SiC particulate

reinforced spray-formed 7XXX series Al-alloys, Mater. Des. 32 (2011) 4304–4309. doi:10.1016/j.matdes.2011.04.009.

[34] Y. Ochi, K. Masaki, T. Matsumura, M. Wadasako, Effects of volume fraction of alumina short fibers on high cycle fatigue properties of Al and Mg alloy composites, Mater. Sci. Eng. A 470 (2007) 230–236.

[35] M. Papakyriacou, H.R. Mayert S.E. Stanzl-Tschegg, M. Groschl, Fatigue properties of Al_2O_3 particle reinforced 6061 aluminium alloy in the high-cycle regime, Int. J. Fatigue 18 (1996) 475–481.

[36] N. Chawla, J.E. Allison, Fatigue of Particle Reinforced Materials, Encycl. Mater. Sci. Technol. (2001) 2967–2972.

[37] J.L. Murray, Calculation of the Titanium-Aluminum Phase Diagram, Metall. Trans. A 19 (1988) 243–247.

[38] V.I. Nikitin, E.G. Kandalova, A.G. Makarenko, L. Yong, Preparation of Al-Ti-B grain refiner by SHS, Scripta Mater. 42 (2000) 561–566.

[39] M. V Karpets, Y. V Milman, O.M. Barabash, N.P. Korzhova, O.N. Senkov, The influence of Zr alloying on the structure and properties of Al_3Ti, Intermetallics. 11 (2003) 241–249.

[40] L. Li, Y. Zhang, C. Esling, H. Jiang, Z. Zhao, Y. Zuo, J. Cui, Crystallographic features of the primary Al_3Zr phase in as-cast Al-1.36 wt. % Zr alloy, J. Cryst. Growth. 316 (2011) 172–176. doi:10.1016/j.jcrysgro.2010.12.063.

[41] M. Zedalis, M. Ghate, M. Fine, Elastic Moduli of Al_3Zr, Scr. Metall. 19 (1985) 647–650.

[42] G. Gautam, A. Mohan, Wear and Friction of AA5052-Al_3Zr In Situ Composites Synthesized by Direct Melt Reaction, J. Tribol. 138 (2015) 021602.

[43] G. Chen, X. Song, N. Hu, H. Wang, Y. Tian, Effect of initial Ti powders size on the microstructures and mechanical properties of Al_3Ti / 2024 Al composites prepared by

ultrasonic assisted in-situ casting, J. Alloys Compd. 694 (2017) 539–548.

[44] Y. Watanabe, N. Yamanaka, Y. Fukui, Wear Behavior of Al-Al_3Ti Composite Manufactured by a Centrifugal Method, Metall. Mater. Trans. A 30 (1999) 3253–3261.

[45] Y. Watanabe, H. Eryu, K. Matsuura, Evaluation of three-dimensional orientation of Al_3Ti platelet in al-based functionally graded materials fabricated by a centrifugal casting, Acta Mater. 49 (2001) 775–783.

[46] Y. Watanabe, A. Kawamoto, K. Matsuda, Particle size distributions in functionally graded materials fabricated by the centrifugal solid-particle method, Compos. Sci. Techn. 62 (2002) 881–888.

[47] P.D. Sequeira, Y. Watanabe, L.A. Rocha, Particle Distribution and Orientation in Al-Al_3Zr and Al-Al_3Ti FGMs Produced by the Centrifugal Method, Mater. Sci. Forum 492-493 (2005) 609–614. doi:10.4028/www.scientific.net/MSF.492-493.609.

[48] P.D. Sequeira, Y. Watanabe, L.A. Rocha, Aluminum matrix texture and particle characterization in Al-Al_3Ti FGMs produced by a centrifugal solid-particle method, Solid State Phenom. 105 (2005) 415–420.

[49] S.C. Ferreira, P.D. Sequeira, Y. Watanabe, E. Ariza, L.A. Rocha, Microstructural characterization and tribocorrosion behaviour of Al/Al_3Ti and Al/Al_3Zr FGMs, Wear 270 (2011) 806–814. doi:10.1016/j.wear.2011.02.007.

[50] S. Zhang, Y. Zhao, G. Chen, X. Cheng, Q. Dai, Microstructures and mechanical properties of aluminum matrix composites fabricated from Al – x wt .% Zr $(CO_3)_2$ (x=5, 10, 15, 20, 25) systems, J. Alloys Comp. 429 (2007) 198–203.

[51] S. Zhang, Y. Zhao, G. Chen, X. Cheng, Microstructures and dry sliding wear properties of in situ (Al_3Zr + ZrB_2)/Al composites, J. Mater. Process. Tech. 184 (2007) 201–208. doi:10.1016/j.jmatprotec.2006.11.023.

[52] Z. Yu-tao, Z. Song-li, C. Gang, Aluminum matrix composites reinforced by in situ

Al_2O_3 and Al_3Zr particles fabricated via magnetochemistry reaction, Trans. Nonferrous Met. Soc. China. 20 (2010) 2129–2133.

[53] J.J. Moses, I.Dinaharan, S.J.Sekhar, Characterization of silicon carbide particulate reinforced AA6061 aluminium alloy composites produced via stir casting, Procedia Mater. Sci. 5 (2014) 106–112. doi:10.1016/j.mspro.2014.07.247.

[54] Y.C. Kang, S.L.I. Chan, Tensile properties of nanometric Al_2O_3 particulate-reinforced aluminum matrix composites, Mater. Chem. Phys. 85 (2004) 438–443.

[55] Y. Choi, M.E. Mullins, K. Wijayatilleke, J.K. Lee, Fabrication of Metal Matrix Composites of TiC-Al through Self-Propagating Synthesis Reaction, Metall. Trans. A 23 (1992) 2387–2392.

[56] I. Gotman, M.. Koczak, E. Shtessel, Fabrication of Al matrix in situ composites via self-propagating synthesis, Mater. Sci. Eng. A. 187 (1994) 189–199.

[57] X.C. Tong, Fabrication of in situ TiC reinforced aluminum matrix composites Part I Microstructural characterization, J. Mater. Sci. 3 (1998) 5365–5374.

[58] T.. Sudarshan, T.. Srivatsan, Rapid Solidification Technology: an Engineering Guide, Technomic Publishing, Pennsylvania, USA, 1993.

[59] X.C. Tong, H.S. Fang, Al-TiC Composites In Situ – Processed by Ingot Metallurgy and Rapid Solidification Technology : Part I . Microstructural Evolution, Metall. Mater. Trans. A 29 (1998) 875–891.

[60] X.C. Tong, H.S. Fang, Al-TiC Composites In Situ – Processed by Ingot Metallurgy and Rapid Solidification Technology : Part II . Mechanical Behavior, Metall. Mater. Trans. A 29 (1998) 893-902.

[61] Z.. Ma, J. Bi, Y.. Lu, H.. Shen, Y.. Gao, Microstructure and Interface of the in situ Forming TiB_2-Reinforced Aluminium Composite, Compos. Interfaces. 1 (1993) 287–291.

[62] Z.Y. Ma, S.C. Tjong, In Situ Ceramic Particle-Reinforced Aluminum Matrix

Composites Fabricated by Reaction Pressing in the TiO_2 (Ti) -Al-B (B_2O_3) Systems, Metall. Mater. Trans. A 28 (1997) 1931–1942.

[63] S.C. Tjong, G.S. Wang, Y.-W. Mai, High cycle fatigue response of in-situ Al-based composites containing TiB_2 and Al_2O_3 submicron particles, Compos. Sci. Technol. 65 (2005) 1537–1546. doi:10.1016/j.compscitech.2005.01.012.

[64] D.C. Dunand, J.L. Sommer, A. Mortensen, Synthesis of Bulk and Reinforced Nickel Aluminides by Reactive Infiltration, Metall. Trans. A 24 (1993) 2161-2170.

[65] M.R. Hanabe, P.B. Aswath, Al_2O_3/Al particle-reinforced aluminum matrix composite by displacement reaction, J. Mater. Res. 11 (1996) 1562–1569.

[66] M. Hanabe, P.B. Aswath, Synthesis of in-situ reinforced Al composites from Al-Si-Mg-O precursors, Acta Mater. 45 (1997) 4067-4076.

[67] H. Fukunaga, X. Wang, Preparation of intermetallic compound matrix composites by reaction squeeze casting, Mater. Sci. Lett. 9 (1990) 23–25.

[68] J. Pan, J. Li, H. Fukunaga, X. Ning, H. Ye, Z. Yao, D. Yang, Microstructural Study of the Interface Reaction Between Titania Whiskers and Aluminium, Compos. Sci. Technol. 51 (1997) 319–325.

[69] A. Kuruvilla, K. Prasad, V. Bhanuprasad, Y. Mahajan, Microstructure-property correlation in $AlTiB_2$ (XD) composites, Scr. Metall. Mater. 24 (1990) 873–878.

[70] G.M. Vyletel, D.C. Van Aken, J.E. Allison, Effect of microstructure on the cyclic response and fatigue behavior of an XD^{TM} aluminum metal matrix composite, Scr. Metall. 25 (1991) 2405–2410.

[71] G.M. Vyletel, J.E. Allison, D.C.V. Aken, The Influence of Matrix Microstructure and TiC Reinforcement on the Cyclic Response and Fatigue Behavior of 2219 Al, Metall. Trans. A 24 (1993) 2545–2557.

[72] M. Koczak, K. Kumar, Insitu process for producing a composte containing refractory material, Patent No. 4808372, 1989.

[73] M.K. Premkumar, M.G. Chu, Synthesis of TiC Particulates and Their Segregation during Solidification, Metall. Mater. Trans. A. 80 (1993) 2358–2359.

[74] M.. Premkumar, M.. Chu, A1-TiC particulate composite produced by a liquid state in situ process, Mater. Sci. Eng. A. 202 (1995) 172–178.

[75] C. Suryanarayana, Mechanical Alloying and Milling, CRC press, New York, 2004.

[76] B. Srinivasarao, C. Suryanarayana, K. Oh-ishi, K. Hono, Microstructure and mechanical properties of Al–Zr nanocomposite materials, Mater. Sci. Eng. A. 518 (2009) 100–107. doi:10.1016/j.msea.2009.04.032.

[77] K. Satyaprasad, Y.R. Mahajan, V.V. Bhanuprasad, Strengthening of Al/20 vol. pct TiC composites by isothermal heat treatment, Scr. Metall. Mater. 26 (1992) 711–716.

[78] Y.T. Zhao, G.X. Sun, In situ synthesis of novel composites in the system Al-Zr-O, J. Mater. Sci. Lett. 20 (2001) 1859–1861.

[79] Y.T. Zhao, X.N. Cheng, Q.X. Dai, L. Cai, G.X. Sun, Crystal morphology and growth mechanism of reinforcements synthesized by direct melt reaction in the system Al-Zr-O, Mater. Sci. Eng. A. 360 (2003) 315–318. doi:10.1016/S0921-5093(03)00474-X.

[80] Y.T. Zhao, Q.X. Dai, X.N. Cheng, S.C. Sun, Microstructure and properties of in-situ synthesized ($Al_3Zr+Al_2O_3$)p/A356 composites, Int. J. Mod. Phys. B. 17 (2003) 1292–1296.

[81] P. Rohatgi, Cast Aluminum-Matrix Composites for Automotive Applications, J. Miner. Met. Mater. Soc. 43 (1991) 10–15.

[82] R. Agarwal, A. Mohan, S. Mohan, R.K. Gautam, Synthesis and Characterization of Al/Al_3Fe Nanocomposite for Tribological Applications, J. Tribol. 136 (2014) 012001 (1-9). doi:10.1115/1.4025601.

[83] R.A. Carden, Metal matrix composite, Patent No. 5980602, 1999.

[84] K. Il Moon, S.C. Kim, K.S. Lee, A study on the microstructure of $D0_{23}$ Al_3Zr and L1

2 (Al + 12 . 5 at .% Cu)$_3$Zr intermetallic compounds synthesized by PBM and SPS, Intermetallics. 10 (2002) 185–194.

[85] Z. Jinxu, H.U. Gengxiang, W.U. Jiansheng, Electron structure and bonding characteristics of Al 3 Ti intermetallic alloys, J. Mater. Sci. Lett. 19 (2000) 1685–1686.

[86] M. Takeda, T. Kikuchi, S. Makihara, Stabilizing effects of third elements on an L12-Al_3Ti compound, J. Mater. Sci. Lett. 18 (1999) 631–634.

[87] Y. V Milman, D.B. Miracle, S.I. Chugunova, I. V Voskoboinik, N.P. Korzhova, Mechanical behaviour of Al_3Ti intermetallic and L12 phases on its basis, Intermetallics. 9 (2001) 839–845.

[88] S.H. Wang, P.W. Kao, The strengthening effect of Al_3Ti in high temperature deformation of Al ± Al_3Ti composites, Acta Mater. 46 (1998) 2675–2686.

[89] S.H. Wang, P.W. Kao, C.P. Chang, The strengthening effect of Al_3Ti in ultrafine grained Al-Al_3Ti alloys, Scr. Mater. 40 (1999) 289–295.

[90] G.M. Swallowe, J.E. Field, C.S. Rees, A. Duckworth, A photographic study of the effect of ultrasound on solidification, Acta Metall. 37 (1989) 961–967.

[91] O. V Abramov, Action of high intensity ultrasound on solidifying metal, Ultrasonics. 25 (1987) 73–82.

[92] J.R.G. Sander, B.W. Zeiger, K.S. Suslick, Sonocrystallization and sonofragmentation, Ultrason. Sonochem. 21 (2014) 1908–1915. doi:10.1016/j.ultsonch.2014.02.005.

[93] K.S. Suslick, Y. Didenko, M.M. Fang, T. Hyeon, K.J. Kolbeck, W.B. Mcnamara III, M.M. Mdleleni, m. Wong, Acoustic cavitation and its chemical consequences, Phil. Trans. R. Soc. Lond. A. 357 (1999) 335–353.

[94] X. Li, Y. Yang, X. Cheng, Ultrasonic-assisted fabrication of metal matrix nanocomposites, J. Mater. Sci. 9 (2004) 3211–3212.

[95] G. Cao, H. Konishi, X. Li, Recent developments on ultrasonic cavitation based

solidification processing of bulk magnesium nanocomposites, Int. J. Met. 2 (2008) 57–65.

[96] G. Cao, H. choi, H. Konishi, S. Kou, R. Lakes, X. Li, Mg–6Zn/1.5% SiC nanocomposites fabricated by ultrasonic cavitation-based solidification processing, J. Mater. Sci. 43 (2008) 5521–5526.

[97] L. Chen, J. Peng, J. Xu, Achieving uniform distribution and dispersion of a high percentage of nanoparticles in metal matrix nanocomposites by solidification processing, Scr. Mater. 69 (2013) 634–637. doi:10.1016/j.scriptamat.2013.07.016.

[98] S. Jia, D. Zhang, Y. Xuan, L. Nastac, An experimental and modeling investigation of aluminum-based alloys and nanocomposites processed by ultrasonic cavitation processing, Appl. Acoust. 103 (2016) 226–231. doi:10.1016/j.apacoust.2015.07.016.

[99] G. Cao, H. Konishi, X. Li, Mechanical properties and microstructure of SiC-reinforced Mg-(2, 4) Al-1Si nanocomposites fabricated by ultrasonic cavitation based solidification processing, Mater. Sci. Eng. A. 486 (2008) 357–362.

[100] I.T.G.S.B. Lebon, D.G.E.K. Pericleous, Effect of Input Power and Temperature on the Cavitation Intensity During the Ultrasonic Treatment of Molten Aluminium, Trans. Indian Inst. Met. 68 (2015) 1023–1026. doi:10.1007/s12666-015-0639-0.

[101] H. Dieringa, Properties of magnesium alloys reinforced with nanoparticles and carbon nanotubes : a review, J. Mater. Sci. 46 (2011) 289–306. doi:10.1007/s10853-010-5010-6.

[102] I. Tzanakis, G.S.B. Lebon, D.G. Eskin, K.A. Pericleous, Characterizing the cavitation development and acoustic spectrum in various liquids, Ultrason. Sonochem. 34 (2017) 651–662. doi:10.1016/j.ultsonch.2016.06.034.

[103] H. Puga, S. Costa, J. Barbosa, S. Ribeiro, M. Prokic, Influence of ultrasonic melt treatment on microstructure and mechanical properties of AlSi9Cu3 alloy, J. Mater. Process. Tech. 211 (2011) 1729–1735. doi:10.1016/j.jmatprotec.2011.05.012.

[104] X. Jian, H. Xu, T.T. Meek, Q. Han, Effect of power ultrasound on solidification of aluminum A356 alloy, Mater. Lett. 59 (2005) 190–193.

[105] L.Z.D.G.E.L. Katgerman, Influence of ultrasonic melt treatment on the formation of primary intermetallics and related grain refinement in aluminum alloys, J. Mater. Sci. 46 (2011) 5252–5259. doi:10.1007/s10853-011-5463-2.

[106] F. Wang, D. Eskin, T. Connolley, J. Mi, Effect of ultrasonic melt treatment on the refinement of primary Al_3Ti intermetallic in an Al–0.4Ti alloy, J. Cryst. Growth. 435 (2016) 24–30. doi:10.1016/j.jcrysgro.2015.11.034.

[107] M. Qian, A. Ramirez, A. Das, Ultrasonic refinement of magnesium by cavitation : Clarifying the role of wall crystals, J. Cryst. Growth. 311 (2009) 3708–3715. doi:10.1016/j.jcrysgro.2009.04.036.

[108] P.P. Bhingole, G.P. Chaudhari, Synergy of nano carbon black inoculation and high intensity ultrasonic processing in cast magnesium alloys, Mater. Sci. Eng. A. 556 (2012) 954–961. doi:10.1016/j.msea.2012.07.104.

[109] Eskin GI, Ultrasonic treatment of light alloy melts, Gordon & Breach, Amsterdam, 1998.

[110] J.D. Hunt, K.A. Jackson, Nucleation of Solid in an Undercooled Liquid by Cavitation Nucleation of Solid in an Undercooled Liquid by Cavitation, J. Appl. Phys. 37 (1998) 254–257. doi:10.1063/1.1707821.

[111] L. Nastac, Modeling and simulation of microstructure evolution in solidifying alloys, Kluwer Academic Publishers, 2004.

[112] H. Xu, X. Jian, T.T. Meek, Q. Han, Degassing of molten aluminum A356 alloy using ultrasonic vibration, Mater. Lett. 58 (2004) 3669–3673.

[113] N. Alba-baena, T. Pabel, N. Villa-sierra, D. Eskin, Effect of Ultrasonic Melt Treatment on Degassing and Structure of Aluminium Alloys, Mater. Sci. Forum. 765 (2013) 271–275.

[114] N. Alba-baena, D. Eskin, Kinetics of ultrasonic degassing of aluminum alloys, Light Met. TMS, 2013. (2013) 957–958.

[115] R. Haghayeghi, H. Bahai, P. Kapranos, Effect of ultrasonic argon degassing on dissolved hydrogen in aluminium alloy, Mater. Lett. 82 (2012) 230–232. doi:10.1016/j.matlet.2012.05.112.

[116] H. Puga, J. Barbosa, E. Seabra, S. Ribeiro, M. Prokic, The influence of processing parameters on the ultrasonic degassing of molten AlSi9Cu3 aluminium alloy, Mater. Lett. 63 (2009) 806–808. doi:10.1016/j.matlet.2009.01.009.

[117] G.I. Eskin, Broad prospects for commercial application of the ultrasonic (cavitation) melt treatment of light alloys, Ultrason. Sonochemistry. 8 (2001) 319–325.

[118] T. Leong, M. Ashokkumar, S. Kentish, The fundamentals of power ultrasound – a review, Acoust. Aust. 39 (2011) 43–52.

[119] W.W. Xu, I. Tzanakis, P. Srirangam, W.U. Mirihanage, D.G. Eskin, A.J. Bodey, P.D. Lee, Synchrotron quantification of ultrasound cavitation and bubble dynamics in Al–10Cu melts, Ultrason. Sonochem. 31 (2016) 355–361.

[120] G.I. Eskin, Cavitation mechanism of ultrasonic melt degassing, Ultrason. Sonochem. 2 (1995) 137–141.

[121] O. Article, Acceleration of Fibrinolysis by High-frequency Ultrasound : The Contribution, Thromb. Res. 100 (2000) 333–340.

[122] S. Hyun, D. Lee, Investigation of convective heat transfer augmentation using acoustic streaming generated by ultrasonic vibrations, Int. J. Heat Mass Transf. 48 (2005) 703–718. doi:10.1016/j.ijheatmasstransfer.2004.07.048.

[123] T. Leighton, The acoustic bubble, Acadmic Press, USA, 1994.

[124] H.C. Starritt, F.A. Duck V.F. Humphrey, Forces acting in the direction of propagation in pulsed ultrasound fields, Phys. Med. Biol. 36 (1991) 1465–1474.

[125] R. Island, Acoustic Streaming near a Boundary sound Defining sketch, J. Acoust. Soc.

Am. 30 (1958) 329–339.

[126] Z. Liu, Q. Han, J. Li, W. Huang, Effect of ultrasonic vibration on microstructural evolution of the reinforcements and degassing of in situ TiB_2p/Al–12Si–4Cu composites, J. Mater. Process. Tech. 212 (2012) 365–371.

[127] Z.W. Liu, M. Rakita, Q. Han, J.G. Li, Microstructural evolution of reinforcements in the remelting in situ TiC /Al–12Si composites treated by ultrasonic vibration, Mater. Res. Bull. 46 (2011) 1674–1678.

[128] Z. Liu, Q. Han, J. Li, Ultrasound assisted in situ technique for the synthesis of particulate reinforced aluminum matrix composites, Compos. Part B Eng. 42 (2011) 2080–2084. doi:10.1016/j.compositesb.2011.04.004.

[129] A. Williams, DNA degradation by acoustic microstreaming, J. Acoust. Soc. Am. 55 (1974) 17–22.

[130] A.R. Williams, J.S. Slade, Ultrasonic dispersal of aggregates of Sarcina lutea, Ultrasonics. 9 (1971) 85–87.

[131] T.J. Mason, J.. Lorimer, Applied Sonochemistry: The uses of power ultrasound in chemistry and processing, Wiley-VCH, Germany, 2002.

[132] K.S. Suslick, Ultrasound: its chemical, physical, and biological effects, VCH, New York, 1988.

[133] K.S. Suslick, Sonochemistry, Science 247 (1990) 1439–1445.

[134] K.S. Suslick, N.C. Eddingsaas, D.J. Flannigan, S.D. Hopkins, H. Xu, Extreme conditions during multibubble cavitation : Sonoluminescence as a spectroscopic probe, Ultrason. Sonochemistry. 18 (2011) 842–846.

[135] G.E. Dieter, Mechanical Metallurgy, S.I. Metri, Mcgraw-Hill, UK, 1988.

[136] S. Jonsson, Mechanical Properties of Metals and Dislocation Theory from an Engineer’s Perspective, Department of Materials Science and Engineering, Royal Institute of Technology, 2007.

[137] H. Altenbach, Topical problems and applications of creep theory, Int. Appl. Mech. 39 (2003) 631–655.

[138] T.H. Hyde, W. Sun, J.A. Williams, Creep analysis of pressurized circumferential pipe weldments-a review, J. Strain Anal. 38 (2003) 1–29.

[139] T.H. Hyde, W. Sun, C.J. Hyde, Applied Creep Mechanics, McGraw-Hill Education, USA, 2014.

[140] R.K. Penny, D.L. Marroitt, Design for Creep, Chapman and Hall, London, UK, 1995.

[141] M. Ashby, H. Shercliff, D. Cebon, Materials Engineering, Science, Processing and Design, Butterworth-Heinemann, Oxford, UK, 2014.

[142] B. Wilshire, M.T. Whittaker, The role of grain boundaries in creep strain accumulation, Acta Mater. 57 (2009) 4115–4124.

[143] B. Wilshire, M. Willis, I.I.E. Procedures, Mechanisms of Strain Accumulation and Damage Development during Creep of Prestrained 316 Stainless Steels, Metall. Mater. Trans. A. 35A (2004) 563–571.

[144] H. Kraus, Creep Analysis, John Wiley & Sons, Inc., New York, USA, 1980.

[145] C.J. Hyde, T.H. Hyde, W. Sun, S. Nardone, E. De Bruycker, Small ring testing of a creep resistant material, Mater. Sci. Eng. A. 586 (2013) 358–366.

[146] T.H. Hyde, W. Sun, J.A. Williams, Requirements for and use of miniature test specimens to provide mechanical and creep properties of materials :a review, Int. Mater. Rev. 52 (2007) 213–255.

[147] T.H. Hyde, W. Sun, Evaluation of conversion relationships for impression creep test at elevated temperatures, Int. J. Press. Vessel. Pip. 86 (2009) 757–763.

[148] T.H. Hyde, W. Sun, A novel high-sensitivity small specimen creep test, J. Strain Anal. 44 (2009) 171–185.

[149] J.P. Rouse, F. Cortellino, W. Sun, T.H. Hyde, J. Shingledecker, Small punch creep testing : review on modelling and data interpretation, Mater. Sci. Technol. 29 (2013)

1328–1345.

[150] B. Dagon, T.H. Hyde, Sampling and small punch test for utility services, in: K. Matoch, W.Sun (Eds.), 2nd Int. Conf. SSTT-Determination Mech. Prop. Mater. by Small Punch Other Miniat. Test. Tech., Ostrava (CZ), 2012: pp. 26–37.

[151] B. Gülçimen, P. Hähner, Determination of creep properties of a P91 weldment by small punch testing and a new evaluation approach, Mater. Sci. Eng. A. 588 (2013) 125–131.

[152] T.H. Hyde, On the Determination of Material Creep Constants Using Miniature Creep Test Specimens, J. Eng. Mater. Technol. 136 (2014) 021006 (1-10).

[153] S. Rashno, B. Nami, S.M. Miresmaeili, Impression creep behavior of a cast MRI153 magnesium alloy, Mater. Des. 60 (2014) 289–294.

[154] T.R.G. Kutty, S. Kaity, A. Kumar, Impression Creep Behaviour of U−6%Zr Alloy-Role of Microstructure, Procedia Eng. 55 (2013) 561–565.

[155] W. Sun, T.H. Hyde, S.J. Brett, Use if the impression creep test method for determining minimum creep strain rate data, in: K. Matocha, R. Hurst, W. Sun (Eds.), 2nd Int. Conf. SSTT-Determination Mech. Prop. Mater. by Small Punch Other Miniat. Test. Tech., Ostrava (CZ), 2012: pp. 297–304.

[156] T.H. Hyde, W. Sun, A.A. Becker, Analysis of the impression creep test method using a rectangular indenter for determining the creep properties in welds, Int. J. Mech. Sci. 38 (1996) 1089–1102.

[157] S.N.G. Chu, J.C.M.Li, Impression creep of β-tin single crystals, Mater. Sci. Eng. 39 (1979) 1–10.

[158] J.C.M. Li, Impression Creep and Other Localised Tests, Mater. Sci. Eng. A. 322 (2002) 23–42.

[159] F. Yang, Impression Creep: Effects of slip, stick and cavity depth, Int. J. Mech. Sci. 40 (1998) 87–96.

[160] D. Chiang, J.C.M. Li, Impression creep of lead, Mater. Res. Soc. 9 (1994) 903–908.

[161] W. Yan, S. Wen, J. Liu, Z. Yue, Comparison between impression creep and uni-axial tensile creep performed on nickel-based single crystal superalloys, Mater. Sci. Eng. A. 527 (2010) 1850–1855.

[162] F. Yang, J.C.M. Li, Impression creep of a thin film by vacancy diffusion . I . Straight punch, J. Appl. Phys. 74 (1993) 4382–4389.

[163] F. Yang, J.C.M. Li, Impression creep of a thin film by vacancy diffusion. II . Cylindrical punch, J. Appl. Phys. 74 (2008) 4390–4397. doi:10.1063/1.354407.

[164] T.H. Hyde, K.A. Yehia, A.A. Becker, Interpretation of impression creep data using a reference stress approach, Int. J. Mech. Sci. 35 (1993) 451–462.

[165] T.H. Hyde, K.A. Yehia, A.A. Becker, Application of the reference stress method for interpreting impression creep test data, Mater. High Temp. 13 (1995) 133–138. doi:10.1080/09603409.1995.11689511.

[166] W. Schlitz, A history of fatigue, Eng. Fract. Mech. 54 (1996) 263–300.

[167] R.E. Reed-Hill, Physical metallurgy principles, Princeton, N.J.: Van Nostrand, 1964.

[168] S. Suresh, Fatigue of materials, Cambridge University Press, New York, USA, 1991.

[169] T. Courtney, Mechanical Behaviour of Materials, McGraw-Hill Higher Education, USA, 2000.

[170] W.. Kim, C. Laird, Crack nucleation and stage I propagation in high strain fatigue - I. Microscopic and interferometric observations, Acta Metall. 26 (1978) 777–787.

[171] W.. Kim, C. Laird, Crack nucleation and stage I propagation in high strain fatigue - II. Mechanism, Acta Metall. 26 (1978) 789–799.

[172] N.E. Dowling, Mean Stress Effects in Stress-Life and Strain-Life Fatigue, SAE Tech. Pap. 2 (2004) 2004-01-2227.

[173] N.E.Dowling, C.A. Calhoun, A. Arcari, Mean stress effects in stress-life fatigue and the Walker equation, Fatigue Fract. Eng. Mater. Struct. 32 (2009) 163–179.

[174] N.E. Dowling, Mean stress effects in strain – life fatigue, Fatigue Fract. Eng. Mater. Struct. 32 (2009) 1004–1019. doi:10.1111/j.1460-2695.2009.01404.x.

[175] A. Nies, Mean stress effect correction in frequency-domain methods for fatigue life assessment, Procedia Eng. 101 (2015) 347–354. doi:10.1016/j.proeng.2015.02.042.

[176] N.E.Dowling, Mechanical Behaviour of Materials, Prentice-Hall Inc., Englewood Cliffs, New Jersey, USA, 1993.

[177] A. Kumar, R.K. Gautam, R. Tyagi, Dry sliding wear characteristics of in situ synthesized Al-TiC composites, Compos. Interfaces. 6440 (2016) 0. doi:10.1080/09276440.2016.1148434.

[178] R. Saraswat, A. Yadav, R. Tyagi, Sliding Wear Behaviour of Al-B_4C Cast Composites Under Dry Contact, Mater. Today Proc. 5 (2018) 16963–16972.

[179] V. Kumar, R.K. Gautam, R. Tyagi, Tribological behavior of Al-based self-lubricating composites, Compos. Interfaces. 6440 (2016) 1–12.

[180] N. Yuvaraj, S. Aravindan, Vipin, Comparison studies on mechanical and wear behavior of fabricated aluminum surface nano composites by fusion and solid state processing, Surf. Coat. Technol. 309 (2017) 309–319.

[181] M. Uthayakumar, S. Aravindan, K. Rajkumar, Wear performance of Al–SiC–B_4C hybrid composites under dry sliding conditions, Mater. Des. 47 (2013) 456–464.

[182] S. Giribaskar, R. Prasad, Ultra-Fine Grained Al-SiC Metal Matrix Composite by Rotary Swaging Process, Mater. Sci. Forum. 702–73 (2011) 320–323.

[183] K.L.A. Khan, P. Mahajan, R. Prasad, Synthesis And Characterization of Al Foam , Al Alloy Foam And Al-SiC Composite Foam, Trans. Indian Inst. Met. 61 (2008) 111–113.

[184] F. Ubaid, P.R. Malti, R.A. Shakoor, G. Parande, V. Manakari, A.M.A. Mohamed, M. Gupta, Using B_4C Nanoparticles to Enhance Thermal and Mechanical Response of Aluminum, Materials (Basel). 10 (2017) 1-12

[185] T.S. Srivatsan, M. Al-hajri, C. Smith, M. Petraroli, The tensile response and fracture behavior of 2009 aluminum alloy metal matrix composite, Mater. Sci. Eng. A. 346 (2003) 91–100.

[186] A.M.A. Mohamed, M. Gupta, Effect of reinforcement concentration on the properties of hot extruded Al-Al_2O_3 composites synthesized through microwave sintering process, Mater. Sci. Eng. A. 696 (2017) 60–69. doi:10.1016/j.msea.2017.04.064.

[187] T.S. Srivatsan, Microstructure, tensile properties and fracture behaviour of Al_2O_3 particulate-reinforced aluminium alloy metal matrix composites, J. Mater. Sci. 31 (1996) 1375–1388.

[188] G. Palumbo, I. Brooks, J. McCrea, G.D. Hibbard, F. Gonzalez, K. Tomantchger, U. Erb, Process for electroplating metallic and metall matrix composite foils, coatings and microcomponents, US 2005/0205425 A1, 2005.

[189] E. Bele, B.A. Bouwhuis, C. Codd, G.D. Hibbard, Structural ceramic coatings in composite microtruss cellular materials, Acta Mater. 59 (2011) 6145–6154. doi:10.1016/j.actamat.2011.06.027.

[190] M.K. Surappa, S. V Prasad, P.K. Rohatgi, Wear and abrasion of cast Al-Alumina particle composites, Wear. 77 (1982) 295–302.

[191] Y. Sahin, Preparation and some properties of SiC particle reinforced aluminium alloy composites, Metallography. 24 (2003) 671–679. doi:10.1016/S0261-3069.

[192] A. Baradeswaran, A. Elaya Perumal, Influence of B_4C on the tribological and mechanical properties of Al 7075-B_4C composites, Compos. Part B Eng. 54 (2013) 146–152. doi:10.1016/j.compositesb.2013.05.012.

[193] H. Wang, G. Li, Y. Zhao, G. Chen, In situ fabrication and microstructure of Al_2O_3 particles reinforced aluminum matrix composites, Mater. Sci. Eng. A. 527 (2010) 2881–2885. doi:10.1016/j.msea.2010.01.022.

[194] H. Arik, Effect of mechanical alloying process on mechanical properties of a Si_3N_4

reinforced aluminum-based composite materials, Mater. Des. 29 (2008) 1856–1861. doi:10.1016/j.matdes.2008.03.010.

[195] K.B. Lee, H.S. Sim, S.W. Heo, H.R. Yoo, S.Y. Cho, H. Kwon, Tensile properties and microstructures of Al composite reinforced with BN particles, Compos. - Part A Appl. Sci. Manuf. 33 (2002) 709–715. doi:10.1016/S1359-835X(02)00011-8.

[196] B.N. Sahoo, S.K. Panigrahi, Synthesis , characterization and mechanical properties of in-situ (TiC-TiB_2) reinforced magnesium matrix composite, JMADE. 109 (2016) 300–313. doi:10.1016/j.matdes.2016.07.024.

[197] B.S.S. Daniel, V.S.R. Murthy, Nickel aluminide reinforced AlN/Al composites by pressureless infiltration, Mater. Lett. 37 (1998) 334–339. doi:10.1016/S0167-577X(98)00116-5.

[198] S. Kumar, M. Chakraborty, V. Subramanya Sarma, B.S. Murty, Tensile and wear behaviour of in situ Al-7Si/TiB_2 particulate composites, Wear. 265 (2008) 134–142. doi:10.1016/j.wear.2007.09.007.

[199] C.S. Ramesh, S. Pramod, R. Keshavamurthy, A study on microstructure and mechanical properties of Al 6061-TiB_2 in-situ composites, Mater. Sci. Eng. A. 528 (2011) 4125–4132. doi:10.1016/j.msea.2011.02.024.

[200] B. Hekner, J. Myalski, N. Valle, A. Botor-Probierz, M. Sopicka-Lizer, J. Wieczorek, Friction and wear behavior of Al-SiC(n) hybrid composites with carbon addition, Compos. Part B Eng. 108 (2017) 291–300. doi:10.1016/j.compositesb.2016.09.103.

[201] N.B. Podymova, A.A. Karabutov, Combined effects of reinforcement fraction and porosity on ultrasonic velocity in SiC particulate aluminum alloy matrix composites, Compos. Part B. 113 (2017) 138–143. doi:10.1016/j.compositesb.2017.01.017.

[202] Q. Han, Y. Geng, R. Setchi, F. Lacan, D. Gu, S.L. Evans, Macro and nanoscale wear behaviour of Al-Al_2O_3 nanocomposites fabricated by selective laser melting, Compos. Part B. 127 (2017) 26–35. doi:10.1016/j.compositesb.2017.06.026.

[203] Ş. Karabulut, H. Karakoç, R. Çıtak, Influence of B_4C particle reinforcement on mechanical and machining properties of Al6061/B_4C composites, Compos. Part B Eng. 101 (2016) 87–98. doi:10.1016/j.compositesb.2016.07.006.

[204] Ş. Karabulut, U. Gökmen, H. Çinici, Study on the mechanical and drilling properties of AA7039 composites reinforced with Al_2O_3/B_4C/SiC particles, Compos. Part B Eng. 93 (2016) 43–55. doi:10.1016/j.compositesb.2016.02.054.

[205] D. Roy, S. Ghosh, A. Basumallick, B. Basu, Preparation of Ti-aluminide reinforced in situ aluminium matrix composites by reactive hot pressing, J. Alloys Compd. 436 (2007) 107–111.

[206] S. Srinivasan, Synthesis of Al/Al_3Ti two-phase alloys by mechanical alloying, Mater. Sci. Eng. A. 153 (1992) 691–695.

[207] Y. Birol, Analysis of the response to thermal exposure of Al/K_2TiF_6 powder blends, J. Alloys Compd. 478 (2009) 265–268. doi:10.1016/j.jallcom.2008.12.016.

[208] J.M. Wu, S.L. Zheng, Z.Z. Li, Thermal stability and its effects on the mechanical properties of rapidly solidified Al-Ti alloys, Mater. Sci. Eng. A 289 (2000) 246–254.

[209] L.Froyen, In-situ p/m Al/(ZrB_2+Al_2O_3) MMCs: Processing, microstructure and mechanical, Acta Mater. 47 (1999) 4571-4583.

[210] D.G. Eskin, K. Al-Helal, I. Tzanakis, Application of a plate sonotrode to ultrasonic degassing of aluminum melt: Acoustic measurements and feasibility study, J. Mater. Process. Technol. 222 (2015) 148–154. doi:10.1016/j.jmatprotec.2015.03.006.

[211] V.O. Abramov, O. V Abramov, F. Sommer, D. Orlov, Properties of Al-Pb base alloys applying electromagnetic forces and ultrasonic vibration during casting, Mater. Lett. 23 (1995) 17–20.

[212] J. Fjellstedt, A.E.W. Jarfors, On the precipitation of TiB_2 in aluminum melts from the reaction with KBF_4 and K_2TiF_6, Mater. Sci. Eng. A. 413–414 (2005) 527–532. doi:10.1016/j.msea.2005.09.054.

[213] J. Fjellstedt, A.E.W. Jarfors, Experimental and theoritical study of Al rich corner in the ternary Al-Ti-B system and reassessment of the Al-rich side of the binary Al-B phase diagram, Z. Met. 92 (2001) 563–571.

[214] Z. He-guo, W. Hang-zhi, G. Liang-qi, Formation of composites fabricated by exothermic dispersion reaction in Al-TiO_2-B_2O_3 system, Tans. Nonferrous Met. Sco. China. 17 (2007) 590–594.

[215] H.M. Lee, Design of Al_3(Ti,V,Zr) systems through phase stability calculations, Mater. Sci. Eng. A. 152 (1992) 26–30.

[216] G.I. Eskin, D.G. Eskin, Ultrasonic Treatment of Light Alloy Melts, 2nd Edition, Second, CRC press, 2015.

[217] J. Li, T. Momono, Y. Tayu, Y. Fu, Application of ultrasonic treating to degassing of metal ingots, Mater. Lett. 62 (2008) 4152–4154. doi:10.1016/j.matlet.2008.06.016.

[218] Z. Liu, M. Rakita, W. Xu, X. Wang, Q. Han, Ultrasound assisted salts-metal reaction for synthesizing TiB_2 particles at low temperature, Chem. Eng. J. 263 (2015) 317–324. doi:10.1016/j.cej.2014.11.043.

[219] Z. Liu, M. Rakita, X. Wang, W. Xu, Q. Han, In situ formed Al_3Ti particles in Al alloy matrix and their effects on the microstructure and mechanical properties of 7075 alloy, J. Mater. Res. 29 (2014) 1354–1361. doi:10.1557/jmr.2014.123.

[220] G.R. Li, H.M. Wang, Y.T. Zhao, D. Bin Chen, G. Chen, X.N. Cheng, Microstructure of in situ Al_3Ti/6351Al composites fabricated with electromagnetic stirring and fluxes, Trans. Nonferrous Met. Soc. China (English Ed. 20 (2010) 577–583. doi:10.1016/S1003-6326(09)60181-3.

[221] T. V. Atamanenko, D.G. Eskin, M. Sluiter, L. Katgerman, On the mechanism of grain refinement in Al-Zr-Ti alloys, J. Alloys Compd. 509 (2011) 57–60.

[222] G.K. Sigworth, The Grain Refining of Aluminum and Phase Relationships in the Al-Ti-B System, Metall. Trans. A. 15 (1984) 277–282.

[223] B. Ashok Kumar, N. Murugan, Metallurgical and mechanical characterization of stir cast AA6061-T6-AlNp composite, Mater. Des. 40 (2012) 52–58.

[224] N. El-mahallawy, M.A. Taha, A.E.W. Jarfors, H. Fredriksson, On the reaction between aluminium, K_2TiF_6 and KBF_4, J. Alloys Compd. 292 (1999) 221–229.

[225] J. V. Wood, P. Davies, J.L.F. Kellie, Properties of reactively cast aluminium–TiB_2 alloys, Mater. Sci. Technol. 9 (1993) 833–840. doi:10.1179/mst.1993.9.10.833.

[226] N. Srivastava, G.P. Chaudhari, Strengthening in Al alloy nano composites fabricated by ultrasound assisted solidification technique, Mater. Sci. Eng. A. 651 (2016) 241–247. doi:10.1016/j.msea.2015.10.118.

[227] T. Li, E. Al Olevsky, M.A. Meyers, The development of residual stresses in Ti6Al4V-Al_3Ti metal-intermetallic laminate (MIL) composites, Mater. Sci. Eng. A. 473 (2008) 49–57. doi:10.1016/j.msea.2007.03.069.

[228] G.K. Meenashisundaram, M.H. Nai, M. Gupta, Effects of Primary Processing Techniques and Significance of Hall-Petch strengthening on the mechanical response of Magnesium Matrix Composites containing TiO_2 nanoparticulates, Nanomater. 5 (2015) 1256–1283. doi:10.3390/nano5031256.

[229] S. Guha, S. Sangal, S. Basu, Finite Element studies on indentation size effect using a higher order strain gradient theory, Int. J. Solids Struct. 50 (2013) 863–875. doi:10.1016/j.ijsolstr.2012.10.017.

[230] S. Guha, S. Sangal, S. Basu, Numerical investigations of flat punch molding using a higher order strain gradient plasticity theory, Int J Mater Forum. 7 (2014) 459–467. doi:10.1007/s12289-013-1141-z.

[231] O.B. Bembalge, S.K. Panigrahi, Development and strengthening mechanisms of bulk ultra fine grained AA6063/SiC composite sheets with varying reinforcement size ranging from nano to micro domain, J. Alloys Compd. 766 (2018) 355–372. doi:10.1016/j.jallcom.2018.06.306.

[232] C.S. Kim, I. Sohn, M. Nezafati, J.B. Ferguson, B.F. Schultz, Z. Bajestani-Gohari, P.K. Rohatgi, K. Cho, Prediction models for the yield strength of particle-reinforced unimodal pure magnesium (Mg) metal matrix nanocomposites (MMNCs), J. Mater. Sci. 48 (2013) 4191–4204. doi:10.1007/s10853-013-7232-x.

[233] S. Aravindan, P. V Rao, K. Ponappa, Evaluation of physical and mechanical properties of AZ91D/SiC composites by two step stir casting process, J. Magnes. Alloy. 3 (2015) 52–62. doi:10.1016/j.jma.2014.12.008.

[234] C.S. Ramesh, R. Keshavamurthy, B.H. Channabasappa, A. Ahmed, Microstructure and mechanical properties of Ni-P coated Si_3N_4 reinforced Al6061 composites, Mater. Sci. Eng. A. 502 (2009) 99–106. doi:10.1016/j.msea.2008.10.012.

[235] F.J. Humphreys, The nucleation of recrystallization at second phase particles in deformed aluminium, Acta Metall. 25 (1977) 1323–1344. doi:10.1016/0001-6160(77)90109-2.

[236] A. Khandelwal, K. Mani, N. Srivastava, R. Gupta, G.P. Chaudhari, Mechanical behavior of AZ31/Al_2O_3 magnesium alloy nanocomposites prepared using ultrasound assisted stir casting, Compos. Part B Eng. 123 (2017) 64–73. doi:10.1016/j.compositesb.2017.05.007.

[237] S.A. Khorramie, M.A. Baghchesara, D.P. Gohari, Fabrication of Aluminum matrix composites reinforced with Al_2ZrO_5 Nano particulates synthesized by sol-gel auto-combustion method, Trans. Nonferrous Met. Soc. China (English Ed. 23 (2013) 1556–1562. doi:10.1016/S1003-6326(13)62630-8.

[238] N. Kumar, R.K. Gautam, S. Mohan, In-situ development of ZrB_2 particles and their effect on microstructure and mechanical properties of AA5052 metal-matrix composites, Mater. Des. 80 (2015) 129–136. doi:10.1016/j.matdes.2015.05.020.

[239] Z. Xiuqing, W. Haowei, L. Lihua, T. Xinying, M. Naiheng, The mechanical properties of magnesium matrix composites reinforced with (TiB_2 + TiC) ceramic particulates,

Mater. Lett. 59 (2005) 2105–2109. doi:10.1016/j.matlet.2005.02.020.

[240] Q. Zhang, B.L. Xiao, W.G. Wang, Z.Y. Ma, Reactive mechanism and mechanical properties of in situ composites fabricated from an Al–TiO_2 system by friction stir processing, Acta Mater. 60 (2012) 7090–7103. doi:10.1016/j.actamat.2012.09.016.

[241] F. Chen, Z. Chen, F. Mao, T. Wang, Z. Cao, TiB_2 reinforced aluminum based in situ composites fabricated by stir casting, Mater. Sci. Eng. A. 625 (2015) 357–368. doi:10.1016/j.msea.2014.12.033.

[242] T. Wang, Z. Chen, Y. Zheng, Y. Zhao, H. Kang, L. Gao, Development of TiB_2 reinforced aluminum foundry alloy based in situ composites – Part II : Enhancing the practical aluminum foundry alloys using the improved Al – 5 wt % TiB_2 master composite upon dilution, Mater. Sci. Eng. A. 605 (2014) 22–32.

[243] M. Wang, D. Chen, Z. Chen, Y. Wu, F. Wang, N. Ma, H. Wang, Mechanical properties of in-situ TiB_2/A356 composites, Mater. Sci. Eng. A. 590 (2014) 246–254. doi:10.1016/j.msea.2013.10.021.

[244] Z. Lin, Y. Li, F.A. Mohamed, Creep and substructure in 5 vol.% SiC-2124 Al composite, Mater. Sci. Eng. A. 332 (2002) 330–342.

[245] F.M. Xu, L.C.M. Wu, G.W. Han, Y. Tan, Compression creep behavior of high volume fraction of SiC particles reinforced Al composite fabricated by pressureless infiltration, Chinese J. Aeronaut. 20 (2007) 115–119.

[246] F. Ji, M.Z. Ma, A.J. Song, W.G. Zhang, H.T. Zong, S.X. Liang, Y. Osamu, R.P. Liu, Creep behavior of in situ TiC_P/2618 aluminum matrix composite, Mater. Sci. Eng. A. 506 (2009) 58–62.

[247] S.M. Miresmaeili, B. Nami, Impression creep behavior of Al-1.9%Ni-1.6%Mn-1%Mg alloy, Mater. Des. 56 (2014) 286–290.

[248] M.D. Mathew, Naveena, D. Vijayanand, Impression creep behavior of 316LN stainless steel, J. Mater. Eng. Perform. 22 (2013) 492–497.

[249] S. Gangolu, A.G. Rao, N. Prabhu, V.P. Deshmukh, B.P. Kashyap, N. Materials, S. Road, Flow Behavior of Alumnium- 15 % Boron Carbide Composite By Differential Strain Rate, conference proceeding "The 19th International Conference on composite materials", 1–9.

[250] Y. Li, F.A. Mohamed, An investigation of creep behavior in an SiC-2124 Al composite, Acta Mater. 45 (1997) 4775–4785. doi:10.1016/S1359-6454(97)00130-4.

[251] T.G. Nieh, K. Xia, T.G. Langdon, Mechanical properties of discontinuous sic reinforced aluminum composites at elevated temperatures, J. Eng. Mater. Technol. Trans. ASME. 110 (1988) 77–82.

[252] Z.Y. Ma, S.C. Tjong, The high-temperature creep behaviour of 2124 aluminium alloys with and without particulate and SiC-whisker reinforcement, Compos. Sci. Technol. 59 (1999) 737–747. doi:10.1016/S0266-3538(98)00113-4.

[253] A.B. Pandey, R.S. Mishra, Y.R. Mahajan, Creep fracture in Al-SiC metal-matrix composites, J. Mater. Sci. 28 (1993) 2943–2949. doi:10.1007/BF00354697.

[254] W.D. Nix, Steady state and transient creep properties of an aluminium alloy reinforced with a alumina fibers, Acta Metall. Metaralia. 40 (1992).

[255] H. Kumar, G.P. Chaudhari, Creep behavior of AS41 alloy matrix nano-composites, Mater. Sci. Eng. A. 607 (2014) 435–444. doi:10.1016/j.msea.2014.04.020.

[256] F. Labib, R. Mahmudi, H.M. Ghasemi, Impression creep behavior of extruded Mg–SiCp composites, Mater. Sci. Eng. A. 640 (2015) 91–97.

[257] B. Zhao, B. Xu, Z. Yue, Indentation creep-fatigue test on aluminum alloy 2A12, Mater. Sci. Eng. A. 527 (2010) 4519–4522.

[258] K.B. Khan, T.R.G. Kutty, M.K. Surappa, Hot hardness and indentation creep study on Al-5% Mg alloy matrix-B_4C particle reinforced composites, Mater. Sci. Eng. A. 427 (2006) 76–82. doi:10.1016/j.msea.2006.04.015.

[259] H. Wang, Q.D. Wang, C.J. Boehlert, J. Yang, D.D. Yin, J. Yuan, W.J. Ding, The

impression creep behavior and microstructure evolution of cast and cast-then-extruded Mg-10Gd-3Y-0.5Zr (wt%), Mater. Sci. Eng. A. 649 (2016) 313–324. doi:10.1016/j.msea.2015.10.001.

[260] F. Kabirian, R. Mahmudi, Impression creep behavior of a cast AZ91 magnesium alloy, Metall. Mater. Trans. A Phys. Metall. Mater. Sci. 40 (2009) 116–127. doi:10.1007/s11661-008-9699-7.

[261] G. Samimi, S. Mirdamadi, H. Razavi, M.A. Boutorabi, Improvement in impression creep property of as-cast AC515 Mg alloy by Mn addition, Mater. Sci. Eng. A. 587 (2013) 213–220. doi:10.1016/j.msea.2013.08.068.

[262] G. Cseh, J. Bär, H.J. Gudladt, J. Lendvai, A. Juhász, Indentation creep in a short fibre-reinforced metal matrix composite, Mater. Sci. Eng. A. 272 (1999) 145–151. doi:10.1016/S0921-5093(99)00466-9.

[263] E. Mohammadi Mazraeshahi, B. Nami, S.M. Miresmaeili, Investigation on the impression creep properties of a cast Mg-6Al-1Zn magnesium alloy, Mater. Des. 51 (2013) 427–431. doi:10.1016/j.matdes.2013.04.045.

[264] T.R.G. Kutty, S. Kaity, C.B. Basak, A. Kumar, R.P. Singh, Creep behaviour of U-6%Zr alloy by impression creep technique, Nucl. Eng. Des. 250 (2012) 125–133. doi:10.1016/j.nucengdes.2012.05.013.

[265] S. Takeuchi, A.S. Argon, Steady-state creep of alloys due to viscous motion of dislocations, Acta Metall. 24 (1976) 883–889. doi:10.1016/0001-6160(76)90036-5.

[266] H. Liu, Y. Chen, Y. Tang, S. Wei, G. Niu, Tensile and indentation creep behavior of Mg-5% Sn and Mg-5% Sn-2% Di alloys, Mater. Sci. Eng. A. 464 (2007) 124–128. doi:10.1016/j.msea.2007.02.061.

[267] N. Dowling E., Mechanical behavior of Materials, Prentice-Hall, Upper saddle River, New Jersey, 1999.

[268] P. Zhang, Creep behavior of the die-cast Mg-Al alloy AS21, Scr. Mater. 52 (2005)

277–282. doi:10.1016/j.scriptamat.2004.10.017.

[269] O.D. Sherby, J.L. Lytton, J.E. Dorn, Activation energies for creep of high purity aluminium, Acta Metall. 5 (1957) 219–227.

[270] Frost. H.J and Ashby. M.F., Deformation-mechanism maps, Pergamon Press, New York, 1982.

[271] B.N. Sahoo, S.K. Panigrahi, Effect of in-situ (TiC-TiB_2) reinforcement on aging and mechanical behavior of AZ91 magnesium matrix composite, Mater. Charact. 139 (2018) 221–232. doi:10.1016/j.matchar.2018.03.002.

[272] S.M. Miresmaeili, B. Nami, Impression creep behavior of Al-1.9%Ni-1.6%Mn-1%Mg alloy, Mater. Des. 56 (2014) 286–290. doi:10.1016/j.matdes.2013.11.011.

[273] A.E. Hammad, A.A. Ibrahiem, Enhancing the microstructure and tensile creep resistance of Sn-3.0Ag-0.5Cu solder alloy by reinforcing nano-sized ZnO particles, Microelectron. Reliab. 75 (2017) 187–194. doi:10.1016/j.microrel.2017.07.034.

[274] J.A. Lee, Cast Aluminum Alloy for High Temperature Applications, Automot. Alloy. TMS. 1 (2003).

[275] H. Somekawa, K. Hirai, H. Watanabe, Y. Takigawa, K. Higashi, Dislocation creep behavior in Mg-Al-Zn alloys, Mater. Sci. Eng. A. 407 (2005) 53–61. doi:10.1016/j.msea.2005.06.059.

[276] S.M. Zhu, J.F. Nie, B.L. Mordike, J.F. Nie, Creep and rupture properties of a squeeze-cast Mg-Al-Ca alloy, Metall. Mater. Trans. A. 37 (2006) 1221–1229. doi:10.1007/s11661-006-1073-z.

[277] S.C. Tjong, G.S. Wang, Cyclic deformation behavior of in situ aluminum – matrix composites of the system Al – Al_3Ti – TiB_2 – Al_2O_3, Compos. Sci. Technol. 64 (2004) 1971–1980. doi:10.1016/j.compscitech.2004.02.006.

[278] S.C. Tjong, G. Wang, Synthesis and Low Cycle Fatigue Behavior of In-situ Al-based Composite Reinforced with Submicron TiB_2 and TiC Particulates, Adv. Eng. Mater.

6 (2004) 964–968.

[279] S. Suresh, Fatigue of materials, Second, Cambridge University Press, Cambridge, 2003.

[280] A. Ayyar, N. Chawla, Microstructure-based modeling of crack growth in particle reinforced composites, Comp. Sci. Tech. 66 (2006) 1980–1994.

[281] R.W. Hertzberg, Deformation and fracture mechanics of engineering materials, Fourth, Wiley, New York, USA, 1995.

[282] Y. Sugimura, S. Suresh, Effects of SiC Content on Fatigue Crack Growth in Aluminum Alloys Reinforced with SiC Particles, Metall. Trans. A 23 (1992) 2231-2242.

[283] Y. Xiong, W. Wang, R. Jiang, K. Lin, G. Song, Surface integrity of milling in-situ TiB 2 particle reinforced Al matrix composites, Int . J. Refract. Met. Hard Mater. 54 (2016) 407–416. doi:10.1016/j.ijrmhm.2015.09.007.

[284] J. Rui-song, W. Wen-hu, S. Guo-dong, W. Zeng-qiang, Experimental investigation on machinability of in situ formed TiB_2 particles reinforced Al MMCs, J. Manuf. Process. 23 (2016) 249–257. doi:10.1016/j.jmapro.2016.05.004.

[285] L. Lu, M. La, F.L. Chen, Al-4 wt. % Cu composite reinforced with in-situ TiB_2 particles, Acta Mater. 45 (1997).

[286] X.P. Li, G. Ji, Z. Chen, A. Addad, Y. Wu, H.W. Wang, J. Vleugels, J. Van Humbeeck, J.P. Kruth, Selective laser melting of nano-TiB_2 decorated AlSi10Mg alloy with high fracture strength and ductility, Acta Mater. 129 (2017) 183–193. doi:10.1016/j.actamat.2017.02.062.

[287] S. Agrawal, A.K. Ghose, I. Chakrabarty, Effect of rotary electromagnetic stirring during solidification of In-situ, Mater. Des. 113 (2017) 195–206. doi:10.1016/j.matdes.2016.10.007.

[288] F. Chen, Z. Chen, F. Mao, T. Wang, Z. Cao, TiB_2 reinforced aluminum based in situ

composites fabricated by stir casting, Mater. Sci. Eng. A. 625 (2015) 357–368. doi:10.1016/j.msea.2014.12.033.

[289] J. Mathew, A. Mandal, S.D. Kumar, S. Bajpai, M. Chakraborty, G.D. West, P. Srirangam, Effect of semi-solid forging on microstructure and mechanical properties of in-situ cast Al-Cu-TiB_2 composites, J. Alloys Compd. 712 (2017) 460–467. doi:10.1016/j.jallcom.2017.04.113.

[290] M. Wang, D. Chen, Z. Chen, Y. Wu, F. Wang, N. Ma, H. Wang, Mechanical properties of in-situ TiB_2/A356 composites, Mater. Sci. Eng. A. 590 (2014) 246–254. doi:10.1016/j.msea.2013.10.021.

[291] T.S. Srivatsan, Cyclic strain resistance and fracture behaviour of Al_2O_3-particulate-reinforced 2014 aluminium alloy metal-matrix composites, Int. J. Fatigue. 17 (1995) 183–199.

[292] S.C. Tjong, G.S. Wang, High-cycle fatigue properties of Al-based composites reinforced with in situ TiB_2 and Al_2O_3 particulates, Mater. Sci. Eng. A. 386 (2004) 48–53. doi:10.1016/j.msea.2004.07.021.

[293] Y. Ma, Z. Chen, M. Wang, D. Chen, N. Ma, H. Wang, High cycle fatigue behavior of the in-situ TiB_2/7050 composite, Mater. Sci. Eng. A. 640 (2015) 350–356. doi:10.1016/j.msea.2015.06.023.

[294] F. Wang, J. Xu, J. Li, X. Li, H. Wang, Fatigue crack initiation and propagation in A356 alloy reinforced with in situ TiB_2 particles, J. Mater. 33 (2012) 236–241. doi:10.1016/j.matdes.2011.07.028.

[295] J.J. Bonnen, J.E. Allison, J.W. Jones, Fatigue Behavior of a 2xxx Series Aluminum Alloy Reinforced with 15 vol. % SiCp, Metall. Trans. A. 22A (1991) 1007–1019.

[296] S. Skolianos, Mechanical behavior of cast SiCp-reinforced, Mater. Sci. Eng. A. 210 (1996) 76–82.

[297] P. Cavaliere, Mechanical properties of Friction Stir Processed 2618/Al2O3/20p metal

matrix composite, Compos. Part A. 36 (2005) 1657–1665.

[298] K. Tokaji, H. Shiota, K. Kobayashi, Effect of particle size on fatigue behaviour in SiC particulate-reinforced aluminium alloy composites, Fatigue Fract. Eng. Mater. Struct. 22 (1999) 281–288.

[299] S.C. Tjong, Y.W. Mai, Failure of metal-matrix composites, in: I. Milne, R. Ritchie, B. Karihaloo (Eds.), Compr. Struct. Integr., Elsevier, New York, 2007: pp. 798–849.

[300] B.G. Park, A.G. Crosky, A.K. Hellier, High cycle fatigue behaviour of microsphere Al_2O_3–Al particulate metal matrix composites, Compos. Part B. 39 (2008) 1257–1269. doi:10.1016/j.compositesb.2008.01.006.

[301] N. Chawla, C. Andres, J.W. Jones, J.E. Allison, The effect of reinforcement volume fraction and particle size on the fatigue behavior of an aluminum alloy/SiC composite, Ind. Heat. 66 (1999) 61–66.

[302] N.E. Bekheet, R.M. Gadelrab, M.F. Salah, A.N.A. El-azim, The effects of aging on the hardness and fatigue behavior of 2024 Al alloy/SiC composites, Mater. Des. 23 (2002) 153–159.

[303] S.C. Tjong, G.S. Wang, Y.-W. Mai, High cycle fatigue response of in-situ Al-based composites containing TiB_2 and Al_2O_3 submicron particles, Compos. Sci. Technol. 65 (2005) 1537–1546. doi:10.1016/j.compscitech.2005.01.012.

[304] K. Wallin, T. Saario, K. Torronen, Fracture of brittle particles in a ductile matrix, Int. J. Fract. 32 (1987) 201–209.

[305] R.W. Armstrong, The Influence of Polycrystal Grain Size on Several Mechanical Properties of Materiels, Metall. Trans. 1 (1970) 1169–1176.

[306] C.Y. Kung, M.E. Fine, Fatigue Crack Initiation and Microcrack Growth in 2024-T4 and 2124-T4 Aluminum Alloys, Metall. Trans. A. 10 (1979) 603–610.

[307] C.Q. Bowles, J. Schijve, The role of inclusions in fatigue crack initiation in an aluminium alloy, Int. J. Fract. 9 (1973) 171–179.

[308] J.N. Hall, J.W. Jones, A.K. Sachdev, Particle size, volume fraction and matrix strength effects on fatigue behavior and particle fracture in 2124 aluminum-SiCp composites, Mater. Sci. Eng. A. 183 (1994) 69–80.

[309] J. Llorca, P. Poza, Influence of reinforcement fracture on the cyclic stress-strain curve of metal-matrix composites, Acta Metall. Mater. 43 (1995) 3959–3969.

[310] R. Gupta, G.P. Chaudhari, B.S.S. Daniel, Strengthening mechanisms in ultrasonically processed aluminium matrix composite with in-situ Al_3Ti by salt addition, Compos. Part B Eng. 140 (2018) 27–34. doi:10.1016/j.compositesb.2017.12.005.

[311] N. Chawla, C. Andres, L.C. Davis, J.W. Jones, J.E. Allison, The Interactive Role of Inclusions and SiC Reinforcement on the High-Cycle Fatigue Resistance of Particle Reinforced Metal Matrix Composites, Mrtallurgical Mater. Trans. A. 31 (2000) 951–957.

[312] D.A. Lukasak, D.A. Koss, Microstructural influences on fatigue crack initiation in a model particulate-reinforced aluminium alloy MMC, Composites. 24 (1993) 262–269.

[313] T.S. Srivatsan, A. R, P. A, L. EJ, Influence of microstructure on cyclic stress response and cyclic fracture behaviour of aluminium alloy metal–matrix composite, in: S.H. Teoh, K.H. Lee (Eds.), Jt. FEFG/ICF Int. Conf. Fract. Eng. Mater. Struct., Elsevier Applied Science, Singapore, 1991: pp. 194–202.

[314] D. Broek, Elementary Engineering Fracture Mechanics, MARTINUS NIJHOFF PUBLISHERS THE HAGUE/BOSTON/LONDON, London, UK, 1982.

[315] S. Malekjani, P.D. Hodgson, P. Cizek, I. Sabirov, T.B. Hilditch, Cyclic deformation response of UFG 2024 Al alloy, Int. J. Fatigue. 33 (2011) 700–709.

[316] H. Liu, S. Yang, C. Xie, Q. Zhang, Y. Cao, Microstructure characterization and mechanism of fatigue crack initiation near pores for 6005A CMT welded joint, Mater. Sci. Eng. A. 707 (2017) 22–29. doi:10.1016/j.msea.2017.09.029.